Accurately determining the number of Auger electrons per nuclear decay for medical isotopes

A thesis submitted for the degree of

Doctor of Philosophy

at the

Australian National University

Mohammed Fatem Alotiby

محمد بن فاطم العتيبي

July 2019

Declaration

I declare that, to the best of my knowledge, this thesis is my own original work and does not contain any material previously published or written by another person except where otherwise indicated.

Mohammed Fatem Alotiby

Date: 26/07/2019

"After three generations of R&D in biotechnology, radiobiology and Auger emitter production methods, we are now closer than ever to finally realising this early dream".

The European Science Foundation report (2014).

PUBLICATIONS ARISING FROM THIS RESEARCH

Journal Publications

1. *"Measurement of the intensity ratio of Auger and conversion electrons for the electron capture decay of ^{125}I"*

M. Alotiby, I. Greguric, T. Kibédi, B. Q. Lee, M. Roberts, A. E. Stuchbery, Pi. Tee, T. Tornyi and M. Vos, Physics in Medicine & Biology, http://iopscience.iop.org/article/10.1088/1361-6560/aab24b/meta

2. *"Quantitative electron spectroscopy of ^{125}I over an extended energy range"*

M. Alotiby, I. Greguric, T. Kibédi, Pi. Tee, and M. Vos, Electron Spectroscopy and Related Phenomena, https://www.sciencedirect.com/science/article/pii/S0368204819300027

3. *"High-resolution conversion electron spectroscopy of the ^{125}I electron-capture decay"*

B.P.E. Tee, A.E. Stuchbery, M. Vos, J.T. Dowie, B.Q. Lee, **M. Alotiby**, I. Greguric, and T. Kibédi. Physics Review C, under review.

Conference Presentations

1. *"Accurately determining the number of Auger electrons per nuclear decay for medical isotopes"*

M Alotiby, M. Vos, T. Tornyi, T. Kibédi, B.Q. Lee, A.E. Stuchbery, M. Roberts and I. Greguric. **(Oral Presentation).** Innovation in Radiation Applications 2017 **https://eis.uow.edu.au/content/groups/public/@web/@eis/documents/doc/uow230531.pdf**

2. "*Accurately determining the number of Auger electrons per nuclear decay for medical isotopes"*

M Alotiby, M. Vos, T. Tornyi, T. Kibédi, B.Q. Lee, A.E. Stuchbery, M. Roberts and I. Greguric. **(Poster Presentation).** International Conference on Photonic, Electronic and Atomic Collisions *http://icpeac30.edu.au/posterlist.php*

3. *"Experimental investigation of the conversion electrons from medical radioisotope ^{125}I"*

B. Tee, T. Kibédi, **M. Alotiby**, M. Vos, and I. Gregoric. **(Oral Presentation).** Heavy Ion Accelerator Symposium 2018
http://hias.anu.edu.au/2018/_files/2018_HIAS_BookOfAbstracts.pdf

4. *"Measurement of Auger electrons emitted after nuclear decay: the case of ^{125}I"*

M.Vos, **M. Alotiby**, T. Kibédi, Pi Tee, and I. Gregoric. **(Oral Presentation).** Heavy Ion Accelerator Symposium 2018
http://hias.anu.edu.au/2018/_files/2018_HIAS_BookOfAbstracts.pdf

ACKNOWLEDGEMENTS

This work would not have been possible without support and advice from many people.
First, I am highly indebted to my supervisor Dr. Maarten Vos for his supervision, patience, and guidance from the early stage of my PhD journey. Thanks, Maarten for introducing me to the world of research physics through your project. I would not forget to remember your timely support and guidance till the completion of my PhD study. My sincere thanks go to my supervisors Dr. Tibor Kibédi and Professor. Andrew Stuchbery, who provided me an opportunity to join their team as a PhD student, and for their help, advice and support during my PhD study. I am also grateful to Dr. Tamas Tornyi and Mr. Bryan Tee for their valuable support and help on my research.

I would like to thank Australian Nuclear Science and Technology Organisation (ANSTO) for their support through preparing the Iodine-125 source.

I am thankful to my postgraduate colleagues Mr. David Stevens, Mr. David Shin, Jack Li and all other colleagues in Australian National University who gave constant encouragement and support which helped me in successfully completing my project work. In addition, I would like to extend my sincere esteem to the technician staff (Mr. Ross Tranter and Mr. Colin Dedman) for their valuable technical support on this project.

I wish to think my parents, my brothers and sisters for their support and encouragement throughout my study. My thanks are also extended to my wife Abeer and my kids Aziz and Yasi for their constant support and love.

Finally, I would like to acknowledge with much appreciation to my scholarship sponsor King Abdulaziz City for Science and Technology (KACST) for financing my PhD study.

ABSTRACT

Auger-emitting radionuclides have great potential in cancer treatment as low-energy Auger electrons (< 5 keV) deposit a large amount of energy in a small volume. Auger-based therapy is attractive as, in contrast to alpha and beta particles, the affected volume around the decaying radionuclides is much smaller than the volume of a cell. Moreover, low-energy electrons (3-20 eV) have been shown to be very effective in causing DNA cleavage. In this study, a third of monolayer of ^{125}I was deposited on a gold surface and the energy of the emerging electrons was measured. ^{125}I decays by electron capture to a nuclear excited state of ^{125}Te. A core hole in the atomic electron cloud is created in the electron capture process, which relaxes via an Auger cascade that produces multiple Auger electrons. Subsequently, the nuclear excited state of ^{125}Te internally decays to the nuclear ground state and the excess energy can also eject an atomic electron (the conversion electron), which also leaves a core hole behind, and the newly created core hole will relax by an Auger cascade as well. The conversion electron and the Auger electrons have similar energies, and thus their intensities can be compared, linking the nuclear- and atomic-physics parts of the decay of ^{125}I.

A Monte Carlo model (BrIccEmis) was used to simulate the Auger-electron spectrum. BrIccEmis is based on the known intensity of the conversion electron line and estimates of the decay rates for Auger and X-ray emission. In order to fit the measured spectrum one has to assume a line shape model describing among others, the effects of shake off. A discussion was held regarding whether one can get a good description of experimental the spectrum of ^{125}I absorbed on an Au surface, based on the calculated one for atomic ^{125}I decay with reasonable assumptions for the line shape.

The measurements of the very low-energy Auger electrons (<1 keV), which are particularly relevant to medical physics applications, are even more difficult to quantify, and preliminary results in this energy range are also discussed.

CONTENTS

LIST OF TABLES

LIST OF FIGURES

Chapter 1

Introduction

Cancer is one of the leading causes of morbidity and mortality worldwide. Its prevalence is expected to rise by about 70% over the next two decades as mentioned by the World Health Organisation (WHO) [1]. In 2016, the US Department of Health and Human Services reported that more than 1.5 million US patients were clinically identified as having cancer [2], roughly, 50% of cancer patients were estimated to need radiation therapy [3]. More recent data does not indicate any different ratio [1, 4, 5]. Despite extensive efforts in cancer research, cancer treatment still presents a real challenge. One of the most common treatments for cancer is radiotherapy, which relies on ionising radiation such as X-rays, γ-rays or protons to induce DNA (deoxyribonucleic acid) double-strand breakage in the cancer cells [6]. Another common type of cancer treatment is chemotherapy, which employs drugs to kill the fast-growing cancer cells [7]. In either case, the healthy cells are not spared but are damaged along with the cancer cells during the treatment. Consequently, the treatments induce side effects such as fatigue, hair loss and higher risks for subsequent cancers [8]. Therefore, it is crucial at present to develop more effective treatments for cancer.

During nuclear decay processes such as electron capture (EC) and internal conversion (IC) cause interactions with the electrons in atomic shells, leading to a vacancy in one of the sub-shells. The vacancy thus created is refilled by an electron from an outer shell and the excess energy of the transitioning electron is liberated and dissipated in one of the two ways: either in the form of an X-ray or by the ejection of another shell electron, that is so-called Auger electron emission [9, 10]. The details of electron capture, internal conversion and the Auger effect are presented in chapter 2.

Radiation therapy causes few or no side effects if the radiation is limited to the area where the tumor is located. Introducing a radiation source with a very short range into the body would accomplished this. Low-energy electrons (less than 10 keV) have a very short range and such electrons are emitted as Auger electrons after certain forms of nuclear decay. Understanding the basic physical process of low-energy Auger electron emission can result in better radiobiological models and thus more effective treatments [11, 12].

The importance of this study stems from significant advances in the last decade in the understanding of the biological effects of low-energy electrons [13], and consequently new interest in the use of Auger electrons for targeted tumour therapy [14, 15].

Radiation in the form of particles and gamma rays have fundamentally different interactions with matter. These types of primary radiation deposit their energy over the course of their trajectory by ionising their surroundings, thereby producing non-thermal secondary electrons. The role of these low-energy electrons has only recently begun to be appreciated [16, 17]. Low-energy electrons are the most important contributors to radiation damage in biological environments because, although they have energies below the typical ionisation threshold of organic matter (3-20 eV), these electrons have been shown to be very effective in causing DNA cleavage [12, 18]. This ability is evident in their high cross-section for breaking chemical bonds, and consequently they have a very short electron inelastic mean-free path of ~ 1-10 nm [19].

Low-energy Auger electrons emitted following electron capture or internal conversion offer an easy and convenient way to harness the unique properties mentioned in the previous paragraph, which is nowhere more important than in targeted tumour therapy [20]. Moreover, Auger electrons have showed very promising effects in-vitro and in-vivo in animal studies over the last decade [21-25].

Already in 1927, the radiation therapy pioneers, Claudius Regaud and Antoine Lacassagne, suggested that it would be possible to have a selective cure for cancer by depositing radionuclides in the cancer cells. This idea has now evolved into targeted radiotherapy. They concluded their paper with the following statement [16]:

“The ideal agent for cancer therapy would consist of heavy elements capable of emitting radiations of molecular dimensions, which could be administered to the organism and selectively fixed in the protoplasm of cells one seeks to destroy. While this is perhaps not impossible to achieve, the attempts so far have been unsuccessful.”

After several iterations of development in biotechnology, radiobiology and Auger emitter production methods, targeted cancer therapy no longer remains solely in the realm of theory. It is now closer to reality than ever before [26].

1.1 General characteristics of therapeutic particle emissions

Theoretically, the effectiveness of any radionuclide depends on the probability of damage to critical target molecules, e.g. DNA. Damage to critical target molecules will result in cell death. A particular target molecule is affected by ionisation due to either the traversal of the emitted radiation directly through the target molecule (direct ionisation), or ionisation in its close vicinity, as ionisation of a surrounding water molecules produces reactive oxygen species that disperse over ~ 4 nm to ionise a target molecule (indirect ionisation) [27]. The Linear Energy Transfer (LET) is the total amount of energy deposited per unit track length, regardless of whether that energy was the result of direct or indirect ionisation. The ratio between direct and indirect ionisation depends upon the kind of emitted particle [28]. The desired interaction range of the particle for highly-targeted therapy is of the order of a few nanometers (in the environment of water), which is the size of a strand of human DNA [29]. Particle emissions for therapeutic purposes, such as beta particles, alpha emission and Auger electrons, can be compared based on their biophysical properties as shown in Figure 1.1.

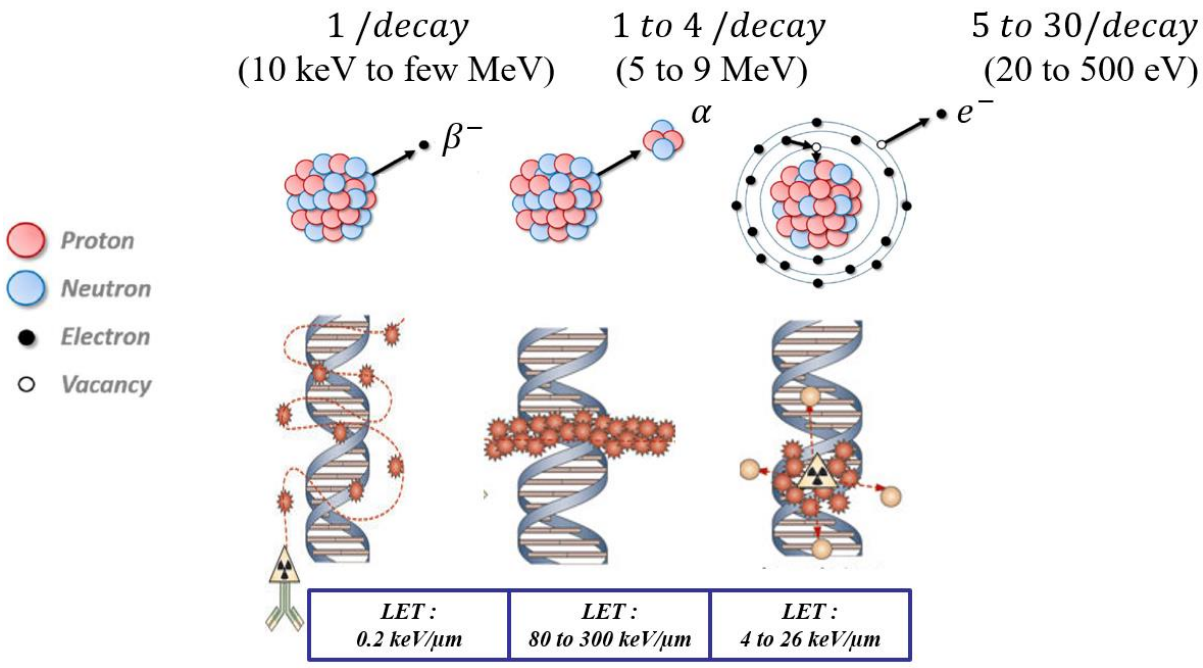

Figure 1.1: Biophysical properties of beta, alpha, and Auger electron emitting radionuclides (uper panel). Image was extracted from [28]. Lower panel shows local ionisation patterns of beta, alpha, and Auger electron on the scale of DNA. Image was extracted from [30].

Beta particles (β^-) have a broad high energy distribution extending up to a maximum value of a few MeV, with a long range in the environment of water from 0.05 to 11.8 mm. (β^-) are emitted from radionuclides such as ^{90}Y,^{131}I or ^{177}Lu at a rate of typically one particle per decay. After the β^- particle's emission, the daughter nucleus has one more proton and one less neutron (see Figure 1.2). As beta particles traverse matter, they lose their kinetic energy and their track paths become increasingly contorted due to scattering. Scattering results from elastic collisions with atomic nuclei and electrons causing changes in the direction of propagation with no energy loss. In contrast, inelastic collisions with atomic nuclei produce bremsstrahlung (German for "braking radiation") and inelatic colloisions with orbital electrons result in ionisations and excitations [28]. The beta particle produces sparse ionisation with low LET (0.2 keV/µm), except over the few nm at the end of its path length.

Alpha particles are positively charged with a mass and charge equal to that of the helium nucleus, their emission leading to a daughter nucleus that has two fewer protons and two fewer neutrons as presented in Figure 1.2. Over the last 40 years, the therapeutic potential of several

alpha-particle-emitting radionuclides (e.g. ^{212}Pb, ^{223}Ra and ^{227}Th) has been assessed. Alpha particles have energies ranging from 5 to 9 MeV resulting in a linear track length on the order of approximately 5 mammalian-cell diameters (20 to 80 µm in water) [31]. The LET of Alpha particle is very high (~80-100 keV/µm), increasing to ~300 keV/µm toward the end of the track (the Bragg peak). The proportion of DNA single-strand breaks (SSB) to double strand breaks (DSB) induced by alpha particle emitters is 20:1 compared to 60:1 as observed with low-LET radiation such as X-rays [28].

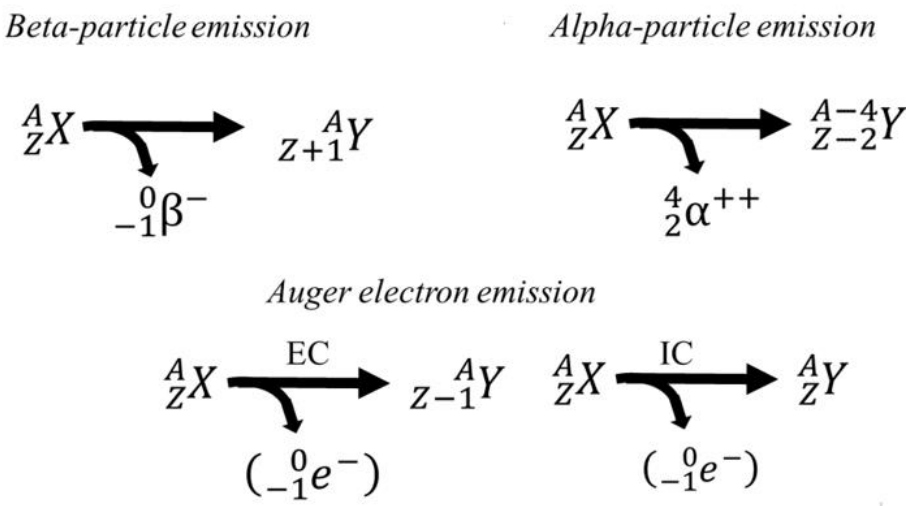

Figure 1.2: Schematic of emissions produced during the decay of therapeutic radionuclide [31].

Auger electrons have much lower energy than beta particles. Radionuclides that decay by electron capture or internal conversion (see Figure 1.2) produce low-energy Auger electrons with subcellular range (order of nanometers). During the first half of the 20th century, the scientific community showed no significant interest in pursuing the radiobiological effects of low energy electrons [13]. However, by the late 1960s and thereafter, encouraging results were found for radionuclides emitting low energy electrons such as Auger and conversion elections. These electrons are suitable tools for highly-targeted therapy [32-35]. Auger electrons are mainly (more than 90%) low-energy electrons (~20 to 500 eV), they traverse matter in contorted paths with a range from a fraction of nanometer up to 500 nm in water, with multiple ionisations (LET ~ 4 to 26 keV/µm) occurring in the vicinity of the decay site [28, 36]. Thus, as a consequence of the short range, it ought to be possible to minimise the undesirable radiation dose to the healthy tissue with the resultant adverse side effects. Another advantage that makes Auger electrons attractive for highly targeted therapy is that, in favourable cases,

5-30 electrons with energies ranging from a few eV to approximately 1 keV, are emitted from a nuclide undergoing an EC decay or an IC process. Targeted therapy that employs Auger electrons as a therapeutic emitter is called Auger therapy [31, 37].

1.2 Choice of isotope

There are several factors that need to be taken into consideration when selecting radioisotopes for use with Auger therapy. The radioisotope must have the following characteristics: (i) production of Auger electrons with desired energies. (ii) Suitable decay scheme and physical half-life to deliver enough radiation to the target cells. (iii) Minimal gamma and X-ray emsission is required to ensure limited effects on adjacent tissue, while still allowing monitoring of radionuclide in the body. This implies a low ratio of X-and γ rays to electron emission, for the purpose of radiolabeling to monitor the therapy with imaging, and to trace the absorbed dose distribution. One of the ideal candidates is thus iodine-125 (^{125}I) because it has specific decay characteristics that meet these standards [38]. However, to use this medical isotope in practice, accurate knowledge of the Auger emission rates (Auger yield per nuclear decay) and energies is needed to estimate the appropriate dose. Motivated by these factors, the primary goal of the present thesis is to measure an accurate Auger yield from the ^{125}I medical radioisotope, using the Auger to conversion electron (CE) intensity ratio.

1.3 Historical development of our knowledge of Auger electrons

X-ray photoelectron spectroscopy developed rapidly following the discovery of the photoelectric effect by Hertz in 1887. The photoelectron spectra of many elements were obtained in the early 1920s. At that time, most of the experiments on the photoelectric effect were performed using magnetic analysers and photographic detection. However, C.T.R. Wilson had suggested in 1912 an experimental setup (the cloud chamber) which allowed a direct observation of charged particle trajectories [39]. In 1922, Pierre Auger started his research activities by building, with his friend Francis Perrin, the first Wilson expansion chamber in France. By modifying the experimental conditions, he observed that the energy of the emitted electrons was independent of the frequency of the primary X-rays and that each element tested had characteristic electron energies [40].

Numerous unexplained features in X-ray emission spectra were resolved in 1935 by Coster and Kronig. They suggested radiationless Auger transitions with the first and second state associated with the same shell. The transition rate among them was large resulting from the significant overlap of the radial wave function of these states. Hence, the first state involved has a short lifetime and appears as a weak and diffuse X-ray emission line. The second state involved shows a satellite adjacent to the ordinary X-ray emission line, due to the atom having a further hole in an outer shell after the emission of an additional electron throughout the radiationless transition [41]. Auger electrons are widely used in materials science. Here the core vacancies are generally not due to nuclear decay but due to irradiation by X-rays or keV electrons.

Several experiments were performed in an attempt to further study the Auger electron. Lander, in the year 1953, carried out the first application of Auger electron spectroscopy to surface analysis. He examined several metals and metal oxides in a pyrex glass ultra-high vacuum system, and he determined the surface sensitivity of the method due to the high absorption coefficient of low energy electrons in the matter [42]. This was followed by Harrower who tried to employ the energy loss spectra to supplement the X-ray tables at low energies [43]. Nevertheless, the discovery of the Auger electron was not considered significant and hence not widely exploited until 1967, when Tharp and Scheibner showed the possibility of using LEED (low-energy electron diffraction) system to detect the energy distribution of Auger electron by examining the analyzer signal [44]. The lock-in technique method was also applied by Harris

to detect the first derivative of the electron emission signal. He used an electrostatic 127° sector analyser and modulated the retarding voltage with a small 7 kHz signal [45]. With this approach, it turned out that Auger electron peaks stand out clearly over a slowly varying background of secondary electrons. These two ideas, the detection of the first derivative of the Auger signal and the use of the standard LEED system for detection, made the method attractive for surface analysis in several ultra high vacuum laboratories. The introduction of a fourth grid in the LEED system, which was a next improvement step, was in 1969 by Palmberg, Bohan, and Tracy. This gave rise to a greatly improved resolution over the whole energy detection range. From the same group came the idea to use a cylindrical mirror analyzer and they found that the analyzer had a better signal to noise ratio as well as being much faster in the transmission than any analyzer used previously [46]. A further pioneering step was made by MacDonald who integrated a cylindrical analyzer into a scanning electron microscope. The use of a highly focused high energy electron beam for excitation of Auger transitions facilitated a high spatial resolution. By scanning the primary beam and detecting electron energies of characteristic Auger peaks, a chemical image of the surface could be produced [47].

More recently it was realised that Auger electrons could also be exploited in the field of radiotherapy for cancer treatment. This was based on the high biological toxicity, and the considerable therapeutic potential of these low energy electron emitters, mainly associated with a very high ionization density created in biological tissue (high-LET). However, the experimental measurement of Auger electrons produced by nuclear decay for medical applications is not straightforward, and data are scarce. The first measurement for Auger electrons of ^{125}I was in 1969 by Casey and Albridge [48]. The spectrum was recorded with the Vanderbilt iron-free, double focusing spectrometer and the source was prepared by depositing iodine on silver, but no information was given in terms of the relative intensity of the conversion line to the Auger peaks [48]. To our knowledge, the only group actively studying Auger spectroscopy after radioactive decay is in Dubna, Russia (see e.g. [49-52]). However, they focus largely on the shape of the high energy part of the spectrum (e.g. the KLL Auger transitions). For the low energy part of the spectrum, E < 600 eV, which is the most important for medical applications, the Auger spectrum from ^{125}I was measured recently in 2016 by Pronschinske et al. The only notable feature, identified by the authors, was the MNN-Auger peaks below about 520 eV [53].

1.4 Thesis outlines and contributions

In this thesis, the electron spectra from ^{125}I were measured and studied. The structure of this thesis is shown below:

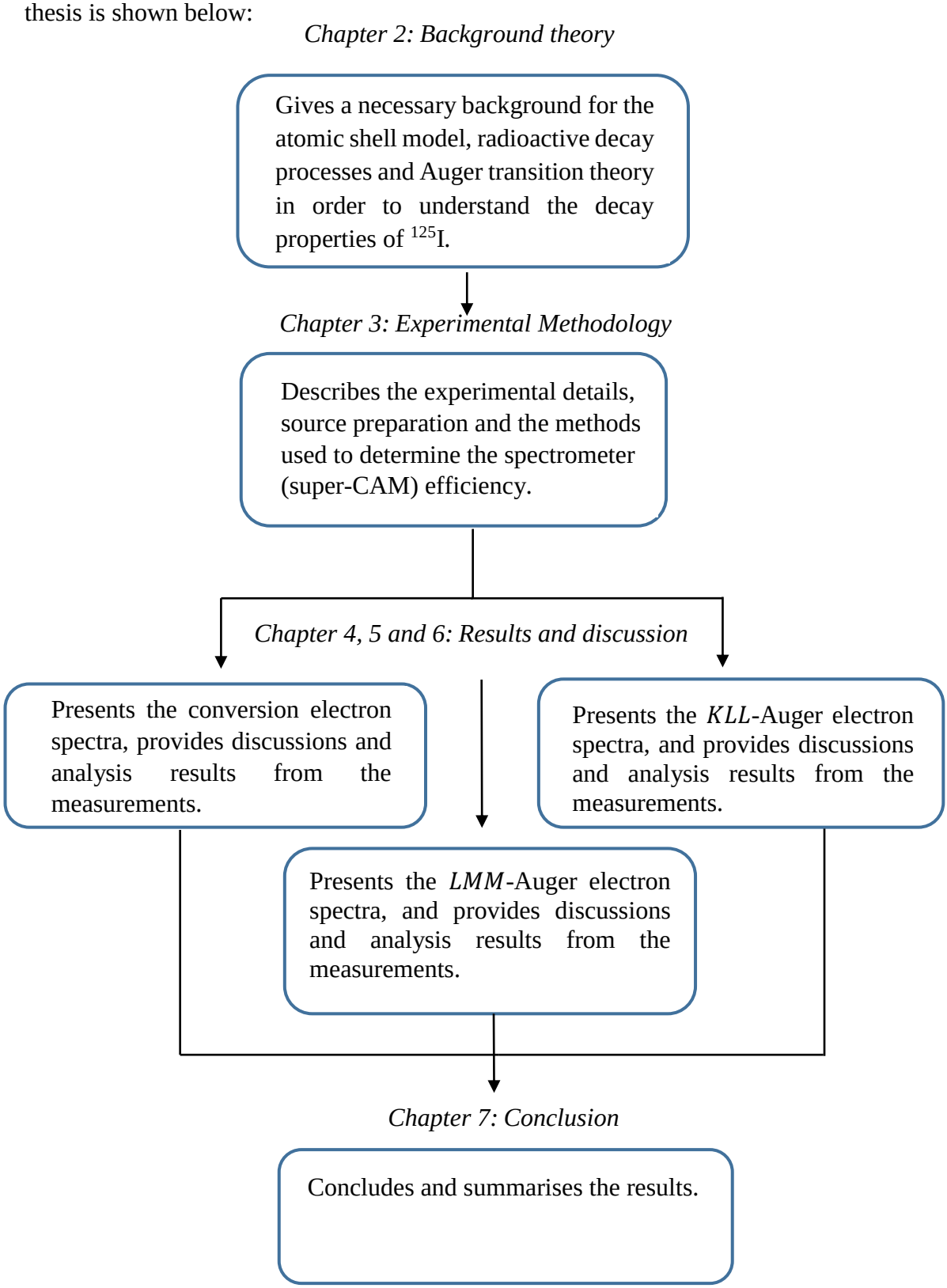

Chapter 2

Background theory

In this chapter, a basic description of the atomic shell model will be provided, and the physics related to the nuclear decay processes for ^{125}I will be reviewed. This chapter includes the concepts of electron capture probability, selection rules, mixing ratio, conversion coefficient and penetration effect. These concepts are followed by an introduction to Auger transitions and the physical process that produces Auger electrons. The Auger transition includes the concepts of Auger effect, relaxation effect, transition probabilities, and shake process. The classification of the KLL-Auger electrons is discussed as this group of Auger electrons was measured in the experiment. Following that, the computational models BrIcc (Band-Raman internal conversion coefficient) and BrIccEmis (Band-Raman internal conversion coefficient emission) that were used to compare with the measurements are also discussed. Lastly, the final section describes the decay scheme of ^{125}I.

2. 1 Theory of the atomic shell model

An explanation of the measured Auger spectra from the atomic relaxation after nuclear decay of ^{125}I to its daughter atom, ^{125}Te (tellurium-125) is provided through a brief discussion on the atomic shell model. Each shell is comprised of subshells, which represents an orbit. The three quantum numbers n, ℓ and m_l which represent the size of orbital, the shape of the orbital and the orientation in space of the orbital, respectively, are used to describe an electron occupying an atomic state. These three quantum numbers are the principal quantum number, the orbital angular momentum quantum number and the magnetic quantum number, respectively [54].

The notations K, L, M, N, O, P and Q are used to label principal shells and correspond to principal quantum number $n = 1, 2, 3, 4, 5, 6$ and 7, respectively. One or more subshell is contained in each principal shell which is quantified by the orbital angular momentum quantum number l which ranges from 0 to n-1 and the labelling is done with the notations s, p, d, f, g for $l = 0, 1, 2, 3, 4$ respectively. For instance, one subshell, $1s$, is contained in the K shell and the two subshells, $2s$ and $2p$, are contained in the L shell. The orbitals available within a subshell,

ranging from $-l$ to $+l$ (including zero), is specified by the magnetic quantum number m_l therefore there are $2l+1$ available states. For example, the number of orbitals in the s, p, d and f subshells are 1, 3, 5 and 7, respectively. Due to Pauli Exclusion principle, the number of electrons accommodated by each orbital is at most two and these electrons should have opposite spins $s = \pm 1/2$. For atomic electrons apart from s shell, the electron spin interacts with the orbital angular momentum, thus another quantum number j introduced, which is the total angular momentum vector and is defined as:

$$j = s + l. \tag{2.1}$$

The quantities s and l denote the electron's spin and the orbital angular momentum vectors respectively. The range of j is from $|l-s|$ to $|l+s|$ in integer steps [55]. The shell structure and the atomic notation for the subshell in tellurium is illustrated in a very schematic way by Figure 2.1 and additional detail is given in Table 2.1.

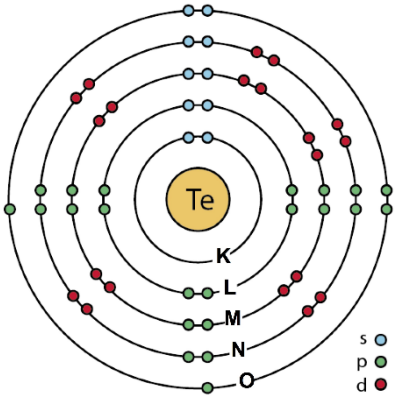

Figuer 2.1: Shell structure of tellurium. The K, L, M, N and O principal shells are labelled on the figure, and the subshells s, p and d are labelled with blue, green and red colours respectively. The image was extracted from [56].

Table 2.1: Atomic notation for shells with different sets of quantum numbers for tellurium.

Energy level	Binding Energy (eV) [57]	Quantum numbers				Atomic Notation
		n	l	s	j	
K	31814	1	0	$\pm 1/2$	$1/2$	$1s_{1/2}$
L_1	4939	2	0	$\pm 1/2$	$1/2$	$2s_{1/2}$
L_2	4612	2	1	$-1/2$	$1/2$	$2p_{1/2}$
L_3	4341	2	1	$+1/2$	$3/2$	$2p_{3/2}$
M_1	1006	3	0	$\pm 1/2$	$1/2$	$3s_{1/2}$
M_2	870.8	3	1	$-1/2$	$1/2$	$3p_{1/2}$
M_3	820	3	1	$+1/2$	$3/2$	$3p_{3/2}$
M_4	583.4	3	2	$-1/2$	$3/2$	$3d_{3/2}$
M_5	573	3	2	$+1/2$	$5/2$	$3d_{5/2}$
N_1	169.4	4	0	$\pm 1/2$	$1/2$	$4s_{1/2}$
N_2	103.3	4	1	$-1/2$	$1/2$	$4p_{1/2}$
N_3	103.3	4	1	$+1/2$	$3/2$	$4p_{3/2}$
N_4	41.9	4	2	$-1/2$	$3/2$	$4d_{3/2}$
N_5	40.4	4	2	$+1/2$	$5/2$	$4d_{5/2}$
O_1	11.6	5	0	$\pm 1/2$	$1/2$	$5s_{1/2}$
O_2	2.3	5	1	$-1/2$	$3/2$	$5p_{1/2}$
O_3	2.3	5	1	$+1/2$	$3/2$	$5p_{3/2}$

2.2 Radioactive decay

Radioactive decay is the spontaneous disintegration of an atomic nucleus resulting in energy and/or matter being emitted from the nucleus. In a sample composed of a large number of radioactive nuclei which decay in a random process, it is not possible to predict which nucleus from within a group of nuclei will disintegrate at a specific time. Thus, the process has to be treated in a statistical manner. Therefore there is a probability that a particular radioactive nucleus will decay in a certain period of time [58].

2.2.1 Radioactive decay law

When a radioactive disintegration occurs with the emission of radiation the initial atom, called the 'parent' atom, is transformed into something else called the 'daughter'. The fundamental law of radioactive decay was first formulated by Rutherford and Soddy in 1902 [59]. They found that the rate at which a particular radioactive material decays was dependent on the number of atoms present at that time (see Figure 2.2). Consider a source with N radioactive nuclei. At the time t the number of nuclei that will decay during the time dt is

$$dN = -\lambda N dt, \tag{2.2}$$

where λ is the decay constant of radioactive isotope and the minus sign indicates that the number of atoms of the radioactive element is decreasing as the source decays with time. Integrating the prevoius equation leads to the number of nuclei as a function of time. Thus the radioactive decay law can be expressed mathematically as:

$$N(t) = N_0 e^{-\lambda t}, \tag{2.3}$$

where N_0 denotes the initial number of radioactive nuclei at $t = 0$. From equation (2.2), the number of nuclei which decay between t and $t + dt$ is $dN = -\lambda N dt = -\lambda N_0 e^{-\lambda t} dt$. Thus the average time of decay, known as the mean life is

$$\tau = \frac{\int_0^\infty t e^{-\lambda t} dt}{\int_0^\infty e^{-\lambda t} dt} = \frac{1}{\lambda}. \tag{2.4}$$

The half-life $t_{1/2}$, which is the time that is required for half of the nuclei to decay, can be expressed in terms of λ by subsituting $N(t_{\frac{1}{2}}) = N_0\ /2$ in equation (2.3) and solving for $t_{1/2}$, therefore:

$$t_{1/2} = \frac{ln2}{\lambda}. \tag{2.5}$$

The activity or decay rate of a radioactive source describes the number of decays per unit time:

$$A(t) = \left|\frac{dN}{dt}\right| = \lambda N_0 e^{-\lambda t} = A_0 e^{-\lambda t}. \tag{2.6}$$

where $A_0 = \lambda N_0$ is the initial activity at $t = 0$. The SI unit for the activity is the Becquerel (Bq), with 1 Bq equal to one decay per second [60].

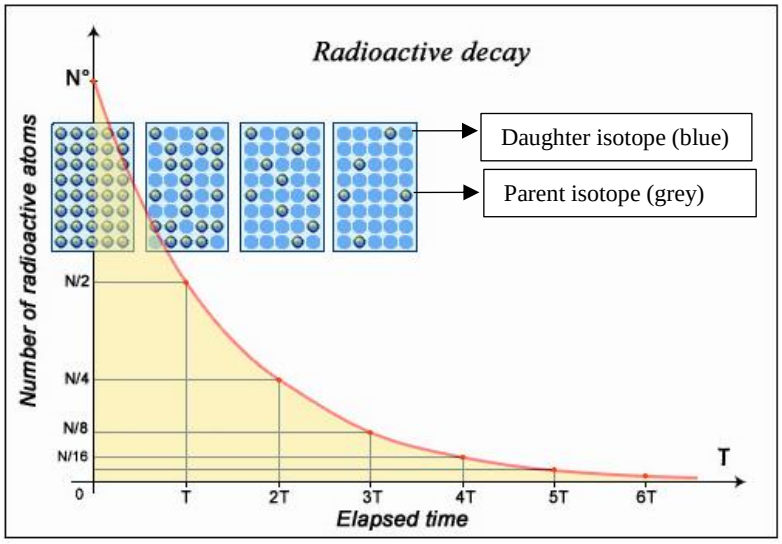

Figure 2.2: Radioactive decay reduces the number of radioactive nuclei over time. The number of nuclei in a radioactive source is halved after a certain period of time known as the half-life. Half of what remains will decay in the next half-life, and so on [61].

2.2.2 Disintegration modes

There are several forms of radioactive decay. Decay by alpha or beta particle emission is not an efficient source of atomic inner-shell core holes, and thus these decay modes do not result in significant Auger electron emission. ^{125}I has both electron capture and internal conversion resulting in inner shell core hole creation and hence cause Auger emission, the subject of this thesis. The ^{125}I decay scheme is shown in Figure 2.3. This scheme will be discussed in detail in section 2.6. Here is described these decay modes (electron capture and internal conversion) as well as gamma emission, as it competes with the conversion electron process.

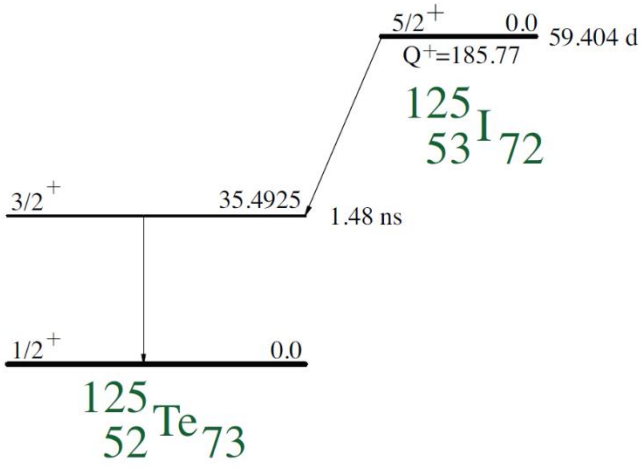

Figure 2.3: The ^{125}I decay scheme [62]. Details of this schematic is presented in section 2.6.

2.2.2.1 Electron Capture (EC)

Electron capture is the process whereby a nucleus absorbs an electron and transforms from element Z to Z-1. In the process it emits an electron neutrino in order to balance the energy and conserve lepton number. An illustraion of the EC process is presented in Figure 2.4.

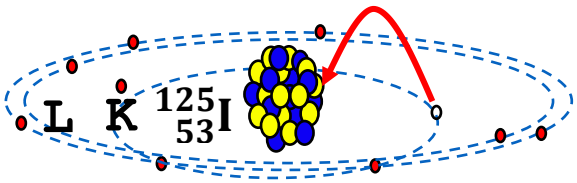

Figure 2.4: Illustration of the electron capture process for iodine-125. The nucleus (blue and yellow circles) captures one of its orbital electrons (red circles) with excess energy carried away by a neutrino (not shown in the figure).

^{125}I, which is used in this project, decays via electron capture to its daughter atom, ^{125}Te. EC is a decay process that creates atomic vacancies, the source of Auger electrons [63].

The equation given below illustrates the electron capture (EC) decay process.

$$ {}^{A}_{Z}X_{N} + e^{-} = {}^{A}_{Z-1}Y_{N+1} + \nu, \tag{2.7} $$

where A is the atomic mass, Z is the atomic number, N is a neutron number, X is the parent element, Y is the daughter element, e^{-} is an electron and ν is a neutrino.

In the case of ^{125}Te the decay is to the ground state and then energy conservation implies that the energy of the neutrino is:

$$ E_{\nu} = Q^{+} - E_{X}. \tag{2.8} $$

where Q^{+} is the energy of disintegration corresponding to the difference in atomic masses between parent ground state and daughter nuclear intial state, and E_X is the binding energy of the captured electron in the X shell (or the subshell) of ^{125}Te. The electron capture transition is only possible if the right hand side of equation (2.8) is positive. If the transition energy, $Q^{+} > E_K$, then the electron captured is far more probable to be from the K-shell than other shells [64]. Moreover, there are some radionuclides which can decay either by positron (β^{+}) emission or by EC. The governing factor deciding the process by which these radionuclides will decay is

the transition energy and is equal to the difference between the energy of disintegration, i.e. the change in atomic masses between the parent and the daughter ground states, and the energy of the excited nuclear state of the daughter nucleus[64, 65]. In the case of positron emission, this transition energy must exceed 1.022 MeV and hence the positron emission process is favourable for a transition energy above 1.022 MeV. On the other hand, for transition energies less than 1.022 MeV, EC is the only decay channel. Another factor which guides the decay process is the atomic number of the nuclide. If the atomic number is low, then positron emission decay is favoured, however with an increase in atomic number, the probability of EC increases. These factors can be illustrated by the examples of ^{22}Na and ^{65}Zn.

$$^{22}_{11}Na \rightarrow {}^{22}_{10}Ne + \beta^{+} + \nu \quad (90\%) \tag{2.9}$$

$$^{22}_{11}Na \xrightarrow{EC} {}^{22}_{10}Ne + \nu. \quad (10\ \%) \tag{2.10}$$

The transition energy of ^{22}Na is 2.842 MeV which is considerably higher than 1.022 MeV. Therefore the favourable route of decay in the case of ^{22}Na is positron emission [63].

Contrast the case of the nuclide ^{65}Zn, taking the following two examples:

$$^{65}_{30}Zn \rightarrow {}^{65}_{29}Cu + \beta^{+} + \nu \quad (1.42\%) \tag{2.11}$$

and

$$^{65}_{30}Zn \xrightarrow{EC} {}^{65}_{29}Cu + \nu. \quad (98.58\%) \tag{2.12}$$

The transition energy is 1.35 MeV, barely above the energy required for positron emission (1.022 MeV). Thus, EC decay dominates [66].

2.2.2.2 Gamma-ray decay

Electron capture can change ^{125}I into an excited state (energy E_i) of ^{125}Te, and this state will decay to the ground state (hence $E_f = 0$) by the emission of electromagnetic radiation, i.e. photons, or through the internal conversion process (to be discussed in section 2.2.2.3). The photon energy is given by:

$$E_\gamma = E_i - E_f. \tag{2.13}$$

Selection Rules

The multipolarity of a nuclear transition can be specified as either electric, E, or magnetic, M, as well as the angular momentum carried away by the photon, given by quantum number L. If $L = 0$, the transition is known as monopole, $L = 1$ dipole, $L = 2$ quadrupole and so on.

Angular momentum must be conserved during the decay. Therefore the difference in angular momentum between the excited state and final state is carried away by the emitted photon with corresponding angular momentum. Another conserved quantity is the total parity of the system [60].

A. Parity Change

Considering the parity change related with the transition, there is an uniqueness between the electric and magnetic multipole nature of the decay. Hence, for an electric transition, the parity change is given by $\Delta\pi_E = (-1)^L$and for the magnetic transition it is given by $\Delta\pi_M = (-1)^{L+1}$. This means that the radiation field for even parity would be $M1, E2, M3$ and $E4$ and for odd parity would be $E1, M2, E3$ and $M4$.

Then if there is a parity change from initial to final state($\pi_i \rightarrow \pi_f$) this is acounted for by the emitted phton (π_γ) with the relation [65]:

$$\pi_\gamma = \pi_i \pi_f. \tag{2.14}$$

B. Angular momentum

The angular momentum of the photon is determined by the angular momentum quantum numbers of the initial (J_i) and final (J_f) nuclear states of the transition and the requirement for angular momentum conservation. This is expressed in the vector equation [60]:

$$|J_i - J_f| \leq \mathrm{L} \leq |J_i + J_f|. \tag{2.15}$$

Consequently, the multipole transitions type needs to satisfy the conditions above, which are known as the selection rules. In brief, if there is no change in parity ($\Delta\pi = 0$) from an initial to final nuclear state and L is even (odd), then the transition type must be electric (magnetic). If there is a change in parity ($\Delta\pi \neq 0$) and L is even (odd), then the transition type must be magnetic (electric) [67]. Table 2.2 shows the selection rules for the 35 keV excited state in ^{125}Te.

Table 2.2: Selection rules for 35 keV transition from the decay of ^{125}Te excited state.

Multipolarity	Angular momentum change ΔL	Parity π change
$M1$	$-1, 0, +1$	$+1$
$E2$	$-2, -1, 0, +1, +2$	$+1$

2.2.2.3 Internal conversion

In certain cases the excitation energy of the nucleus is carried away by an atomic electron instead of the photon. This type of nuclear transition is called internal conversion (IC), and the ejected atomic electron is called an (internal) conversion electron. The initial explanation of the origin of mono-energetic electron energy resulting from the internal conversion of the gamma-decay energy was by Lise Meitner and Otto Hahn in Germany [63]. Luis W. Alvarez was the first to supply experimental evidence of internal conversion in artificially produced radioactive atoms [63]. An example of radionuclide decay by internal conversion is shown in Figure 2.3. Decay by internal conversion (IC) competes with gamma decay. An internal conversion electron may be ejected from an atom after absorbing the excitation energy from the nucleus. In this nuclear decay process, which is called an electromagnetic transition (EM), an excited nucleus decays to a lower excitation state and transmits its decay energy to an atomic electron in the X-shell ($X = K, L, M, etc$). The atomic electron is then emitted from the atom with an

energy corresponding to the nuclear decay energy, less the binding energy of the atomic electron:

$$E_{CE} = E_\gamma - E_s, \tag{2.16}$$

where E_s is the binding energy of the corresponding shell s where the converted electron was located. The binding energy of the electron varies with the atomic orbital and thus there will be separate internal conversion lines from atomic states with different binding energies. The conversion electron emission rate of (sub) shell s is quantified by the internal conversion coefficient, $\alpha_{CE,s}$, which is defined to be the probability ratio of conversion electron emission from shell s, $P_{CE,s}$, to photon emission I_γ:

$$\alpha_{CE,s} = P_{CE,s}/I_\gamma. \tag{2.17}$$

The sum of $\alpha_{CE,s}$, of all the (sub) shells is known as the total internal conversion coefficient $\alpha_{CE,T}$, which is defined to be the intensity ratio of total conversion electron emission for the nuclear transition, I_{CE}, to I_γ:

$$\alpha_{CE,T} = I_{CE}/I_\gamma \tag{2.18}$$

The total intensity for an electromagnetic decay can be written as [68]:

$$I_{Total} = I_\gamma + I_{CE} = I_\gamma\left(1 + \alpha_{CE,T}\right). \tag{2.19}$$

Based on the selection rules, it is allowed to have transitions with different multipole order compete. Therefore, additional information such as the mixing ratio δ is needed in order to describe a degree of multipolarity admixture in a transition. Assuming, there is $GL{+}G'L'$ during a transition, where G, $G'$are either electric or magnetic multipole fields, and L, L' are the corresponding quantum numbers of the angular momentum, then the square of the mixing ratio δ^2 is equal to the ratio of the transition rates of the photon intensity of the two multipolarity components [67].

$$\delta^2 = \frac{I_\gamma(G'L')}{I_\gamma(GL)}. \tag{2.20}$$

The internal conversion coefficient for a mixed transition ($GL/G'L'$) is related by:

$$\alpha_{CE}\left(\frac{GL}{G'L'}\right) = \frac{\alpha_{CE}(GL)+\delta^2\alpha_{CE}(G'L')}{1+\delta^2}, \tag{2.21}$$

where $\alpha_{CE}(GL)$ and $\alpha_{CE}(G'L')$, as can be calculated from theory, are the conversion coefficients of pure multipolarity, GL and $G'L'$, respectively [69]. The possibility for internal conversion to occur is dependent upon the subshell where the converted electron is created, the atomic number, Z, GL (multipolarity where the gamma-ray carries away angular momentum L), and the nuclear transition energy. General properties of the internal conversion coefficient are that they decrease when the transition energy is increased, they increase as the multipolarity is increased, and they become negligible in the case of high energies where electron-positron pair production becomes possible.

2.2.3 Nuclear parameters

Rose carried out the first computation of internal conversion coefficients relating to the K shell [70]. The calculations were done with the assumptions of an unscreened Coulomb field acting on atomic electrons along with a zero radius (point) nucleus. These estimates worked quite well for the lighter nuclei. However, for the case of a heavier nuclei, it was noted after some time that the size of the nucleus can cause noticeable corrections to the internal conversion coefficients. This effect is known as the penetration effect [71]. By assuming a finite nuclear size, the static nuclear charge distribution which acts on the atomic electrons has to be taken into account, causing a static effect (i.e. an energy shift). Moreover, the observable presence of the nuclear wave function will lead to extra matrix elements of operators that govern the electromagnetic transitions within the nucleus, an aspect that is referred to as the dynamic effect. The computations of the penetration effect on the conversion coefficients were done independently for the magnetic transitions and the electric transitions. More details can be found in the paper [72].

Due to the selection rules, the 35 keV excited state in ^{125}Te, from the electron capture decay of ^{125}I, decays with an admixture of magnetic dipole ($M1$) and electric quadrupole ($E2$) radiation to the ground state. Section 2.6 has details for the decay scheme of ^{125}I. The mixing ratio for this transition from the excited state to the ground state of ^{125}Te is found to be minute ($\delta \approx 0.03$ [73]), indicating that the transition is mostly $M1$. Hence, the focus is solely on studying the penetration effect for a magnetic transition. For this reason, two nuclear parameters are introduced: the penetration parameter which is denoted by λ, and the mixing parameter which is represented by Δ.

For a specific subshell s, the conversion coefficient for an $M1$ transition is given by the following equation:

$$\alpha(M1) = \alpha_0(M1)[1 + b_1(s)\lambda + b_2(s)\lambda^2], \tag{2.22}$$

where $\alpha_0(M1)$ represents the conversion coefficient related to pure magnetic transition without any penetration effect, $b_1(s)$ and $b_2(s)$ are the penetration coefficients of the subshell s, and the symbol λ represents the penetration parameter [74]. Additionally, the mixing Δ, is defined as:

$$\Delta = \frac{\delta^2}{1+\delta^2}, \tag{2.23}$$

where δ represents the $M1$ mixing ratio. Therefore, combining equation (2.21) and (2.23) gives the following result:

$$\alpha(M1 + E2) = \alpha(M1)(1 - \Delta) + \alpha(E2)\Delta. \tag{2.24}$$

The reason for having parameter Δ in the above equation is to facilitate the use of a least squares fitting method that is given in the analysis section 4.5. The penetration coefficients were calculated through the use of a modified version of the calculation program dubbed CATAR [72].

2.3 The natural width of a spectral line

As a consequence of the Heisenberg uncertainty principle, the uncertainty in the energy of a state, ΔE, is inversely proportional to the lifetime, τ of the excited state:

$$\Delta E \approx \frac{\hbar}{\tau}, \tag{2.25}$$

where $\hbar$ is the reduced Plank's constant. The uncertainty principle in this form shows that if the the lifetime decreases, the uncertainty in energy increases, $\Delta E \uparrow \Leftarrow \tau \downarrow$ [75]. The energy level of an excited state of an atom can never be determined precisely unless the state lives foverever (i.e. a stable state).

The energy distribution of the final state is given by the Lorentz distribution:

$$L(E) = \frac{1}{\pi} \frac{\frac{1}{2}\Gamma_f}{(E - E_f)^2 + (\frac{1}{2}\Gamma_f)^2}. \tag{2.26}$$

Note that Γ_f is also known as the Lorentzian (natural) width of state f. In an actual experiment, the measured energy distribution will be folded with a Gaussian line shape, due to instrumental resolution, which takes the form of:

$$G(E) = \frac{\sqrt{4ln2}}{w\sqrt{\pi}} exp - \left\{\frac{4ln2(E)^2}{w^2}\right\}, \tag{2.27}$$

where w is the full width at half maximum (FWHM) of the distribution. Hence, the measured energy is the convolution of Lorentzian and Gaussian line shapes, which is known as the Voigt line shape. The Voigt line shape has the form of

$$\int_{-\infty}^{\infty} G(E')L(E - E_f - E')dE'. \tag{2.28}$$

The Voigt line shape given in Figure 2.5 is calculated by Python [76] using the formulae described above [77-79].

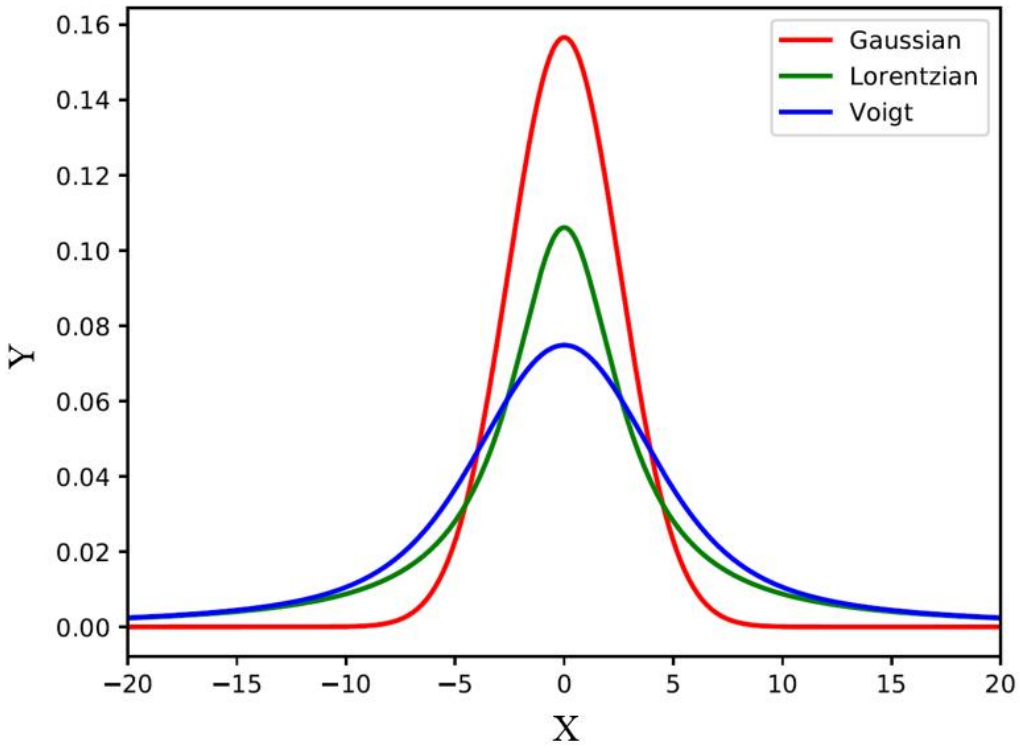

Figure 2.5: Convolution of normalized Gaussian and Lorentzian components (i.e distribution) to form a Voigt distribution. The Gaussian and Lorentzian line shapes are centered at X = 0 and both have a full width half maximum (FWHM) of 5. The area under each curve is unity.

2.4 Auger transition theory

Auger transitions usually follow any kind of inner-shell ionization. The resulting Auger electron often has low energy and is therefore a suitable tool for targeted cancer therapy. In this section the underlying physics of Auger transitions and the classification scheme used in this thesis is introduced.

2.4.1 Auger effect

A vacancy is formed in the atomic inner shell of the residual atom when radionuclides decay by internal conversion (IC) or by electron capture (EC). Afterwards, the excited atom undergoes radiative and non-radiative transitions until the atomic ground state is achieved. For high and intermediate Z elements radiative transitions dominate for K-shell vacancies and cause the emission of a characteristic X-ray. There is a diversity of non-radiative transitions, the most widespread are the Auger, Coster-Kronig (CK) and super Coster-Kronig (super CK) transitions. Non-radiative transitions are the dominant decay mode for vacancies in the L-shell and beyond. An Auger transition is a physical process in which an initial electron vacancy in a lower shell is filled by an electron from a higher shell and another electron is ejected from a higher shell. The electron emitted from the outer shell is called the Auger electron [80, 81]. The notation for the emitted X-ray and Auger electron is often characterised according to the (sub) shells involved during the decays. Consider an Auger transition that involves the filling of an initial vacancy in the X (sub) shell by an electron in the Y (sub) shell, and the decay energy is transferred to an electron in the Z (sub) shell, which is then emitted. The emitted electron is called a XYZ-Auger electron, following the IUPAC notation [82]. Figure 2.6 illustrates of radiative and non-radiative decays which involve the K, L and M shells.

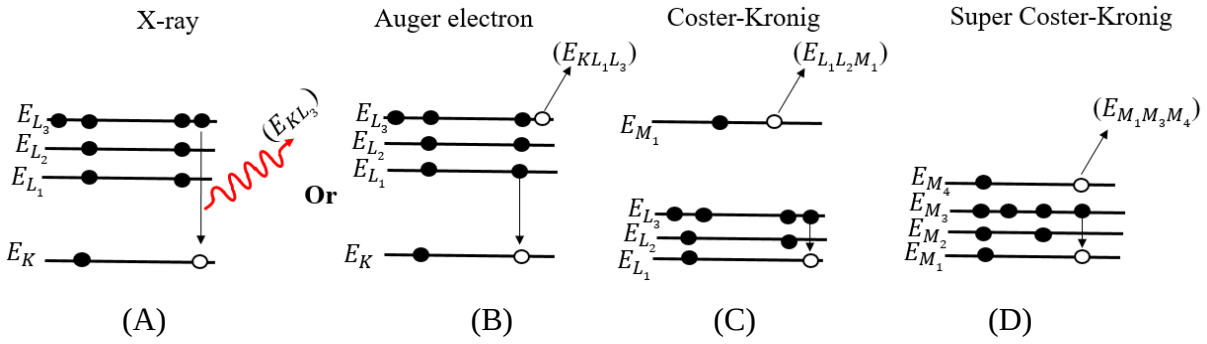

Figure 2.6: Examples of the (A) radiative transition and (B), (C) and (D) non-radiative transition on the basis of atomic level schemes. There are no Coster-Kronig transitions for the K shell.

In Figure 2.6, E_K, $E_{L_{1,2,3,4}}$ and $E_{M_{1,2,3,4}}$ are the binding energies of the K shell, $L_{1,2,3,4}$ and $M_{1,2,3,4}$ subshells, respectively. The E_{KL_3} is energy of the emitted photon while $E_{KL_1L_3}$, $E_{L_1L_2M_1}$ and $E_{M_{1,2,3,4}}$ are the energies of the emitted electrons. In the radiative transition (A), the initial vacancy in the K shell is filled by an electron from the L_3 subshell, and the energy released is carried away by an X-ray with energy E_{KL_3}. In the case of non-radiative transitions (B), (C) and (D), each results in the emission of an orbital electron. These latter processes are likely to happen when the vacancy lies in the L-shell or beyond. In an Auger transition (B), an intial vacancy in a lower energy level is filled by an electron from a higher energy level. For CK (C) transitions, the electron that fills the core hole creates a vacancy in the same shell, however the ejected electron comes from a different shell. Finally, in super CK transitions (C), the vacancy and the two participating electrons are initially all in the same shell [38, 83].

For radiative decay, the X-ray emission has energy:

$$E_{KL3} = E_K - E_{L3}, \tag{2.29}$$

while for non-radiative decay (i.e. Auger electron), the Auger electron has energy:

$$E_{KL2L3} = E_K - E_{L1} - E_{L3}^{*}. \tag{2.30}$$

Here E_{L3}^{*} is the binding energy of an electron in the L_3-subshell with the pressence of a vacancy in the L_1-shell [36]. Radiative transitions propagate the electron vacancy to a higher shell with no change in the number of vacancies. With non-radiative transitions, the vacancy number increases by one.

2.4.2 Atomic relaxation

Atomic relaxation is a multi-step process whereby the inner shell vacancy created during the nuclear decay event propagates towards the outer shell. At each step, the transition rate and the energy released depend on the electronic configuration of the atom. This whole process is known as the "vacancy cascade" or "atomic relaxation cascade". The vacancy cascade arises after the initial vacancy is created and will terminate when all vacancies reach the valence shell, or until no more atomic transitions are energetically possible. The vacancy cascade typically completes within 10^{-16} to 10^{-13} seconds [84, 85]. Figure 2.7 shows an example of a vacancy cascade in xenon following on from K-shell ionisation. It is important to realize that Figure 2.7 presents only one of many possibilities for vacancy propagation. During the atomic relaxation

process, the filling of a vacancy would result in either radiative emission of X-rays or non-radiative Auger transitions. These two procesess are in competition. Thus, the relaxation of an initial vacancy is a multistep process, governed by the X-ray and Auger-electron transition rates. Moreover, due to the large number of possible relaxation paths, the process is stochastic. Hence, a Monte Carlo technique, which relies on random sampling to obtain numerical solutions for complex problems [86], provides a practical way to compute the full relaxation process.

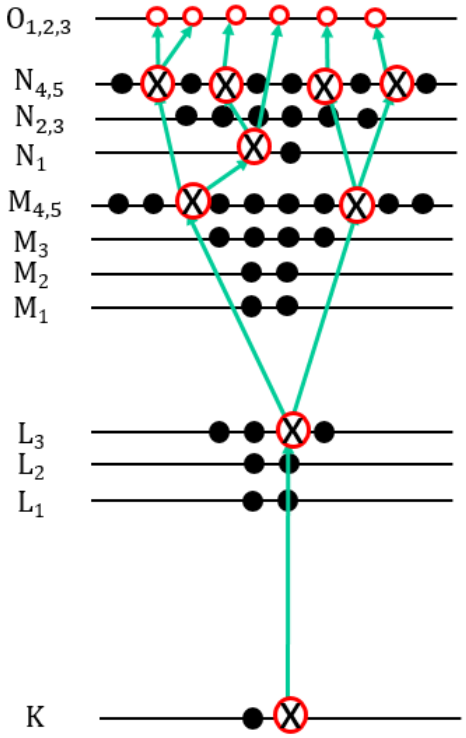

Figure 2.7: An example of a vacancy cascade in ^{125}Te followed by K-shell ionisation, where the electrons are represented by black dots, vacancies by red holes, and filled vacancies by red holes with Xs in them. Six vacancies are represented at the O-shell as a result of this vacancy cascade.

During the propagation of vacancies a large number of Auger electrons can be produced with energy ranging from a few eV to 100 keV. Thus, for Auger therapy purposes, the desired low-energy range of the Auger electrons can be obtained from transitions at the end of the atomic relaxation process. In order to evaluate the Auger spectra after a nuclear decay, it is important to understand the atomic relaxation process in detail. Thus, a computational model, BrIccEmis, was developed at the ANU to describe the full atomic relaxation process using a Monte Carlo approach [65]. A brief description of BrIccEmis is presented in section 2.5.

2.4.3 Transition rate

The rate of total decay (denoted by A) of an excited state is the inverse to its lifetime (denoted by τ): $A = \tau^{-1}$. According to the Heisenberg uncertainty principle, the total rate of decay can be linked to the width of the energy level (Γ) of that state by employing the following equation $\Gamma = A\hbar$, where $\hbar$ is the reduced Plank constant. To achieve the total level width of the excited state, the radiative width denoted by Γ_R the, Auger width denoted by Γ_A and the Coster-Kroing width denoted by Γ_{CK} is summed as shown in the equation below:

$$\Gamma = \Gamma_R + \Gamma_A + \Gamma_{CK}\,. \tag{2.31}$$

It is necessary to express the quantity of the transitions rates as a fraction of the total transition rate. Thus, in order to express the transition in fraction form the fluorescence yield ω, the Auger yield a, and the Coster-Kronig yield f, are introduced as defined below [87]:

$$\begin{aligned} \omega &= \Gamma_R/\Gamma \\ a &= \Gamma_A/\Gamma \\ f &= \Gamma_{CK}/\Gamma. \end{aligned} \tag{2.32}$$

In this thesis the yields which involve the filling of vacancies in the K-shell will be discussed because the way that the fluorescence rate influences the KLL-Auger can be easily explained. For LLM-Auger fluorescence the rate is still important but it is best calculated using a Monte Carlo approach, hence not discussed here.

The K-shell does not have a subshell and therefore CK transitions will not occur for a K vacancy. Considering the mentioned scenario, the summation of a K fluorescence yield ω_K and K-Auger yield a_K is unity, such that:

$$\omega_K + a_K = 1. \tag{2.33}$$

In order to calculate the total number of the initial vacancies n_K in the K shell resulting from the nuclear decay, the equation below is used:

$$n_K = I_{EC}P_{EC,K} + P_\gamma\alpha_K, \tag{2.34}$$

where I_{EC} represents the electron capture intensity, $P_{EC,K}$ is the K-shell capture probability, P_γ describes the probability of the decay path (for ^{125}Te there is only one decay path, so P_γ=1), and α_K is the conversion coefficient of the K shell.

Extensive research has been conducted on the K fluorescence yields for a wide range of nuclei [88-90]. By looking at the available experimental data, a systematic behaviour in the yields can be observed, as shown in Figure 2.8. The observed trend has been approximated reasonably well by several authors [87, 88, 91] using different semi-empirical formulae.

$$\omega_K = \frac{Z^n\,\omega_{max}}{k^n + Z^n} \qquad (a)$$

$$\left(\frac{\omega_K}{1-\omega_K}\right)^{\frac{1}{4}} = \sum_{i=0}^{3} b_i Z^i \quad (b) \qquad (2.35)$$

$$\left(\frac{\omega_K}{1-\omega_K}\right)^{1/3.5} \sum_{i=0}^{3} c_i Z^i \quad (c)$$

These semi-empirical models were described and compared in detail by Kahoul et al. [88].

where Z is the atomic number, ω_K is the K fluorescence yields and ω_{max}, k, n, b, c are parameters to obtain K fluorescence yields from a global fit to the data.

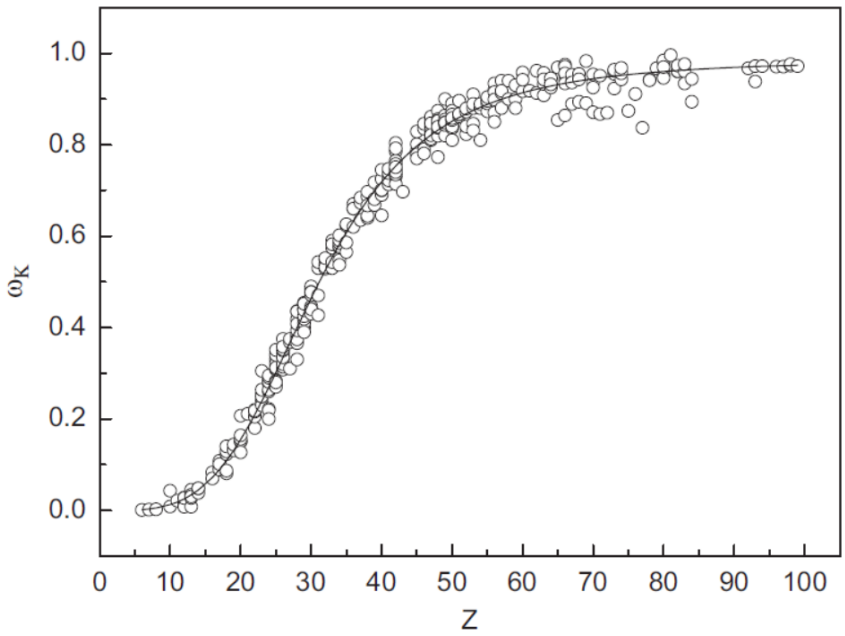

Figure 2.8: Distribution of experimental K fluorescence yields, ω_K as a function of atomic number, Z. The trend of the measurement data (circles) is described reasonably well with semi-empirical equation $2.35(a)$. Image was extracted from [88].

2.4.4 Shake process

The removal of an atomic electron will always take place during the following processes: electron capture, internal conversion, and non-radiative decays. In the event of core electron removal, there is a sudden change in central potential as observed by the valence electrons, which can result in the excitation of an outer atomic electron into a free electron state (shake-off), or into an unoccupied bound state (shake-up). The process described above is normally referred to as the *shake process* [92]. This thesis does not consider the shake-up process because all measured quantities in the experiment do not incorporate the valence electrons.

2.4.4.1 Shake-off probabilities

The probability of the shake electron being created is often calculated in the high energy limit, where the sudden approximation applies [93, 94]. In this approximation, electron shake-off depends only on the initial and final states. Therefore, the probability of shake occurring can be expressed as the overlap integral between the initial state ψ_i and final ψ_f wave functions of the shake electron as shown in the equation below:

$$P_{i\to f} = \left[\int \psi_f^* \psi_i \, dt\right]^2 \tag{2.36}$$

It is worth noting that the calculations involving the shake probabilities are obtained on the basis of single-configuration wave functions and do not take electron-electron correlation into account. Figure 2.9 shows the shake energy distribution of neon due to photo-ionization.

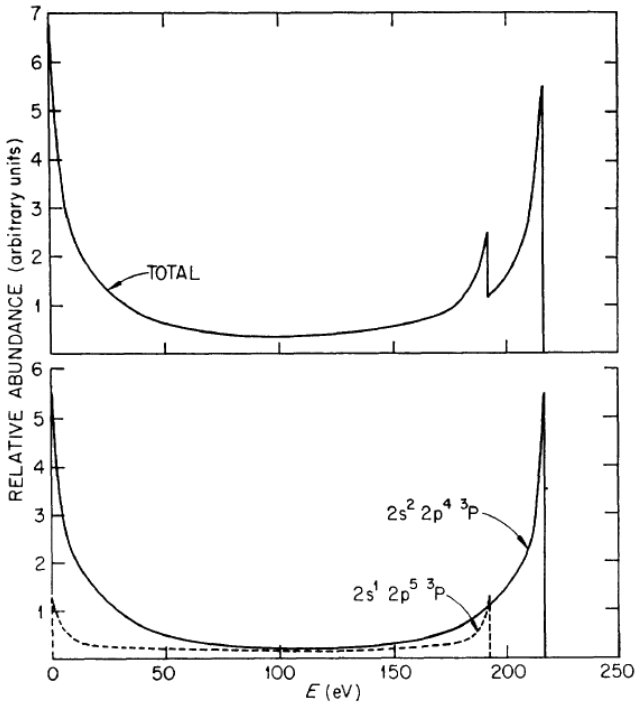

Figure 2.9: Energy distribution of multiple electron ejections from the outer shell of neon due to photoionisation of the L-shell. The bottom panel shows the contributions from the simultaneous ionisation of two electrons from the $2p$ subshell and one each from the $2s$ and $2p$ subshells, and the upper panel shows the sum of these contributions. Image was taken from [95].

The shake probabilities were only calculated for closed shell (noble) atoms in the past [92, 96, 97]. More recently, Lowe et al [98] calculated the shake probabilities for transition metals, which contain open $3d$ shells, by employing multi-configration wave functions. Their results agree much better with the experimental results when compared to any previous work, and this comparison is presented in Figure 2.10. The shake probabilities calculated by Lowe et al. are generally higher than in previous models, indicating that the electron-electron correlation can increase the shake probabilities for open shell atoms, such as tellurium [65].

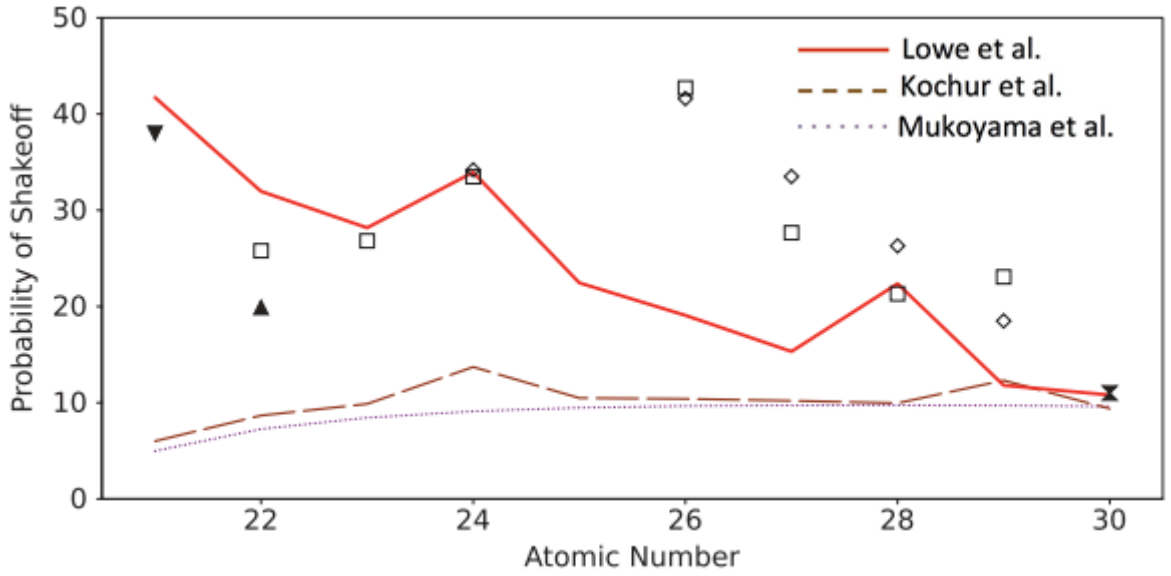

Figure 2.10: Theoretical shake-off probability for transition metals by Lowe et al.[98] (red solid), Krochur et al. [96] (brown dashed line), and Mukoyama et al.[97]. Note that the symbols ▲, ▼, □ and ◊ represent the experimental data [99-102] respectively. The comparison shows that the Lowe et al. model agrees much better with experimental results than other models, highlighting the importance of the inclusion of electron-electron correlation to open shell atoms. Image extracted from [98].

2.4.4.2 Shake energy distribution

In our case, there can be shake off after the conversion electron decay or after each step of the Auger. The energy distribution of shake-off electrons occurs as a result of a sudden vacancy created by internal conversion or photoionisation and can be represented by [65]:

$$h\nu = E_i + E_0 + E_e + E_s, \tag{2.37}$$

where $h\nu$ is the γ-energy, E_i represents the ionisation potential for removing the first electron (conversion electron or photoelectron), E_0 is the threshold energy for electron shake-off to occur, which can always be estimated by the binding energy of the electron that is shaken off, and E_e and E_s denote the (kinetic) energies of first emitted electron and shake electron, in that order. Note that the quanitities $h\nu$, E_i and E_0 are fixed, hence the shake electron shares energy with other emitted electrons, which causes a continuous energy distribution from zero energy up to $h\nu - E_i - E_0$ [103]. Consequently, the shake-off process will produce very low energy

electrons. Thus, proper understanding of the shake effects is needed for Auger applications to a highly-targeted therapy.

In the case of Auger electrons, the situation is slightly different as there is no $h\nu$ (no clear energy level), so it easiest to refer to the energy of Auger electron with shake to the energy of the electron without shake [65]:

$$E_A^S = E_A - E_0 - E_s, \tag{2.38}$$

where E_A^S and E_A are the Auger energy with and without the shake-off process.

An illustration of the shake energy distribution is shown in Figure 2.9. Note that in the actual experiment, the energy distribution shown in Figure 2.9 will be folded with a Gaussian line shape because of the instrumental broadening effect. By doing so, the shake effect will produce an asymmetric peak with a longer tail seen at the low-energy side. This effect is critical in the analysis of the current experimental work.

2.4.5 Atomic structure effect

Vacancy creation through electron capture and internal conversion processes will temporarily leave an atom in one of several configurations. Electron capture decay will leave the atom with atomic number Z in the electron configuration of an atom with atomic number $Z + 1$, which decays afterward to a lower-energy state. After an electron capture decay, the vacancy cascades could occur too quickly (10^{-15} s) for valence electrons to rearrange into their (new) electronic ground state. As a consequence Auger transitions after electron capture and internal conversion, respectively will have slightly different kinetic energies. This is called the atomic structure effect [104]. Such an atomic structure effect was established experimentally for LMM-Auger electrons after electron capture decay of ^{131}Cs by Kovalik et al. [105]. It was found that the shift in energy as a result of the effect was (9.4 ± 1.1) eV. Practically, this phenomenon means that each measured Auger peak could have contributions from two peaks originating from electron capture and internal conversion, with a small energy separation.

2.4.6 Classification for the *KLL* Auger electrons

The KLL-Auger electrons were measured in this experiment and it was found more peaks than expected in the jj-coupling scheme. Hence, here the intermediate coupling scheme for this group of electrons is introduced. An Auger transition will change the initial state of an excited atom from a single to a double hole state ($1^+ \rightarrow 2^+$). Therefore the kinetic energy of the emitted Auger electron is directly related to the final state energy of the atom, which is dependent on the interactions between the residual electrons. Thus, different types of interactions between electrons will result in slightly different energies of the emitted Auger electrons from the corresponding subshells, hence causing splitting in the measured Auger lines [106].

The spin-orbit interaction requires that the total angular momentum is conserved. For each electron the total angular momentum is described by the equation below:

$$j = l + s. \tag{2.39}$$

In the absence of the spin-orbit interaction (or if it is very small), the electrostatic interactions between electrons are described by the total orbital angular momentum L, and the total spin angular momentum S, which are defined as:

$$L = l_1 + l_2 + l_3 + \cdots \tag{2.40}$$

$$\mathrm{S} = s_1 + s_2 + s_3 + \cdots \tag{2.41}$$

The interactions between electrons will couple all these angular momenta together, with the restriction that the total angular momentum (of the final state) $J = L + S$ must be conserved. When the electrostatic interaction between electrons dominates over the spin-orbit interaction, the total orbital angular momentum L and total spin S are conserved separately. This is known as the LS-coupling, which leads to three possible KLL Auger lines:

$$KL_1L_1,\ KL_1L_{2,3} \text{ and } KL_{2,3}L_{2,3} \tag{2.42}$$

On the other hand, when the spin-orbit interaction dominates over the electrostatic interaction between electrons, the spin s and orbital angular momentum l of each electron couple to form a total angular momentum j, this is known as jj-coupling. In the jj-coupling limit, there are six KLL Auger lines:

$$KL_1L_1,\ KL_1L_2,\ KL_1L_3,\ KL_2L_2,\ KL_2L_3 \text{ and } KL_3L_3. \tag{2.43}$$

Heavy nuclei can be described better under the jj-coupling scheme while light nuclei are described better under the LS-coupling scheme. For interactions lying between pure *jj*-coupling and LS-coupling, the total angular momentum J of the final state is conserved but not necessarily the total orbital angular momentum L and total spin S. This is known as intermediate coupling. The intermediate coupling scheme leads to nine possible KLL Auger lines [107]:

$$KL_1L_1(^1S_0),\ KL_1L_2(^3P_0),\ KL_1L_2(^1P_1),\ KL_1L_3(^3P_1),\ KL_1L_3(^3P_2), \tag{2.44}$$

$$KL_2L_2(^1S_0),\ KL_2L_3(^1D_2),\ KL_3L_3(^3P_0) \text{ and } KL_3L_3(^3P_2). \tag{2.45}$$

The notations S, P, D indicate the total orbital angular momentum of that state, while the superscripts 1 and 3 indicate the singlets ($S = 0$) and triplets ($S = 1$) states of the electrons, respectively. The subscripts $0, 1, 2$ indicate the total angular momentum J of that state. Detailed descriptions of these states are beyond the scope of this thesis.

2. 5 Theoretical model - BrIcc and BrIccEmis

The main objective of this thesis is to determine the Auger yield accurately and then test the theoretical model against the measured yield. To achieve this, a computational model was employed to compare the experimental results with the theoretical ones. The model mentioned above is known as BrIccEmis, which uses the distribution of the vacancies as calculated by BrIcc as starting point and add the relaxation process to it.

A- BrIcc

This program was developed by Kibédi et al. [69] with the aim of calculating the conversion coefficients for a range of nuclei with selected transition energies multipolarities and mixing ratios e.g., see Figure 2.11. The input data, which is required to evaluate the conversion coefficients, is taken from Evaluated Nuclear Structure Data File (ENSDF) which contains the latest evaluated nuclear data [108].

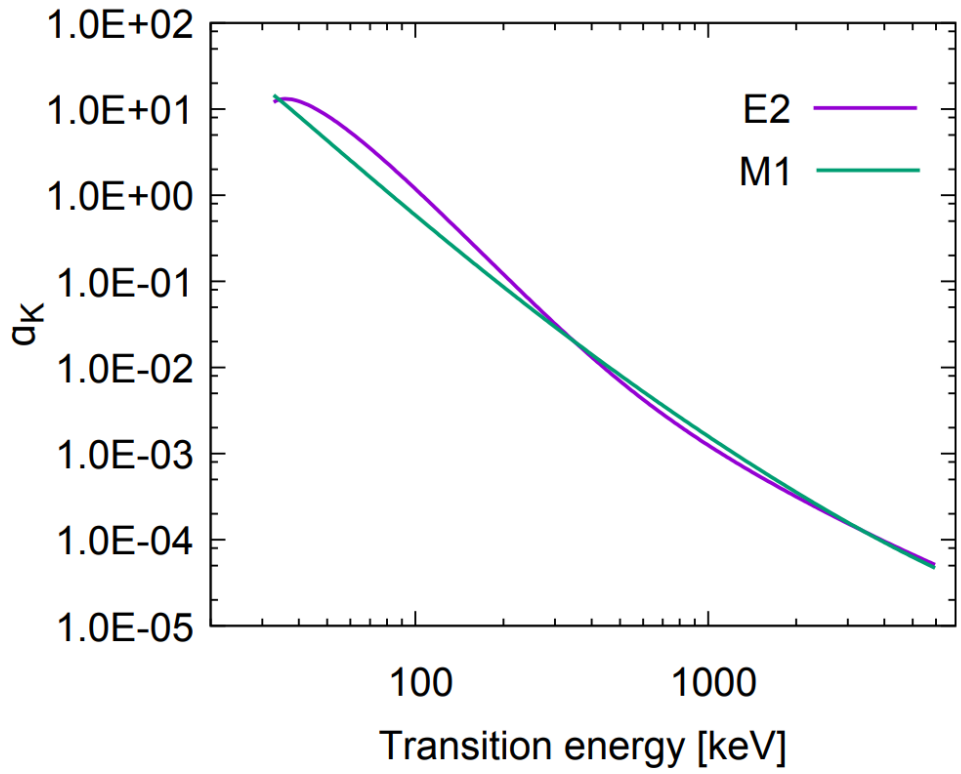

Figure 2.11: K-conversion for $M1$ and $E2$ in tellurium (Z=52) calculated by BrIcc. In our case the transition energy is 35.5 keV, the transition is almost exclusively $M1$ and hence α_K is 11.6.

B- BrIccEmis

This is the recent program developed at the ANU by Lee [65]. It can calculate the full atomic non-radiative spectrum from a nuclear decay. It is worth noting that this algorithm makes use of the Monte Carlo method [86] when calculating the Auger and X-ray spectra. To realize the complete atomic processes during the BrIccEmis calculations, the initial state after the nuclear decay process must be simulated. Furthermore, the propagation of atomic vacancies at each step is chosen at random from atomic transitions present by using the respective transition rates as the weighting factors. BrIccEmis can be run with two different assumptions: (a) vacancies reaching the valence band are taken to neutralize straight away. This called "condensed" model. (b) The vacancies are all in the valence shell and a multiply charged ion is formed in the final state with a charge state corresponding to the total number of Auger and conversion electrons emitted. This is "the isolated atom" model.

For the mentioned assumptions, the following input data is required: the nuclear structure data, internal conversion coefficients, capture probabilities, transition probabilities, and transition energies.

The nuclear structure data such as half-life and properties of level states are extracted from ENSDF based on routines from BrIcc [69]. Moreover, the internal conversion coefficients are extracted from BrIcc, with the general precision of better than 2% [108]. The probabilities of electron capture are evaluated using the Schönfeld methodology [109]. For ^{125}I, Schönfeld approximated the uncertainties in the K and L capture rates to fall below 0.3% and 2%, in that order. The Evaluated Atomic Data Library (EADL) database provides the atomic transition rates [110], which are realized through the calculations in the jj-coupling scheme.

The accuracy of the calculated radiative and non-radiative transition (except the CK transition) rates are reported to be better than 10% and 15%, respectively, while the error in the CK transition rates can be up to 100% [110]. Finally, the binding energies that are required to evaluate the transition energies are calculated in the jj-coupling scheme, using the RAINE code [111]. In summary, the theoretical model has proved satisfactory in a series of radioisotopes [112, 113]. On the other hand, the transition energies were found to deviate, particularly for the ones having higher atomic numbers. This scenario can be attributed to the absence of the Breit electron interaction and the quantum electrodynamics corrections (QED) [114] in the RAINE code. In addition, BrIccEmis includes the atomic structure effect as described in section 2.4.5 by considering electron capture and internal conversion as separate processes. Finally, it is

important to note that the calculated shift in energy due to the atomic structure effect was approximately 10 eV according to BrIccEmis.

In this thesis, the Auger and conversion electron spectra from the electron capture decay of ^{125}I were measured within the energy range from 2 to 36 keV. The expected line spectra (without the natural broadening effect) were calculated using BrIccEmis code as shown in Figure 2.12. In an actual experiment, these lines will be folded with the line shapes and widths due to the instrumental resolution, the natural lifetime broadening, the shake-off processes and other effects [115]. Moreover, it should be noted that the shake effect was neglected in the BrIccEmis calculations, since it is at present not well understood.

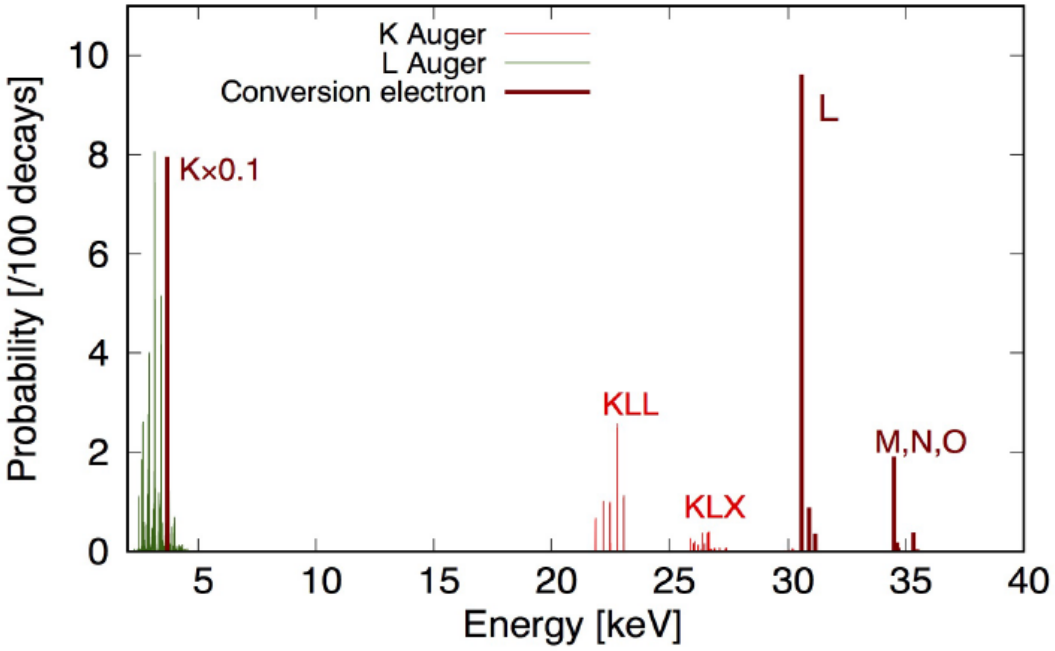

Figure 2.12: Calculated line spectra for the electron capture decay of ^{125}I from BrIccEmis. The Auger and conversion electrons are labelled in the spectra. The K-conversion line has been scaled down by a factor of 10, and note the KLX-Auger lines include the KLM and KLN Auger lines.

2. 6 Decay scheme of ^{125}I

The decay scheme of ^{125}I is shown in Figure 2.13. ^{125}I decays in 100% of the cases to the 35.5 (5) keV level in ^{125}Te via electron capture, with a decay energy of Q_{EC}= 185.77 (6) keV. After that, the excited state of ^{125}Te will decay to its ground state, by releasing 35.5 (5) keV energy either by emitting a conversion electron or a gamma ray. The 35.5 (5) keV transition, from an initial state with spin-parity of $J_i^{\pi} = 3/2^+$ to a final level state with spin-parity of $J_f^{\pi} = 1/2^+$, can only be of type $M1 + E2$, according to the selection rules. The mixing ratio of the $E2$ to $M1$ multipolarity transitions was suggested to be $\delta = 0.03$ [116]. Moreover, in 7% of the cases the excited state of ^{125}Te decays to its ground state by γ-ray emission.

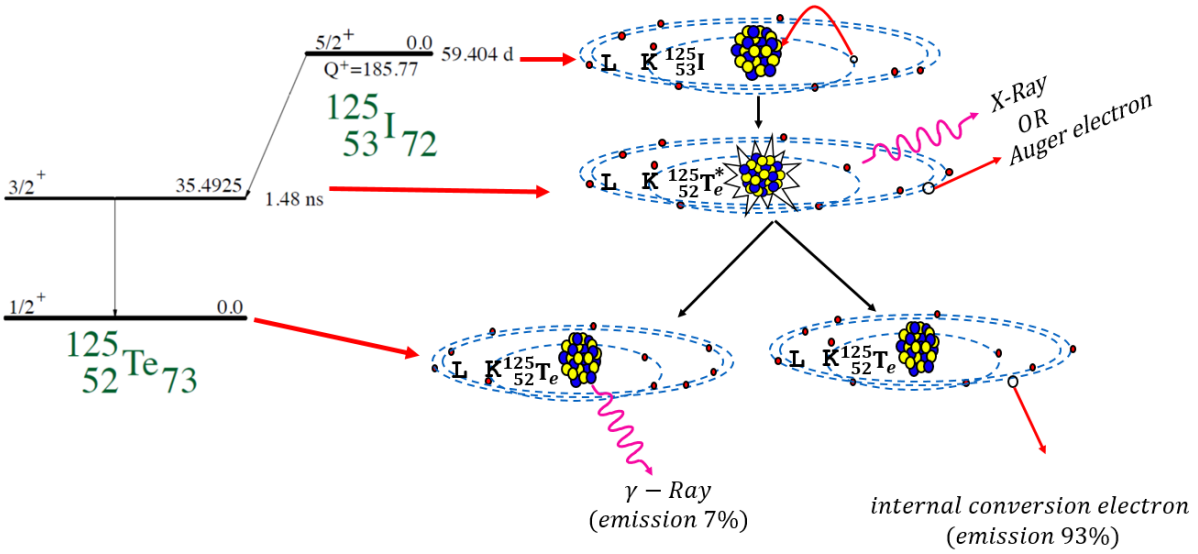

Figure 2.13: Decay scheme of ^{125}I radionuclide. ^{125}I decays with a 59.4 (28) day half-life, to the ground state of ^{125}Te in two steps. In the first stage ^{125}I decays by electron capture to the $3/2^+$ excited state of ^{125}Te which has a half-life of 1.48 (8) ns. This is followed by a transition to the ground state of ^{125}Te via either internal conversion with a probability of 93% or gamma emission with a probability of 7% of tellurium atom decay. As a result of each EC and IC event, a vacancy is created in an inner atomic shell of the tellurium atom. The resulting ionised atom is unstable and thus leads to a complex number of radiative and non-radiative transitions.

The initial vacancy distribution of ^{125}I after electron capture and internal conversion processes is presented in Table 2.3. In the table, the capture probabilities I_{EC} were extracted from BrIccEmis calculations following methodology by Schönfeld [109], whereas the conversion electron emission rates I_{CE} were calculated by adopting the conversion coefficients from BrIcc and a mixing ratio of $\delta = 0$. Note that some of the subshell capture probabilities are not presented in Table 2.3, as they are negligible contributions relative to other subshell capture probabilities [117].

Table 2.3: Initial vacancy distribution from the electron capture and internal conversion processes of the decay of ^{125}I. Where P_{EC} is the capture probability, and P_{CE} is the conversion electron emission rate.

Atomic Subshell	Probability per decay		
	P_{EC}	$P_{CE}(\delta = 0.03)$	$P_{CE}(\delta = 0)$
K	0.80	0.79492	0.79492
L_1	0.15	0.096084	0.096084
L_2	0.0042	0.008935	0.007684
L_3	-	0.003713	0.001924
M_1	0.035	0.01904	0.01904
M_2	0.0010	0.001877	0.001612
M_3	-	0.000779	0.000402
M_4	-	2.13×10^{-05}	1.8×10^{-05}
M_5	-	1.68×10^{-05}	1.29×10^{-05}
N_1	0.0078	0.003794	0.003794
N_2	0.00022	0.000346	0.000299
N_3	-	0.000143	7.38×10^{-05}
N_4	-	3.32×10^{-06}	2.82×10^{-06}
N_5	-	2.59×10^{-06}	1.99×10^{-06}
O_1	0.00048	0.000421	0.000421
O_2	-	2.7×10^{-05}	2.33×10^{-05}
O_3	-	1.07×10^{-05}	5.51×10^{-06}
Sum	1	0.930135	0.926318

Now that a better understanding of the nuclear decay processes of ^{125}I is available, it is clear why ^{125}I is a suitable candidate for targeted therapy. This is because ^{125}I decays by electron capture with a probability of 100%, and decays further by internal conversion with a probability of 93% (see Table 2.3) to the stable ^{125}Te. Thus, almost always two successive vacancy cascades occur per decay of ^{125}I, which could result in about 20 Auger electrons [38] ranging in energy between 0 eV and 34 keV (interaction sites of ~10 to 100 nm) being emitted. For this reason, the ^{125}I is a very effective Auger electron emitter.

2. 7 Summary

In summary, the necessary background for idoine-125 decay was discussed in details in this chapter. In particular, the concepts of electron capture probability, selection rules, mixing ratio, conversion coefficient and penetration effect as well as the Auger transition and physical process that produces Auger electron were also presented. In addition the computational models (BrIcc and BrIccEmis), that will be used to compare with the measurement were introduced.

Chapter 3

Experimental Methodology

The primary components of most Auger Electron Spectroscopy (AES) systems are: (i) the electron gun, (ii) the ion gun used to sputter the sample surface, (iii) the electron energy analyser and (iv) the detector. In our case, owing to the use of a radioactive source (^{125}I), only three components are required: the radioactive source, the electron energy analyser, and the detector. In this chapter, the details of the experiment to measure the Auger and conversion electrons are discussed.

3.1 Source preparation and activity

An initial attempt at measuring Auger-electron emission from ^{125}I was made using a source prepared using a procedure from papers published in the late 1960s, based on the formation of silver iodide on a silver surface [48]. In this source iodine reacts with silver forming silver iodide. From the known activity of the source (326.89 MBq) and dimension of the silver substrate, the thickness of the silver iodide was calculated and found to be 0.04 μm, which was larger than the inelastic mean free path λ(E) at low energies (< 4 keV) and hence most of the emitted electrons are in the background rather than in the peak itself. It also was found that the background level increased quite significantly within one week to the level that the experiment had to be stopped. This indicated that the silver iodide sample was not chemically stable, particularly in high vacuum, and therefore another approach was required. For this experiment, ^{125}I sources were prepared by ANSTO (Australian Nuclear Science and Technology Organisation) by allowing iodine in the form of a NaI solution to be deposited onto a gold substrate, following the methodology described in the literature [53]. ^{125}I can be prepared as a sub-monolayer source on a Au (111) surface, which is stable in air [118].

Before radiolabeling with ^{125}I, the gold substrate was annealed in order to produce a (111) surface structure to allow iodine adsorption. This was done by annealing a thin Au layer on a SiO_2 substrate using a butane torch until a dull, red glow of the sample was observed. For this a dark room was used to enable observation of the glowing color and to avoid the risk of overheating the sample. The annealing process was repeated three times. The Au was left to cool for 30 seconds after each annealing process. A droplet containing NaI in a NaIOH solution

(pH ≈ 10, from Perkin Elmer) was then deposited on Au surface, and allowed to become adsorbed. In this way an approximately 4 mm diameter source was obtained with an activity of 5 MBq. The resulting source was a third of a monolayer of ^{125}I on top of the gold substrate, thus making low-energy measurements possible.

The activities of the iodine sources were measured using a high purity germanium (HPGe) detector at the ANU. The key results are presented in Table 3.1. A picture of the iodine source is shown in Figure 3.1.

Table 3.1: ^{125}I activity determination from the experiment for two ^{125}I samples. Note that the (EMS) and (super-CMA) specify the spectrometer in which the iodine sources were measured.

	Activity (MBq)
^{125}I (EMS)	4.2 ± 0.4
^{125}I (super-CMA)	4.7 ± 0.4

The activity distribution of the iodine source was also determined experimentally by moving the source over a 0.5 mm diameter hole in a 3 mm thick lead sheet on top of the HPGe detector, and detecting the corresponding γ-ray yield. The analysis result is shown in Figure 3.2, which suggests the activity distribution of the ^{125}I source is quite homogeneous over a 2 mm diameter circle located at the centre of the Au layer.

Figure 3.1: A third of monolayer of ^{125}I on a gold substrate. Note that the circle has diameter of 5 mm, which is the activity region that gives most radiation from ^{125}I atoms.

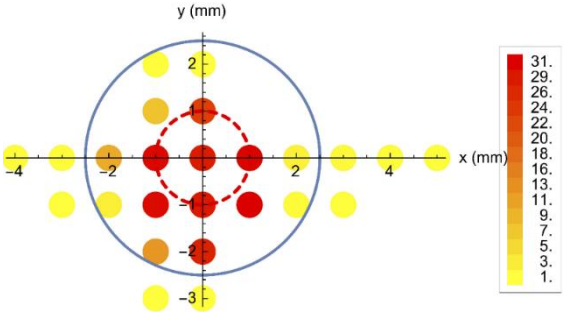

Figure 3.2: Activity distribution of ^{125}I source (super-CMA). Scaling number represents the relative activity at different regions of the source, while the scaling number 1(yellow) is the activity contributed from the background. The blue circle represent the actual size of the source, and the red dashed circle represents the deduced homogenous activity region. Note that each measurement step is 1 mm.

Acknowledgment

I would like to thank Mr Bryan Tee for providing me the Figures 3.1 and 3.2.

3.2 Description of spectrometers

Two types of electron spectrometer are currently used in the Electron Spectroscopy Laboratory, ANU (Australian National University) to measure Auger electron spectra. One is a modified Cylindrical Mirror Analyser (super-CMA). Modifications to extend the measurement energy range to 4 keV and to shield the detector from gamma and X-radiation were carried out in-house. The energy measurement extension from 2.5 keV to 4 keV is of particular importance, as it allows the instrument to cover not only very low-energy Auger electrons, but also the more energetic L-Auger decays which precede these in the cascade. Additionally, this instrument is capable of measuring the L-Auger electrons together with the K-conversion line generated from the electron capture (EC) decay of ^{125}I. Results of these measurements are presented in chapter 6.

The other instrument used was a hemispherical electron analyser, developed for high-resolution Electron Momentum Spectroscopy (EMS) which can measure electrons up to 40 keV in energy. It has a small opening angle (~ 0.1% of 2π) and the ability to measure a range of energies simultaneously (up to 200 eV). Thus, with this single instrument, the L, M, N conversion lines and KLL, LMM Auger groups can be measured as shown in chapters 4, 5 and 6.

3.3 Design and principle of the super-CMA

The Cylindrical Mirror Analyser (super-CMA) was made by Staib Instruments [119]. A schematic view of the spectrometer is included in Figure 3.3. There is a circular grid (4), inserted just in the front of the spectrometer that remains at ground potential. The main purpose of this grid is to isolate the field in the first stage (A) of the analyser and the field-free region outside the analyser. The spectrometer consists of a two-stage (A) and (B) CMA. The first stage (A) is comprised of a pair of coaxially spaced metal cylinders: inner (1) and outer (2). A negative voltage is applied to the cylinder (2) and a somewhat smaller negative voltage is applied to the cylinder (1). As a consequence, electrons entering the space between the cylinders are decelerated and deflected towards an intermediate aperture (3) which is held at ground potential. This aperture is situated axially, and separates the two stages of the analyser. Auger electrons pass from the source through this aperture, if their energies are within a broad energy band selected by the first stage of the analyser. A more precise energy selection occurs in the second stage (B).

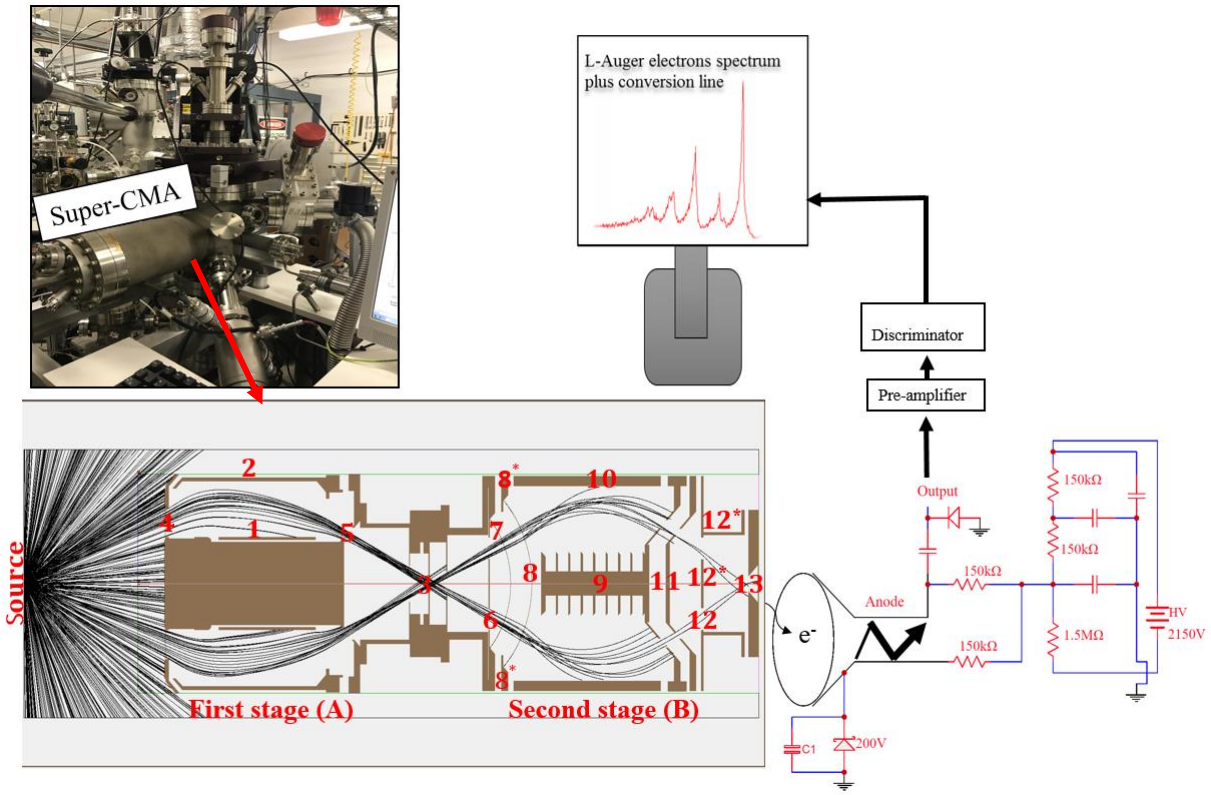

Figure 3.3: Schematic and photograph of Auger experiment setup. The black curve represents the trajectory of the emitted electron from the 4 mm diameter iodine source at 100 eV pass energy.

A quasi-annular slot (4), which is held at ground potential, is necessary to permit entry of the electrons, whose trajectories are under analysis, into the radial electric field space between cylinder (1) and (2). Another quasi-annular slot (5) permits the exit of the same electrons from the radial electric field. Similarly, holes (6) and (12) serve the same purpose at the second stage of the analyser (B).

There are two grids located at the entrance of the second stage. When the electrons pass through these two grids, their kinetic energy is changed (usually decelerated) to the Pass Energy (PE). If there are low energy electrons, they will be accelerated to the PE. For example, if the PE is 100 eV and a 50 eV electron is to be measured, that means the electrons must accelerate from 50 to 100 eV when they go through the grids. In summary, the PE can be defined as a user-controlled quantity used to select the energy of the electrons in the second stage, which determines the energy resolution of the spectrometer.

When the analyser is operated at constant PE mode then potentials (8,9,10,12 and 13) all change when the scanned voltage is changed. In this retardation mode of operation, the spherical grid (7) nearest to the intermediate aperture (3) is held at ground potential while the second grid (8) is at the retarding voltage. Thus, the electrons are decelerated by these two grids and then deflected toward the quasi-annular slot (12). Subsequently, electrons are accelerated to the final aperture (13). The final aperture (13) is a simple circular hole placed on the axis of the CMA. The dimension of this aperture sets the energy resolution. The spectrometer is protected from the earth's magnetic field by a coaxial cylinder, made of mu-metal placed inside the vacuum chamber around the analyser. Furthermore, this analyser, which is made mainly of aluminum, is compact and fits through a standard CF 100(6" OD) flange. Figure 3.4 shows the dimensions of the super-CMA.

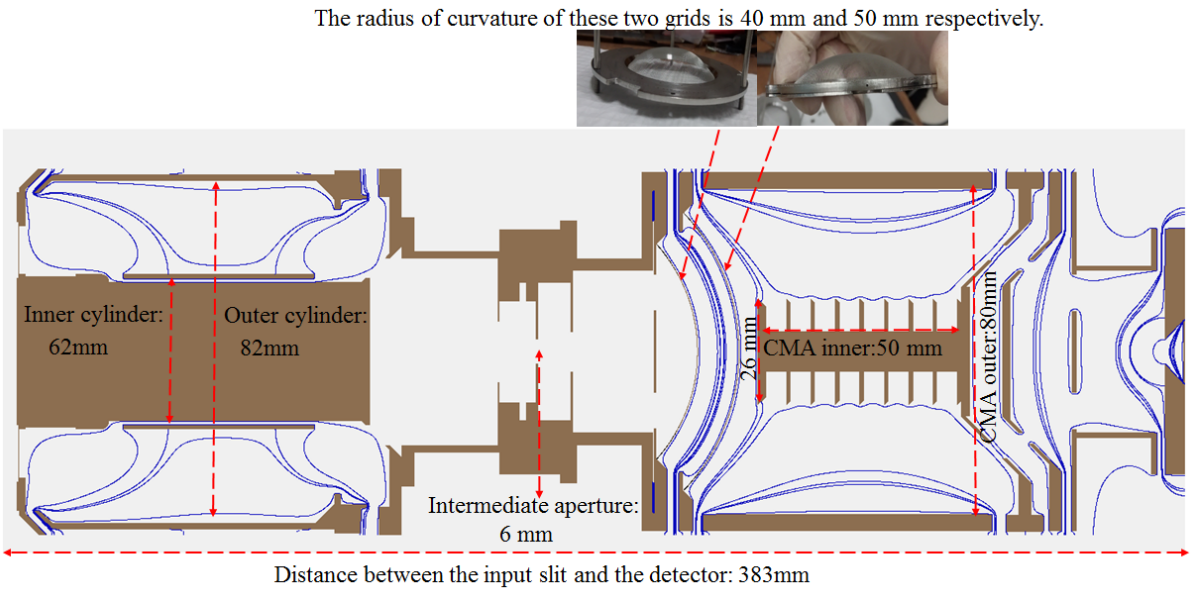

Figure 3.4: Dimensions of the super-CMA. Blue lines represent the electrostatic field lines calculated in SIMION simulation.

Figure 3.5 shows an overview of the analyser control electronics. All voltages required by the analyser are supplied via a single cable attached to a multi-pin feedthrough located on the vacuum flange. Each connection, with its designation, is given in Table 3.2.

All voltages are derived from two power supplies. One power supply (the scanning power supply, V_{scan}) is set to the energy of the electron one wants to measure. The inner and outer cylinder of the first stage are set to a fraction of this power supply, using a resistive divider. The second power supply has an output voltage that is equal to the nominal pass energy of the second stage. A resistive divider is used to tie a fraction of the floating power supply (V_{float}) output to the scan voltage, see Figure 3.5. Within the second stage of the analyser, the electrons are decelerated and electrons with a certain kinetic energy inside this second stage are transmitted. All applied voltages after electron deceleration, are relative to the deceleration potential. Therefore, a floating power supply is required. The voltages for the second stage are then derived from this floating supply (Pin1, Pin 2, Pin 3, Pin 4 and Pin 7).

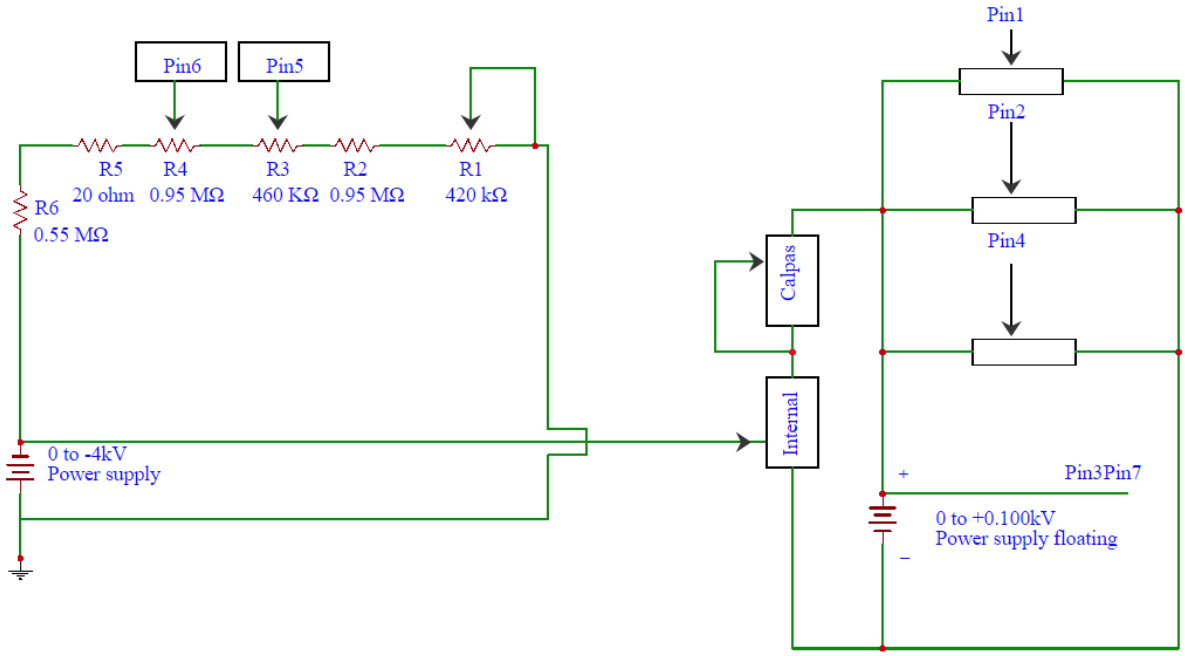

Figure 3.5: Schematic of super-CMA control electronics (see main text for more details).

Table 3.2: An overview of the cable connecting the analyser with its power supply, including designations. The complete wiring schematic of super-CMA control electronics is given in Figure 3.5.

Pin number	Applied Voltage on	Reference number in Figure 3.3	$V_{\text{scan}} \pm X\, V_{\text{float}}$ [(a)]
1	Trim	12	$V_{\text{scan}} - 0.043 \times V_{\text{float}}$
2	CMA inner stage (B)	9	$V_{\text{scan}} - 0.442 \times V_{\text{float}}$
3	Exit slit	13	$V_{\text{scan}} - 0.606 \times V_{\text{float}}$
4	CMA outer stage (B)	10	$V_{\text{scan}} - 0.135 \times V_{\text{float}}$
5	Inner cylinder stage (A)	1	$0.6039 \times V_{\text{scan}}$
6	Outer cylinder stage (A)	2	$0.6897 \times V_{\text{scan}}$
7	Retard	8	$V_{\text{scan}} - 0.605 \times V_{\text{float}}$

(a) Where: V_{scan} is a negative voltage, X is different for different pins and V_{float} is a positive voltage.

3.3.1 Obtaining an estimate of the efficiency of super-CMA

Quantifying the transmission function (analyser efficiency) of the super-CMA for different incoming electron energies is difficult. To our knowledge, Gergely et al. [120] are the only group who have attempted to determine the efficiency of a spectrometer of the same type (DESA 100 CMA of Staib Instruments) experimentally in 1999. As mentioned in section 1.2, the aim is to determine the number of Auger electrons emitted per nuclear decay, based on the measurement of the number of K-conversion electrons per nuclear decay, which is well known. Therefore, by comparing the conversion electron intensity to the Auger electron intensity, the number of Auger electrons per nuclear decay can determined. However, generally they are not of the same energy, and hence at least the relative efficiency of the analyser at these energies must be known.

Three approaches were used to help reach the goal of quantitative understanding of the spectrometer response: (a) SIMION simulation, (b) comparing elastic peak intensities at different incoming energies, and (c) comparing different Auger signals. The last two used an electron beam.

For the latter two experiments, it is of course important that the beam current is known precisely. For this purpose the beam current was measured using a Faraday cup, which is known to be one of the more precise beam current measurement tools. A schematic diagram of the Faraday cup, which was added to the ultra-high vacuum manipulator, is shown in Figure 3.6.

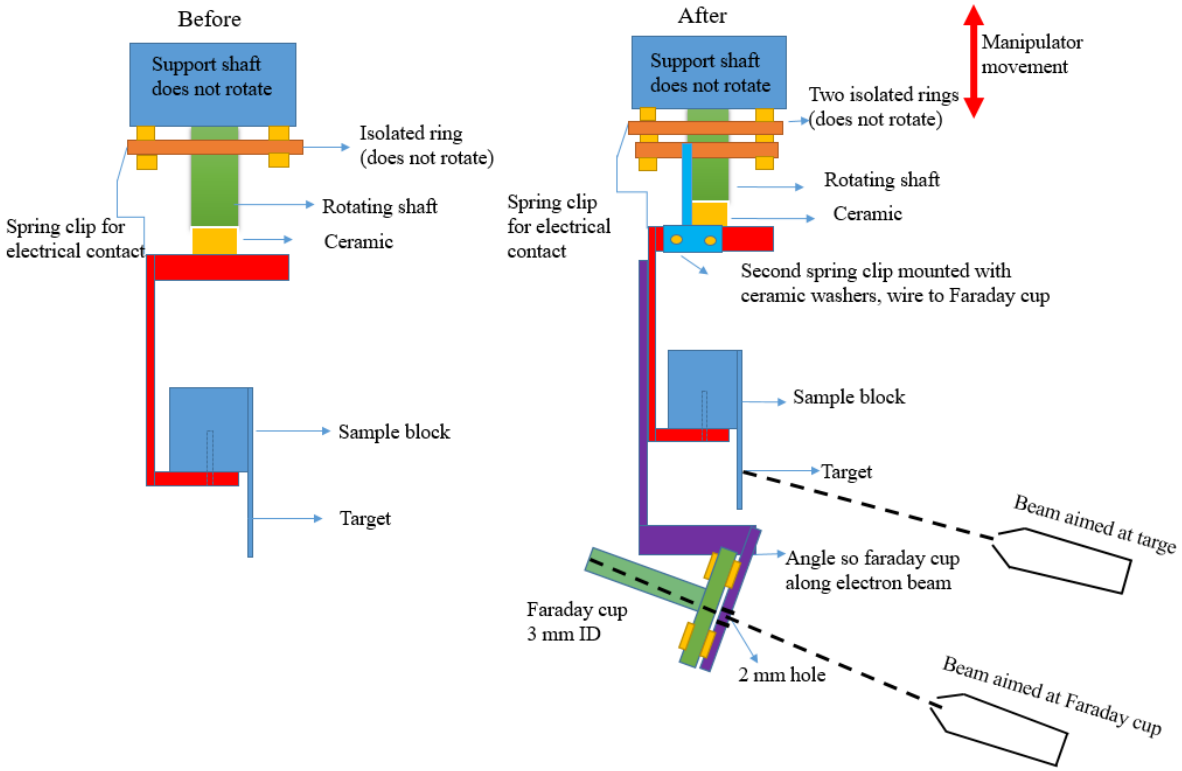

Figure 3.6: Schematic diagram of the Faraday cup after it was added to an ultra-high vacuum manipulator.

SIMION simulations for energies larger than the PE: SIMION is a software package used to calculate electric fields and to simulate the trajectories of charged particles in those fields. Electron trajectories calculated by a SIMION simulation are shown in Figure 3.3. The blue lines in Figure 3.4 show the electrostatic field. The reader is referred to [121] for more details of the software package.

In this approach the SIMION electron optics simulations range from 600 eV to 4000 eV in order to compare the results with the results observed by Gergely et al. [120]. In the simulations, 2.4 million electrons were simulated to enter the super-CMA starting within ± 2 mm from the axis and at an angle between 12° and 28°. The pass energy was set to 100 eV. Potentials of the electrode were set according to Table 3.2. The transmitted electrons were counted to estimate the transmission function. Complementing these simulations, the transmission curve determined by Gergely et al. [120] was digitised and compared with the SIMION simulations as shown in Figure 3.7. It is observed that a curve proportional to $1/E$, where E is the energy of electron, lies in between the two transmission curves. Note that in the actual spectrometer a small residual magnetic field is present (due mainly to the Earth's

magnetic field) but no magnetic field was applied in the SIMION simulation and this may result in the transmission curve to be over-estimated as shown in Figure 3.7. More discussion regarding spectrometer efficiency will be presented later in this section.

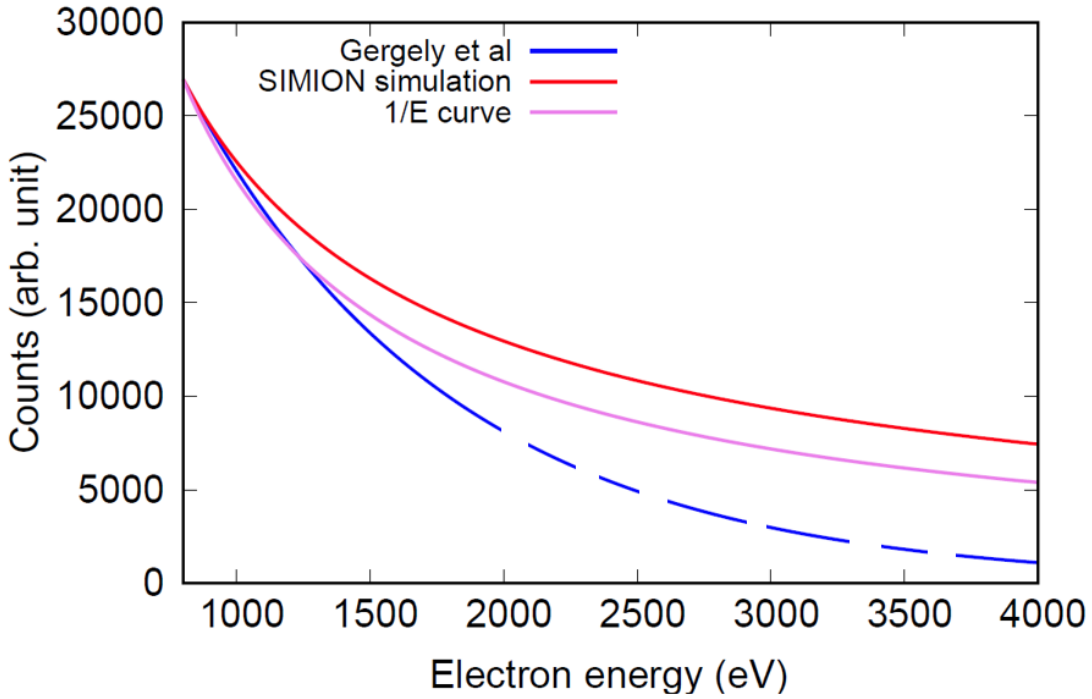

Figure 3.7: Transmission functions of the CMA as estimated from the SIMION electron optics simulations (red curve) and experiment work by Gergely et al. [120] (blue curve). The $1/E$ function (violet curve) lies in between the two estimated transmission functions. Note that the data of Gergely et al. was provided up to 2000 eV only. The dashed blue curve extends the data of Gergely et al. beyond 2000 eV via extrapolation based upon the best fit of the data.

SIMION simulations for the energies lower than the PE: In this case the situation changes completely. The transmission of the analyser suddenly drops quickly (this drop off is also seen by Gergely et al. [120] although no information was given in relation to the PE). The transmission of the analyser was simulated at two different PEs as shown in Figure 3.8A. Looking at Figure 3.8B, which shows the pure secondary electrons emission from the silver sample (measured for three different PEs), it can be seen, that indeed if it had been measured with a different PE, the shape changes in a way consistent with the SIMION simulation. Note that this measurement was done after the Helmholtz coils were installed (Figure 3.12 shows the Helmholtz coils surrounding the Auger experiment).

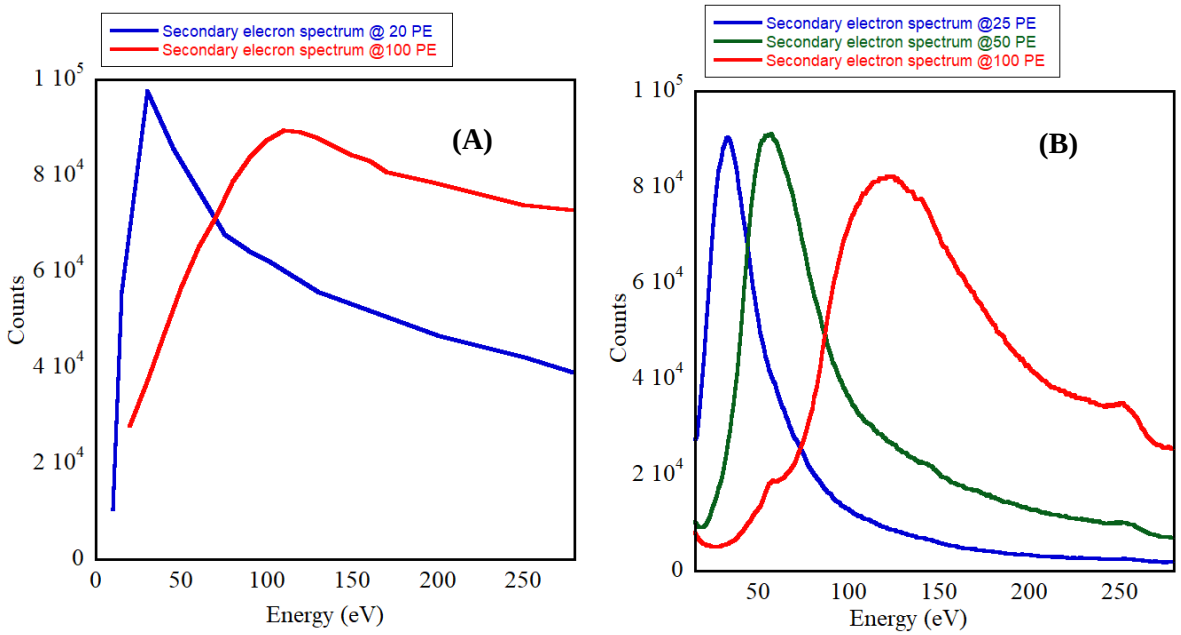

Figure 3.8: Figure (A) shows the transmission function $T(E)$ as simulated by SIMION. Figure (B) shows the pure secondary electron emission from (Ag) sample at three different PEs.

Comparing elastic peak intensities with the SIMION simulation: The efficiency of the spectrometer was also measured experimentally by measuring the elastic peak intensity of the incoming electron energy from 350 eV to 3500 eV. In this case, the electron gun is used to direct electrons at a silicon target and then the number of electrons that are reflected from the silicon target is measured. In a simple V-shape model for the electron trajectories, the number of reflected electrons is proportional to two factors: a) the probability of scattering over the angle between the electron gun and the spectrometer, which in our case is on average 123° , i.e. the elastic differential cross-section and b) the mean distance traveled into the material without losing energy, i.e. the corresponding inelastic mean free path λ(E). Note that if the electron makes an inelastic excitation, it will drop to a lower energy level and hence it will not contribute to the elastic peak and thus the elastic peak intensity depends on the mean distance traveled without losing energy.

Both quantities have completely different energy dependencies. The λ(E) increases with energy, as shown in Figure 3.9, while the elastic cross section decreases with the energy as shown in Figure 3.10.

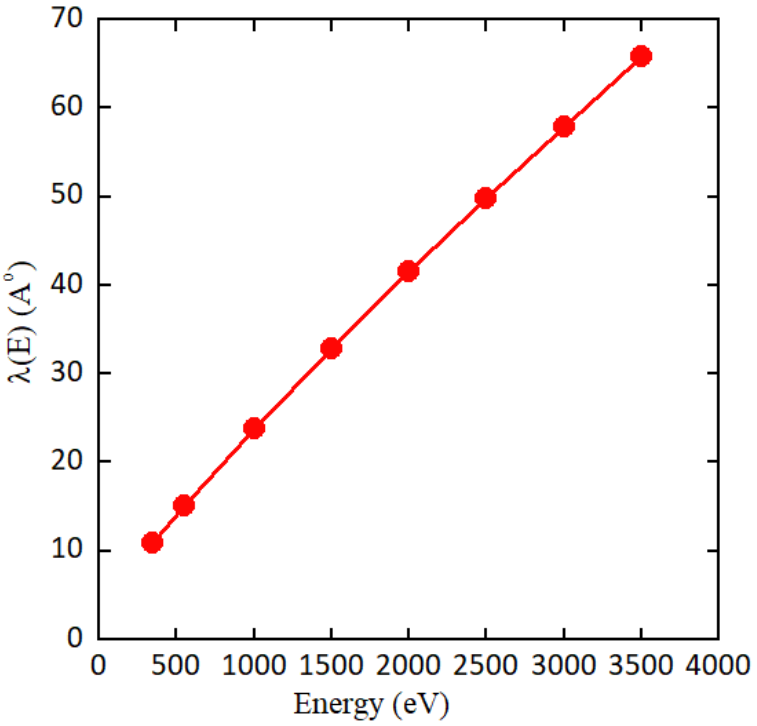

Figure 3.9: Calculated inelastic mean free path $\lambda(E)$ for a silicon sample at different kinetic energy using QUASES-IMFP-TPP2M software [122].

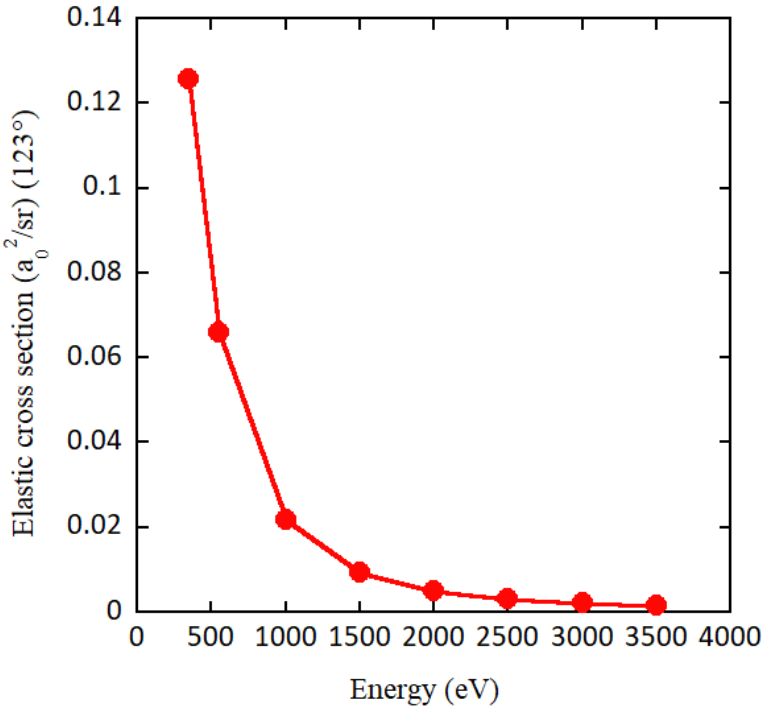

Figure 3.10: Calculated cross section at 123° scattering angle (Note: this angle corresponds to the electrons detector in our geometry) for a silicon sample at different kinetic energies obtained from the NIST electron elastic-scattering cross-section database [123].

By comparing the measured intensity (at the same beam current) with the product of these two quantities one can obtain an estimate of the transmission of the super-CMA.

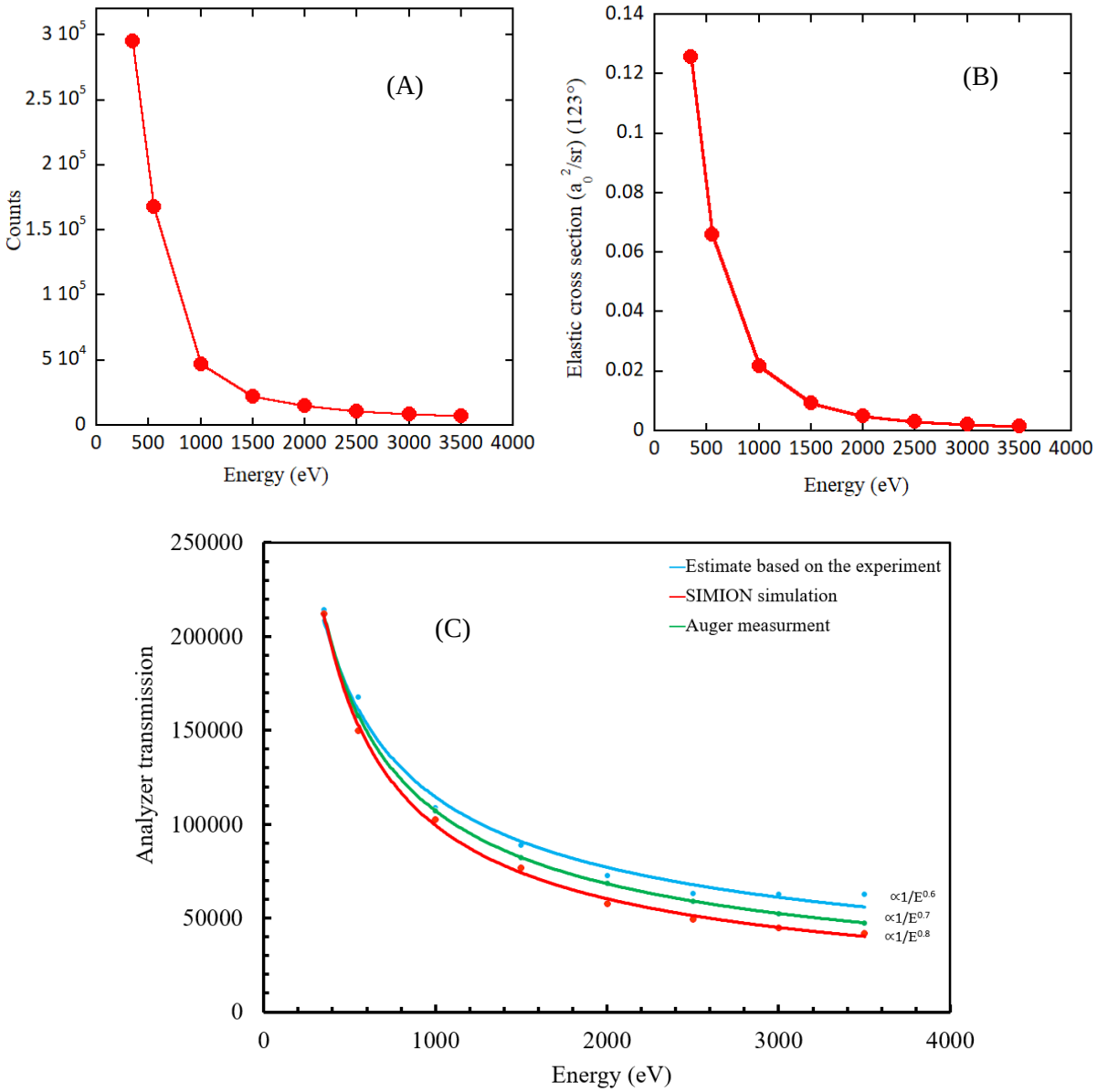

Figure 3.11: Figure (A) represents the measured count rate per nanoampere (nA). Figure (B) represents the product of cross section (a_0^2/sr) * $\lambda(E)$ (Å) versus energy which would be proportional to the expected count rate if the analyser transmission would be energy-independent. Figure (C) shows the experimental estimate of the super-CMA transition (blue dots) compared with the transmission functions of the CMA as estimated from the SIMION electron optics simulations (red dots) as well as with Auger measurement (green dots, will be discussed later). The solid blue, green and red lines are the fits of the estimate experimental, Auger measurement and SIMION simulation data, respectively. Note that in Figure (C) the red and the green curves were scaled to the highest point of the blue curve.

The initial measurement (before the Helmholtz coils were installed) showed the obvious discrepancy between SIMION simulation and the measured transition based on the elastic peak, particularly at the low energy end of the spectrum. To improve this it was decided to implement Helmholtz coils surrounding the apparatus to nullify the effect of Earth's magnetic field as shown in Figure 3.12. After the addition of the coils, and with suitable currents flowing in each Helmholtz coil, efficiency measurements were repeated and found to scale like $1/E^{0.6}$, with E being the electron energy, as shown in Figure 3.11C (blue curve). Spectrometer efficiency was also calculated using a SIMION simulation with the same settings [Pass energy = 100 eV and energy range from 350 eV to 3500 eV] and this data was in close agreement (proportional to $1/E^{0.8}$) with the elastic peak intensities approach, see Figure 3.11C (red line).

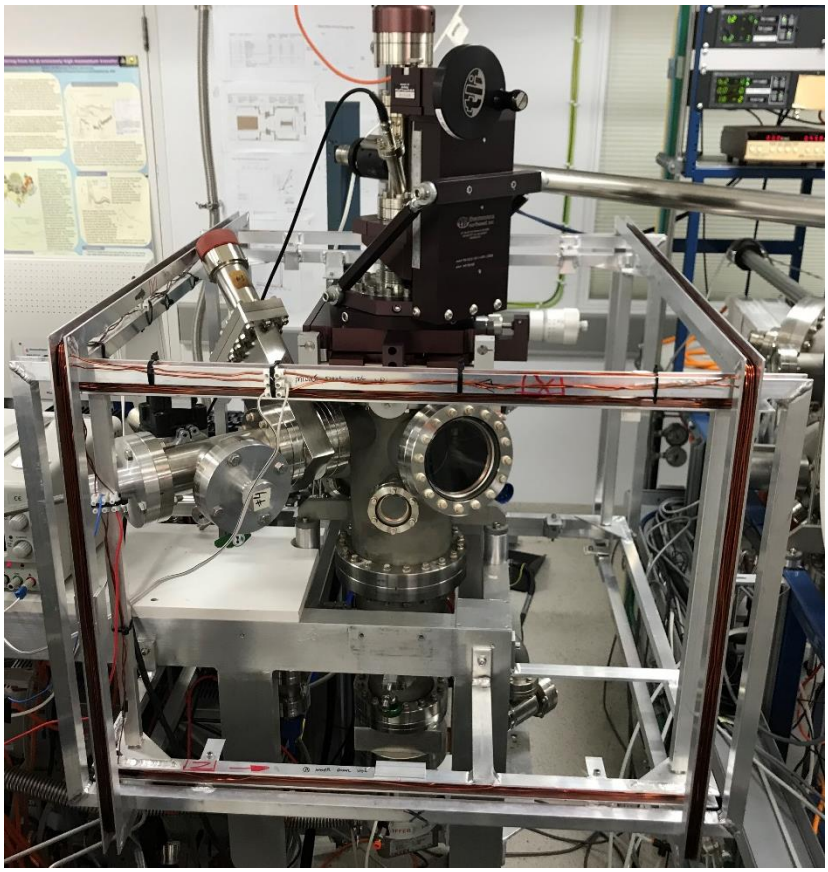

Figure 3.12: Helmholtz coils surrounding the Auger experiment.

Comparison of Auger signal intensities at different energies for silver and silicon samples:

As a third method to determine the transmission of the super-CMA analyser beside the SIMION simulation and elastic peak methods, an attempt was made to use the (electron-beam induced) Auger signal itself. For the Auger signal, a good theoretical estimation of the intensity can be obtained by taking the product of the ionization cross section (σ_x) at the energy of the electron gun, the fraction of the core holes that decay by a specific Auger channel, and the λ(E) at that energy. Elements with two Auger lines at widely different energies were selected. These were silicon (Si) and silver (Ag). A sample of each was prepared by etching the surface in an Argon environment until contaminates were removed. The intensity ratios of the two Auger peaks for these samples were then measured. The expected ratio of the intensities of these two lines were calculated. Thus, the difference in these ratios should give the ratio of the analyser transmission T(E) at these energies. The details are discussed below.

When a specimen is excited by an incident electron beam used in Auger production the important thing to know is how many core holes are made. In the silver (Ag) measurement, there are L_3-core holes created at high binding energy (2558 eV) and M_4-core holes created at low binding energy (344 eV), and the ionisation cross sections of these levels differ greatly.

The Auger intensity is determined by measuring: a) the probability that the incoming electron creates a core hole in the specific atomic subshell and that is the σ_x and b) the fraction of these core holes that decays via the observed Auger channel. The probability of these transitions (P_{LMM} and P_{MNN}) and the $\sigma_{L,M}$ for silver Auger using a NIST database program [123] were calculated. The fluorescence decay by the Auger channel rather than the X-ray channel was also corrected using the equation below, however the effect was minor.

$$a_{Auger} = 1 - \omega_{x-ray} \tag{3.1}$$

c) The λ(E) which is defined as the average distance an electron travels between two inelastic interactions. This was calculated from QUASES-IMFP-TPP2M Ver. 3.0 [122]. By using these factors, the number of those Auger electrons that are leaving the sample was calculated. Thus providing an expected count rate. The resulting relationship can be represented as:

$$I_{Auger}^{emit} = \sigma\ P\ \lambda\ \mathrm{I}_0 \tag{3.2}$$

With I_0 the beam current. Comparing the count rate of the two calculated lines gives (if I_0 is the same for both measurements):

$$\frac{I_{E_1}^{emit}}{I_{E_2}^{emit}} = \frac{\sigma_1 \, P_1 \, \lambda_{E_1}}{\sigma_2 \, P_2 \, \lambda_{E_2}}. \tag{3.3}$$

Moreover, the intensity of Auger electrons as measured by the analyser was determined. The Auger signal is on a background of secondary electrons. The areas of the Auger peaks were determined by a background subtraction procedure using the Origin program [124]. In this method, a straight line background was subtracted from the measured spectrum. This straight line background requires the selection of two points in order to determine the area of the peak. One at the low energy (high background) side E_{Low}, and the other at the high energy (lower background) side E_{High}. These points are labelled in Figure 3.13 and Figure 3.14.

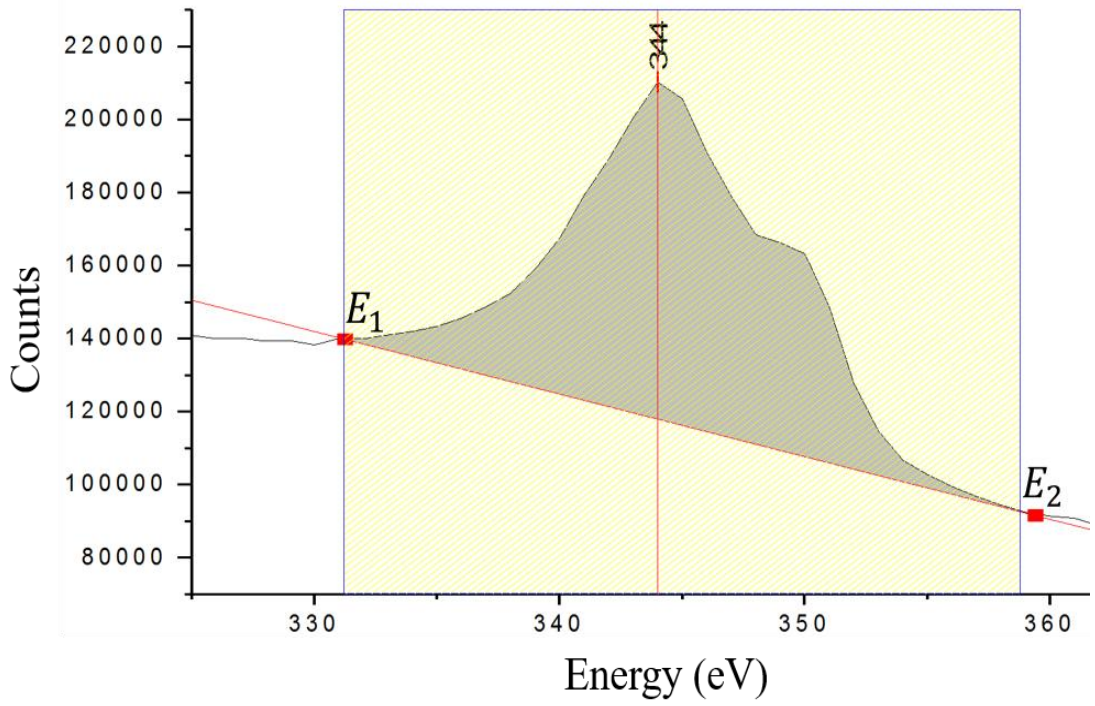

Figure 3.13: Spectrum of the $M_4N_{4,5}N_{4,5}$ and $M_5N_{4,5}N_{4,5}$ transitions for Ag.

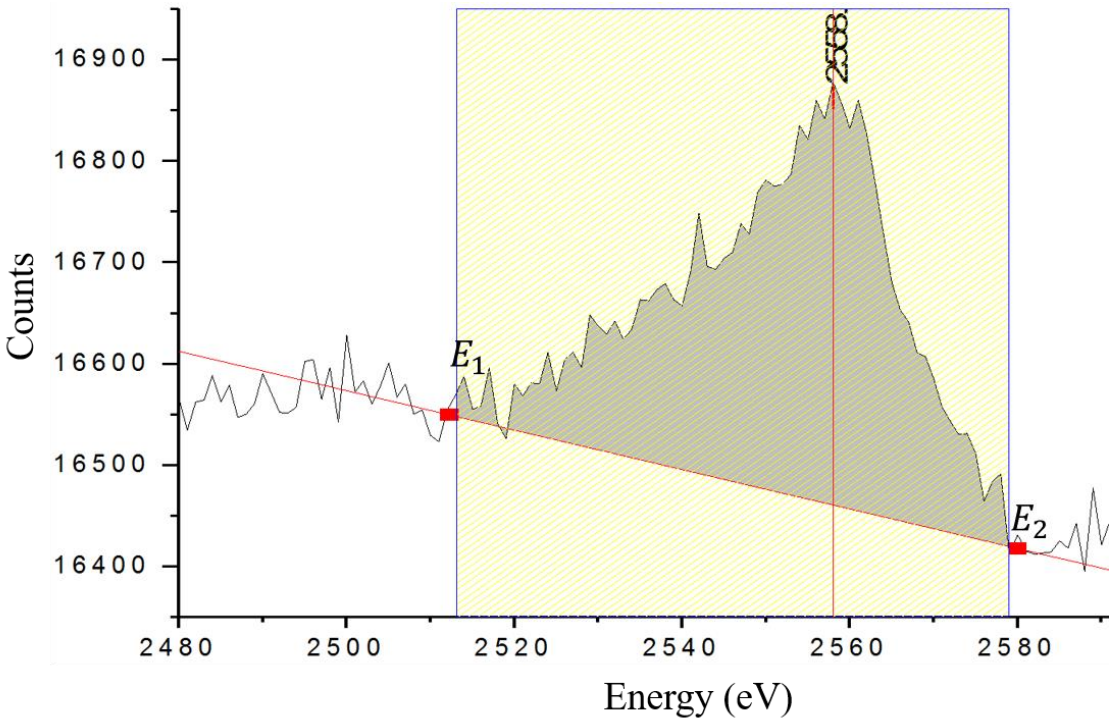

Figure 3.14: Spectrum of the $L_3M_{4,5}M_{4,5}$ transitions of Ag.

The observed count rate of one Auger line is written as:

$$I_{Auger}^{measured} = \mathrm{C}\ \mathrm{T(E)}\sigma\ P\ \lambda\ \mathrm{I_0} \tag{3.4}$$

Here, C is the experimental geometry which does not depend on the energy of the detected electron and $\mathrm{T(E)}$ is the analyser transmission.

The ratio of the count rate of the two measured lines is given by:

$$\frac{\mathrm{I}_{\mathrm{E}_1}^{measured}}{\mathrm{I}_{\mathrm{E}_2}^{measured}} = \frac{\mathrm{C}\ \mathrm{T}(\mathrm{E}_1)\sigma_1\ P_1\ \lambda_{E_1}}{\mathrm{C}\ \mathrm{T}(\mathrm{E}_2)\sigma_2\ P_2\ \lambda_{E_2}} \tag{3.5}$$

Rearranging, the ratio of the analyser transmission is:

$$\frac{\mathrm{T}(\mathrm{E}_1)}{\mathrm{T}(\mathrm{E}_2)} = \frac{\mathrm{I}_{\mathrm{E}_1}^{measured}\sigma_2\ P_2\ \lambda_{E_2}}{\mathrm{I}_{\mathrm{E}_2}^{measured}\ \sigma_1\ P_1\ \lambda_{E_1}} \tag{3.6}$$

and thus the energy dependence of the analyser transmission $\mathrm{T(E)}$ can be determined.

The result of this method for Ag suggests that the analyser transmission is proportional to $\approx {}^{1}/_{E^{0.7}}$ (see Figure 3.12, green line).

In summary, the intensity for Auger silver MNN and LMM peaks was measured. The MNN was 173412 counts while the LMM was 2060 counts. These measured intensity rate was found to be 84.The theoretical ratio assuming no energy dependence of the detection, was found to be 23. From this one conclude that the energy dependence of the analyser is 3.6 obtained by dividing the measured intensity ratio over the theoretical intensity ratio. The energy Auger lines differs by factor 7.4. Hence, if a $1/E^{X}$ dependence is assumed, then these observations would indicates that X is 0.7.

This approach proved hard to apply for the silicon sample due to the presence of secondary electrons. Electrons from the incoming beam, used to create the core holes, transfer their energy to many target electrons. These electrons are located in the conduction band and have generally a small amount of the energy, but enough to escape into the vacuum. Typically they carry energies below 50 eV. This kind of electrons is known as a "secondary electron". In contrast, the electrons that are located in the inner shell, need a sufficient transfer energy to overcome this strong bonding. Therefore, this process causes an atomic ionization, which then leads to the emission of X-ray or Auger electrons, another kind of secondary electron. Figure 3.15 shows the entire electron emission for the silicon sample including secondary electrons. The Auger peak itself is visible near 80 eV, but its intensity is small and the background due to secondary electrons has a complicated shape. Hence it is not possible to determine the area of the Auger peak with good accuracy.

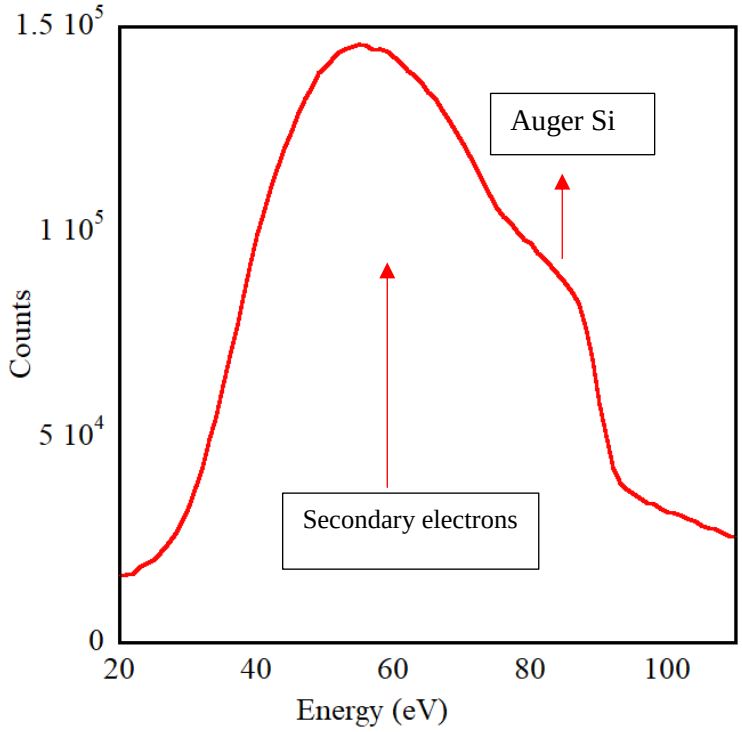

Figure 3.15: Secondary electron effect on the measurement of Auger Si measured at a pass energy of 100 eV. It is hard to separate the area of the Si Auger peak from the secondary electrons.

3.3.2 Advantages and limitations of the super-CMA

One advantage of our type of super-CMA is the geometry and symmetry of the design, which is selected to be cylindrical in order to maintain the maximum possible sensitivity. Electrons emitted from the source are introduced directly into the front space between the inner (1) and outer (2) cylinders after passing through a circular grid inserted in the front of the spectrometer (see Figure 3.3). This manner of inserting the electron into the spectrometer makes the working distance larger between the source and the spectrometer. This working distance can be up to 55 millimetres. Another advantage of the spectrometer geometry is that it allows the introduction of a tantalum shield of 30 mm diameter inside the second stage of the analyser to prevent X-rays or low energy gamma rays emitted from the ^{125}I source from being counted by the detector, such that the Auger electrons can be detected without background. Moreover, the simple construction of the spectrometer allows easy disassembly and cleaning of all parts of the analyser. This is important, particularly after contamination with iodine as occurred in an early measurement. The most serious limitations of the super-CMA are (i) that the precise

energy position of an observed peak is sensitive to the sample position relative to the analyser, and (ii) the complicated transmission function.

3.3.3 Super-CMA energy scale calibration

The energy scale of the spectrometer was calibrated using an electron gun to excite Auger electrons for various samples: Ag, Ta, Cu, Nb, and Si. The results were then compared with the literature. The output showed that the ΔE, (ΔE is the difference between the Auger peak found in the literature and our experiment), was about 5 eV for energies below about 500 eV. The difference was attributed to the work function. The current research measured the kinetic energy outside the material, whereas the results in the literature are relative to the Fermi level. For energies over 1000 eV the difference was larger and this was attributable to both work function and power supply calibration. Table 3.3 shows results for the calibration compared to the literature results.

Table 3.3: Auger peak energies from our experiment versus Auger peak emerges from the literature.

Sources	Peak reported in the literature (eV)	Peak observed from our experiment (eV)	ΔE (eV)
Silver (Ag)	351.6	347	4.9
Tantalum (Ta)	168	163	5
	1674	1666	8
Copper (Cu)	918.20	912	6.20
Niobium (Nb)	1937.10	1930	7.10
Silicon (Si)	1616	1608	8
	92.90	88	4.9

3.4 Channel electron multiplier detector

A Sjuts Optotechnik KBL 25RS Channel Electron Multiplier (CEM) [125] was used in this study to detect the Auger electrons emitted from ^{125}I. It consists of a hollow glass tube, the inside surface of which is coated with a thin film of semiconducting material. This material acts as the secondary electron emitting dynode surface. The detected electron impinges on this surface, creating secondary electrons that are accelerated by the applied field. When these electrons again strike a surface this process repeats and an avalanche of up to 10^8 electrons is produced which generates a pulse that is suitable for further amplification by a conventional electronic circuit (see Figure 3.16).

Figure 3.16: A Sjuts Optotechnik KBL 25RS channel electron multiplier detector.

A positive potential of 200 eV relative to ground is established using a Zener diode at the entrance to the CEM, see Figure 3.3, such that even very low-energy electrons transmitted through the analyser will have at least 200 eV kinetic energy when they impact the channeltron walls, and hence can easily produce secondary electrons. It was found necessary to maintain a relative potential of 2.15 keV on the tube anode since at such a voltage the count rate was found to be stable and reproducable (see Figure 3.17).

All secondary electrons are collected at the anode of the CEM, from where they pass into the amplifier, as shown in Figure 3.3. An integral discriminator with a threshold set just above the noise level, is used to generate a TTL pulse for each electron detected [125] which is used as input for a counter, interfaced with the computer. The software program used in this experiment

is called DAC Auger program. It can control the experiment using two Measurements Computing units, one is a counter, and the other one is a DAC which controls the main high-voltage power supply of the super-CMA.

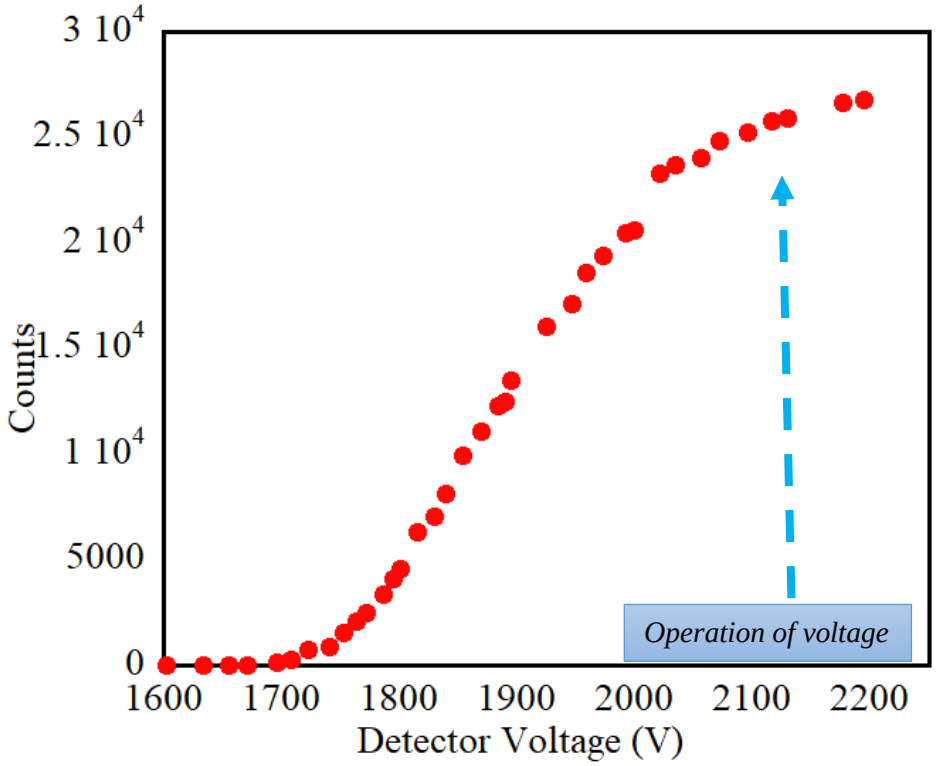

Figure 3.17: Count rate of the channel electron versus applied voltage.

3.5 The vacuum system

The vacuum system in use is an ultrahigh –vacuum chamber with a base pressure of ≈5x10^{-10} Torr, equipped with the super-CMA spectrometer for use in Auger electron measurements. Such a low pressure is necessary to allow the electron to be detected (by avoiding scattering of the electrons by residual gases between the sample surface and the detector) and to make sure that the prepared, atomically clean surfaces can be maintained free of contaminants during the measurement. This is particularly important for the electron-beam based measurement used to calibrate the spectrometer, as described in section 3.3.3. The initial vacuum is generated by a roughing pump which is used to evacuate the chamber, thereby producing an initial rough vacuum. This is also used to pump a backing line for the next stage, the turbo-molecular pump. The roughing pump is connected to the turbomolecular pump via an angle valve. Finally, the turbomolecular pump is connected to the main chamber and is used as a second stage to achieve UHV. The UHV regime can only be reached after baking out the chamber for about 48 hours at temperatures between 100-150 ˚C. This procedure facilitates the elimination of residual molecules adsorbed onto the stainless steel walls of the chamber, which otherwise would be released at a low rate thereby increasing the pressure and possibly contributing to source contamination. The pumping speed of the turbomolecular pump fitted to the vacuum system is 210 L/S.

3.6 Electron momentum spectrometer (EMS)

3.6.1 Design and principle of EMS spectrometer

The second spectrometer, EMS, was a locally-built spectrometer that can detect electrons with energies from 2 keV to 40 keV. A schematic layout of the spectrometer is shown in Figure 3.18.

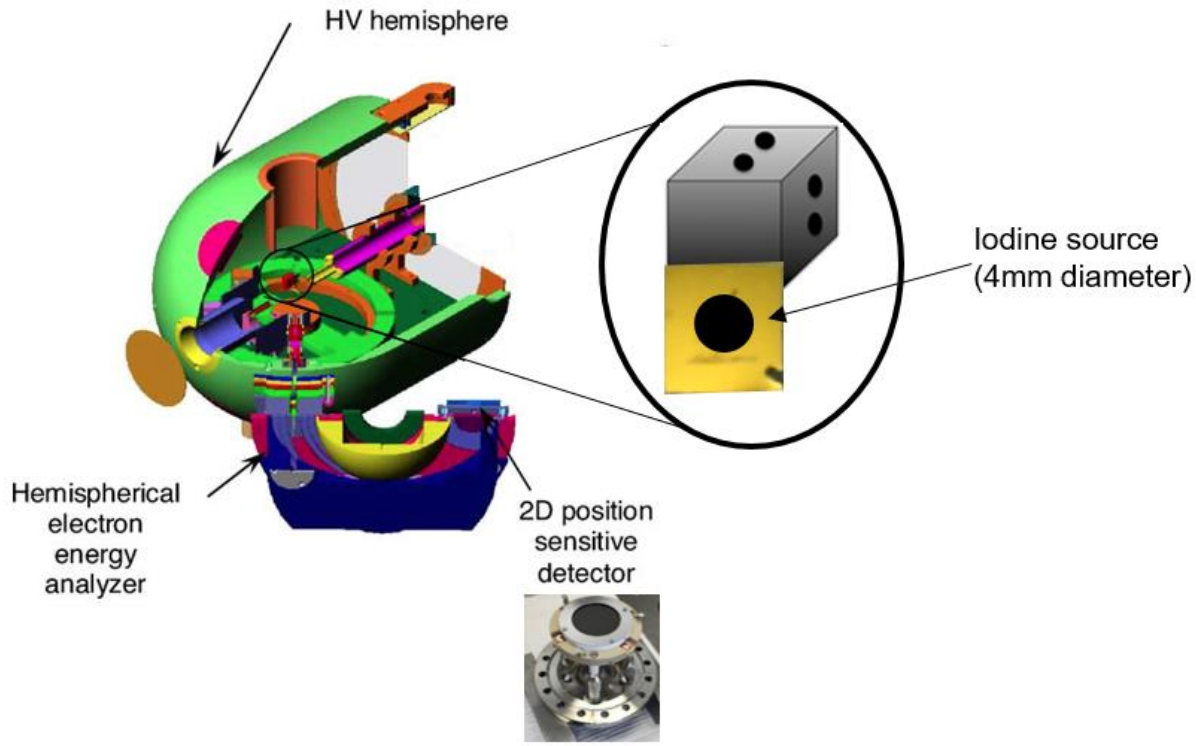

Figure 3.18: Schematic of electron momentum spectroscopy (EMS) (image extracted from [126]). The details are described in the main text.

The iodine source was held on the mounting block and was moved into the main spectrometer chamber and located in the centre of the high voltage (HV) hemisphere at positive high voltage in a vacuum chamber. The ejected electrons leaving the source initially find themselves surrounded by a high voltage hemisphere. After leaving this, via a 0.5 mm wide slit, the electrons are decelerated and focused by an electrostatic lens stack. A set of small circular apertures used to calibrate the angular scale of the detector is mounted on a turntable. Placing these in front of the analyser allows calibration of the angular scale without breaking the vacuum [127]. An electrostatic field is applied to the emitted electrons from the source, to decelerate them to the pass energy of the hemispherical electron energy analyser. These

electrons are then detected by a two-dimensional detector, which is capable of measuring a range of energies simultaneously [127].

The high-energy spectrometer works rather differently compared to the super-CMA. The hemispherical electron energy analyzer (HEEA) is a component attached to the main chamber (see Figure 3.18) and acts as a narrow pass filter which focuses electrons with a particular energy, as determined by a potential difference established between the outer and inner hemispheres.

The analysis/detection process is divided into three stages: focus, energy filtering, and finally detection by a two-dimensional position sensitive detector. The primary purpose of the first stage is to collect the electrons from the source and focus them onto the input plane of the analyser, in the process reducing the electron kinetic energy. In the second stage of the analysis/detection process, the electrons with certain energies must be discriminated. This process is easily performed geometrically using the hemispherical analyser with a suitable potential applied to the inner and outer hemispheres. All electrons enter the HEEA at the same radius, but at the exit plane their radius depends on their kinetic energy. In the final stage, electrons hit the multichannel plate pair of diameter 40 mm. At the multichannel plates, the single incoming electron produces an avalanche of the order of a million electrons, which can be detected striking a phosphor screen, mounted behind the channel plates. A camera is used to determine the exact exit position, from which the precise electron energy and propagation direction can be calculated [126, 128]. For this application the propagation direction is not important.

SIMION simulation: An example of SIMION simulations for the lens stack is shown in Figure 3.19. In these simulations the initial kinetic energy of the electron was 30 keV, and at the exit of the lens stack this energy was reduced to 1000 eV, the pass energy of the analyser. The lens stack forms an image of the source at the entrance of the hemispherical analyser. The simulations were done for a 0.2 mm diameter source (as is the case when an electron beam hits the sample) and a 4 mm diameter source (as is the case for our ^{125}I sample) with initial angular range of 1.5°. In both cases, all electrons transmitted through the slit will enter the analyser, but the width of the image formed is much smaller for the electron beam case. The spectrometer transmission is thus determined solely by the width of the entrance slit and is independent of energy. The hemispherical detector transfers this image (with unity magnification) onto the

channel plates. When a radioactive source is used the larger spot size at the entrance of the hemisphere causes some deterioration in energy resolution. As the energy of the electrons after deceleration is always the same, the detection efficiency of the channel plates does not depend on the initial electron kinetic energy.

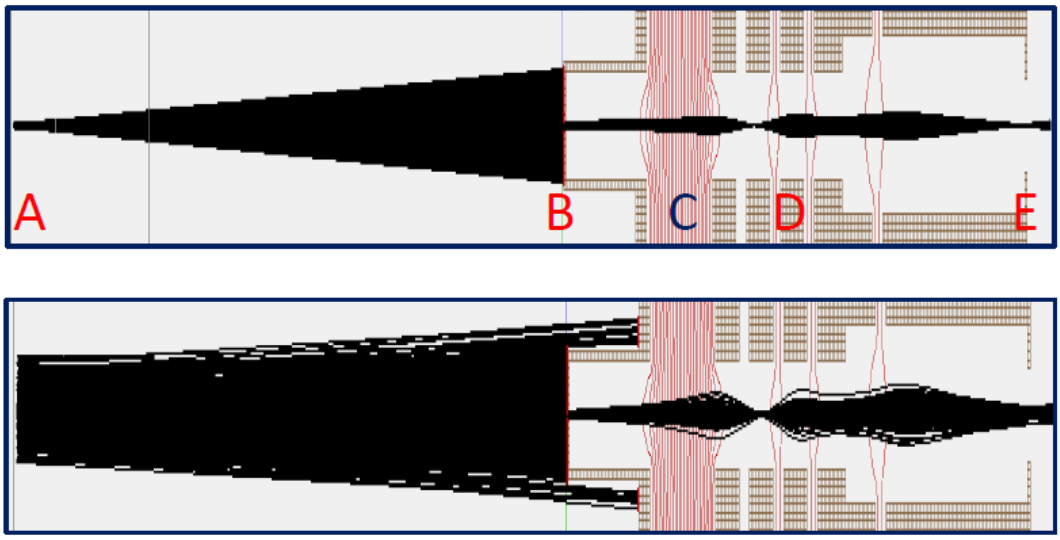

Figure 3.19: Example of a SIMION simulation for the high-energy spectrometer. Electrons emitted from the source (A) are restricted from entering the lens stack by a 0.5 mm wide slit (B). After the main deceleration stage (C) the electrons are focused by a set of electrostatic lenses (D) on the exit plane (E) that coincides with the entrance of the hemispherical analyser. The vertical scale is expanded by a factor of 4, for clarity. The top panel shows the case of a 0.2 mm diameter source (as is the case when an electron beam hits the sample). The lower panel shows the case for a source size of 4 mm diameter as is the case for our ^{125}I source. The red lines are equipotential planes plotted at 1000 V intervals.

The spot size at the entrance to the hemisphere will be smaller than the sample size due to demagnification by the electron optics and will be effectively $\frac{1}{2}$ mm full width at half maximum. This also causes a spot size at the channel plate of $\frac{1}{2}$ mm. At a pass energy of 1000 eV, the energy range measured by the entire (40 mm diameter) detector, is 200 eV. That means that 1 mm corresponds to $\frac{200}{40}$ = 5 eV. Thus $\frac{1}{2}$ mm correspond to 2.5 eV, which is approximately the experimentally observed resolution (2.3 eV).

3.6.2 Iodine measurement by EMS spectrometer

The EMS spectrometer was operated in two different modes for measuring ^{125}I. One is the high-resolution mode, which can be achieved by setting the kinetic energy of the decelerated electrons (pass energy) at 200 eV, while applying a constant high voltage to the hemisphere, and varying the analyser voltage up to 1 keV. Stability of the sample high-voltage was checked using a precision voltage divider (Ross Engineering VD45) and a 7-digit voltmeter, and it was found to be better than 0.2 V. (However the absolute accuracy of the high-voltage measurement is not expected to be better than 5 V.) The energy resolution was ≈ 2 eV (as will be discussed in section 4.2) in this mode but the range of energies that can be measured was limited to ≈ 930 eV due to constraints on the voltage that can be applied to the analyser [127].

In the low-resolution mode, the main 40 kV power supply was controlled by a computer using a 16-bit DAC. Measurement of the obtained voltage showed deviations of up to 8 V from the actual requested setting when the high voltage was varied between 5 and 35 kV (using a simple linear calibration), but when the voltage is varied over a smaller range (1-2 kV) then the deviation was fairly constant (≈ 1 V) over this range. In this mode the pass energy was set at 1000 eV. The energy resolution obtained in this way was 6.6 eV, but the energy range that can be measured is not restricted and the data acquisition rate is about 5 times higher. If no peaks are expected over a particular energy range, then that energy range was skipped, further speeding up the measurement. Besides the main high-voltage, one of the lens voltages was changed under computer control to ensure that the decelerating lens stack forms an image of the source at the entrance plane of the analyser at all times [127].

Figure 3.20 shows an overview of the electronics used in the EMS spectrometer. Typical voltages used on the high voltage hemisphere as well as the electron optics are given in Table 3.4.

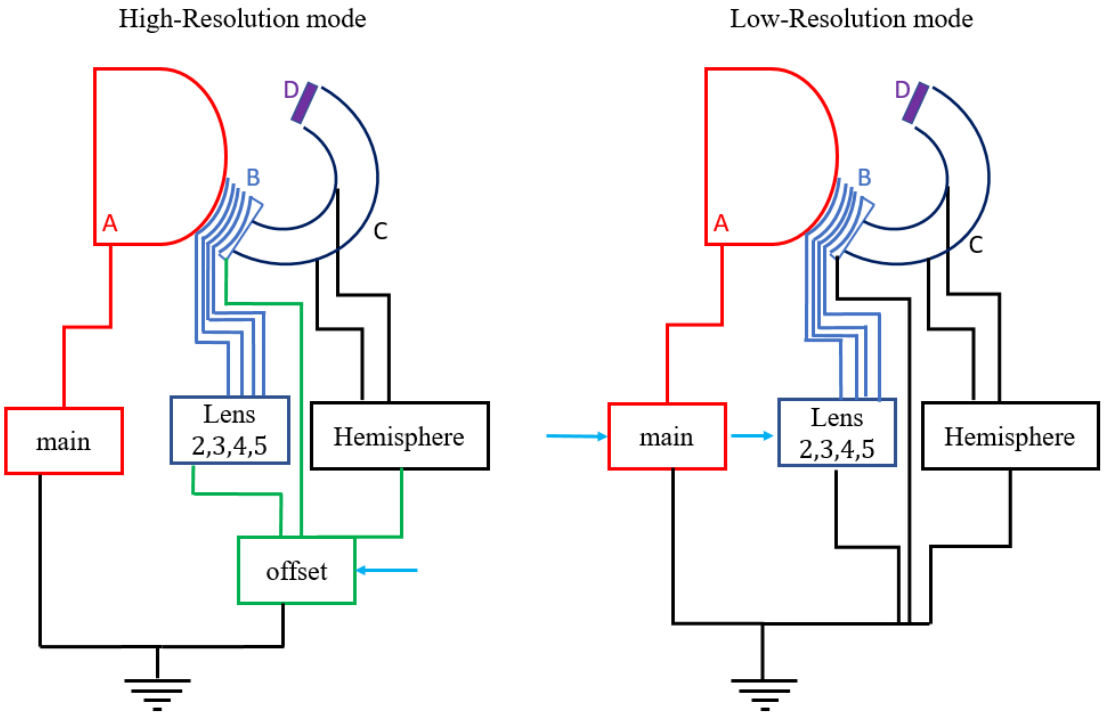

Figure 3.20: A schematic view of the EMS spectrometer electronics in the high-resolution (left) and low-resolution (right) mode. A, B, C and D represent the HV sphere, lenses, hemisphere and detector respectively. Arrows indicate power supplies that are controlled by the computer.

Table 3.4: Voltages values used for high and low resolution modes.

	High resolution mode	Low resolution mode
Main HV	30.547 kV	29.3 – 33.7 kV
lens 2	3.75 kV	2.05 – 2.36 kV
lens 3 and 5	0.45 kV	1.9 kV
lens 4	0 V	0 V
pass energy	200 eV	1000 eV
Inner Hemisphere	133.33V	666.6V
Outer Hemisphere	-80V	– 400 V
Offset	120 – 543 eV	

3.7 Summary

In summary, two types of electron spectrometer were used in this research in order to measure Auger electron spectra. One is the super-CMA which can measure electrons in the energy range from 50 eV to 4 keV. Hence, this instrument is capable of measuring the L-Auger electrons together with the K-conversion line generated from the electron capture (EC) decay of ^{125}I. In addition, the MNN Auger electrons (< 600 eV) were also measured using this spectrometer. The results of these measurements will be presented in chapter 6. The second spectrometer is the EMS spectrometer which can measure electrons from 2.87 keV to 40 keV. Thus, with this instrument, the L, M, N conversion lines and KLL, LMM Auger groups can be measured as will be shown in chapter 4, 5 and 6.

Chapter 4

Conversion electron spectroscopy and discussion

In this chapter first the conversion line group measurements (L, M and N) from electron capture decay of ^{125}I using the EMS spectrometer is discussed. This is followed by an analysis of nuclear parameters extracted from the experimental results. The nuclear parameters will be used later when the conversion electron intensities are used to calibrate the Auger intensity. Moreover, the analysis of the L line shape, as described here, will provide a good starting point for the fitting of the more complicated Auger spectra.

4.1 L-shell Conversion electron spectroscopy

Two measurements on the L-conversion lines were achieved with the EMS spectrometer. One was measured in the high energy-resolution mode for the L_1-conversion line only, and the other was measured in the low energy-resolution mode for the L_1, L_2 and L_3 conversion lines (see section 3.6.2 for more details about high and low-resolution modes). Note that in the high-resolution mode, the width of the L_1 line is slightly narrower than that obtained in the low-resolution mode. When measurement of an extended energy range is required (L_1, L_2 and L_3), the low-energy resolution mode is selected because measurement in the high-resolution mode takes a long time (about 5 days), in particular for the L_3 line which is a very weak signal.

4.2 High resolution L_1 conversion measurement

In Figure 4.1, a spectrum of the L_1-conversion line in the high-resolution mode is shown. A well-defined peak with a clear tail was observed at an energy (maximum peak at 30.543 keV) that is consistent with the expected value for the L_1-conversion line (30.553 keV). The peak was fitted to the Voigt line shape. The obtained fit parameters are reproduced in Table 4.1. In the fitting, the Lorentzian width represents the life time broadening of the L_1 (as described in chapter 2, section 2.3). The natural widths were taken from the literature (2.2 eV) [129]. The Gaussian width of the main peak was allowed to be a free parameter and was interpreted as the energy resolution of the spectrometer in this mode of operation. Hence it was concluded that the energy resolution of the spectrometer is ≈ 2.3 eV FWHM (full width at half maximum). This is larger than the energy resolution obtained in REELS (Reflection Electron Energy Loss Spectroscopy) experiments with the same spectrometer at 30 keV and 200 eV pass energy where the obtained resolution is 0.5 eV FWHM [126]. The poorer energy resolution is due to the larger size of the emitting surface (4 mm for this experiment, compared to 0.2 mm of the electron beam in REELS) and the fact that ripple and drift in the main high-voltage power supply cancels out in REELS (incoming electrons are accelerated, outgoing electrons are decelerated) but not in the current experiment. Note that in all subsequent plots the experimental data is shown as the black points and the fit is shown in the red lines.

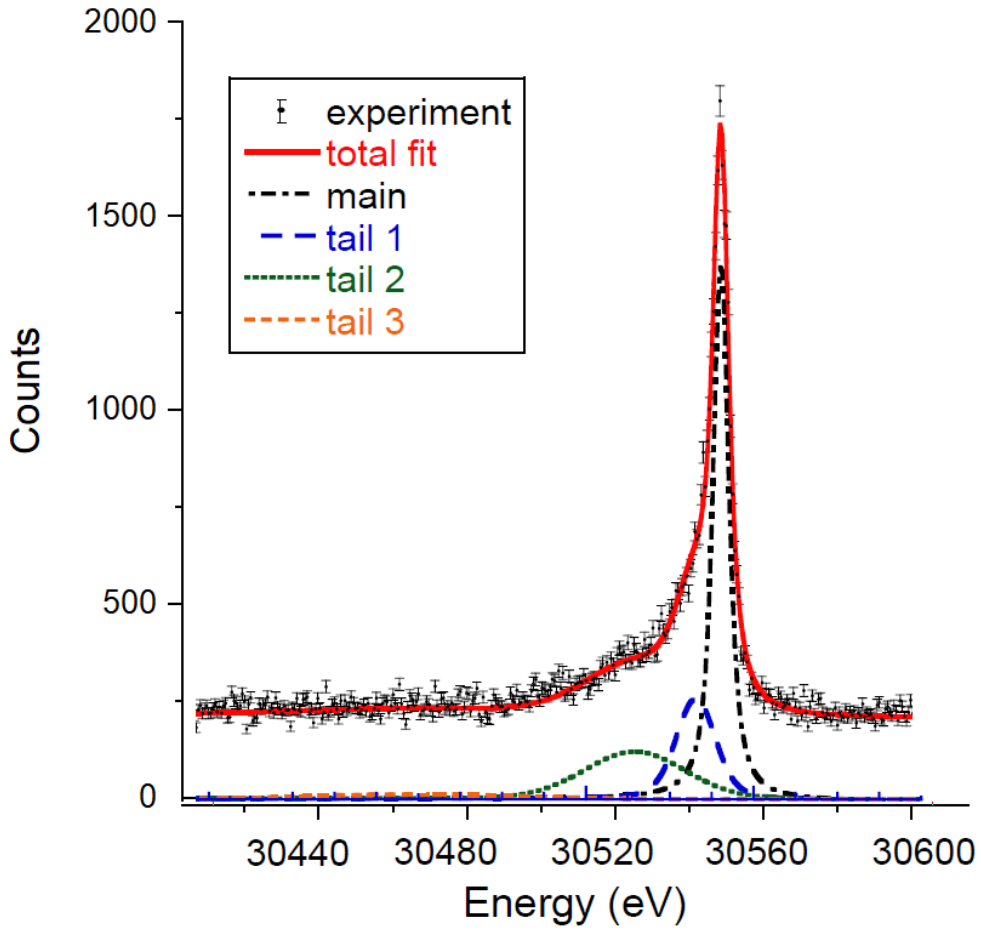

Figure 4.1: The L_1-conversion line measured at high resolution mode compared with fitted curves obtained as described in the text.

Using the parameters of Table 4.1, one would conclude that the sum of the areas of the tail contributions is almost equal to that of the main component. There is significant overlap of the tail components and the main component and other fitting approaches could produce a rather different area of the tail component. In comparison, the intrinsic intensity for high-energy photoemission of carbon was found to be 58% of the main peak [130], whereas Yubero and Tougaard [131] obtained a value of ≈ 60% for the intrinsic intensity in photo emission of the aluminium (Al $2s$ level). The tails can be seen as an indication that "shake-off" occurs frequently. In the context of medical physics, these "shake-off" electrons are important as they are a moderate source of additional low-energy electrons with large genotoxic effects [12]. Note that all components shown in Table 4.1 were additionally broadened by an estimate of the experimental resolution (≈ 2.3 eV) and the calculated lifetime broadening of the L_1 level (Lorentzian of 2.2 eV FWHM [129]).

Table 4.1: Parameters used to fit the spectrum of Figure 4.1 and the Gaussian width of the different components. All components were additionally broadened by an estimate of the experimental resolution (≈ 2.3 eV) and the calculated lifetime broadening of the L_1 level (Lorentzian of 2.2 eV FWHM).

	Position (shift) (eV)	Rel. intensity	Width (eV)
Main	30552	1	0
Tail 1	(-6.0)	0.37	8.7
Tail 2	(-20)	0.47	27.7
Tail 3	(-73)	0.10	55

4.2.1 An evaluation of the line shape

It was observed that all measured conversion line peaks and Auger peaks have asymmetric shapes with clear tails on the low energy side. The generally accepted explanation for these tails is that they can be attributed to the energy loss as a result of intrinsic and extrinsic effects. Intrinsic effects involve interaction with the local environment in the source (i.e. the decaying atom) such as shake-up and shake-off processes. In contrast, extrinsic effects involve the transportation of electrons through the solid from the emitter to the surface. This may cause inelastic scattering leading to the creation of (surface) plasmons [81, 115]. In this experiment, a third of monolayer of iodine was placed directly onto a gold substrate. Therefore, the tail contributions, at high energies (e.g. L_1-conversion line energy), due to extrinsic effects (surface plasmon excitation) should be very small of the order of 3% [132]. Thus, one would expect that the intrinsic effects, in particular the shake-off processes, are the main cause of the tails. All measured spectra were fitted with the Origin program [124].

4.2.2 Intensity ratios and energy determination

The fitting approaches were first applied to the conversion lines since this is a simpler case than the Auger lines because the Auger peaks are overlapping. It was subsequently assumed that the same line shape applies to the Auger lines when measured to the same resolution, taking into account the differences in the lifetime broadening.

The conversion electron spectra were used to gain an understanding of the spectrometer performance and the shake effect in the sample after core electron emission. This knowledge was then used to aid the interpretation of the Auger spectra.

Several fitting strategies were employed but all resulted in very similar conclusions to the one described here. The observed main peak can be described with a Voigt line shape which is the convolution of a Gaussian and a Lorentzian. As discussed in section 4.2, the Gaussian width represents the resolution of the spectrometer, and the Lorentzian width represents the lifetime broadening of the associated transition level(s) [115]. The lifetime broadening was taken from the literature (in the Auger case sum of three lifetimes: the initial state and the lifetime of the final states (i.e. both levels)) [129, 133]. The tail components of the peak were described by some linear combination of symmetric Gaussian line shapes, as they seem to fit the tails reasonably well. In short, each measured peak was described by the summation of two (or three) symmetrical Gaussians and a Voigt line shape. A small increase in the background due to the intrinsic loss at the low energy side of the peak, was observed in all measured spectra. To take this into account a Shirley background approach [134] was applied for all measured spectra. The same tail parameters were used to describe all peaks, but the lifetime broadening of the different levels was taken from their literature estimates.

4.3 Low resolution L_1, L_2 and L_3 conversion measurement

In order to measure the L_1, L_2 and L_3-CEs in a single measurement, the spectrometer was operated in the low-energy resolution mode. The measured L_1, L_2 and L_3 conversion line spectrum is shown in Figure 4.2. Three conversion lines were easily identified from the spectrum and it should be noted that the measured L_2 and L_3 lines were much weaker than the L_1 line. All lines were fitted with the same set of tail parameters, but their lifetime broadening was taken from the literature [129] and differed slightly (from 2.2 to 2.84 eV). Therefore, this approach assumes that all L-conversion lines have the same shake energy distribution. As the shape of the tails due to shake-off is poorly understood, the validity of this assumption is still

to be confirmed. If this assumption is abandoned without prior knowledge of the shake distribution for the L_2 and L_3 lines, peak areas (and hence the obtained area ratios) could vary substantially due to low peak to background ratios for the L_2 and L_3 lines.

The experimental data (energies and intensities) were compared with the BrIcc predictions and measurements by Brabec et al. [116], Casey et al. [48] and Miura [135]. Note that there is no intensity ratio for L-conversion lines given by Miura et al. for comparison. The comparison results are shown in Table 4.1, section 4.6.

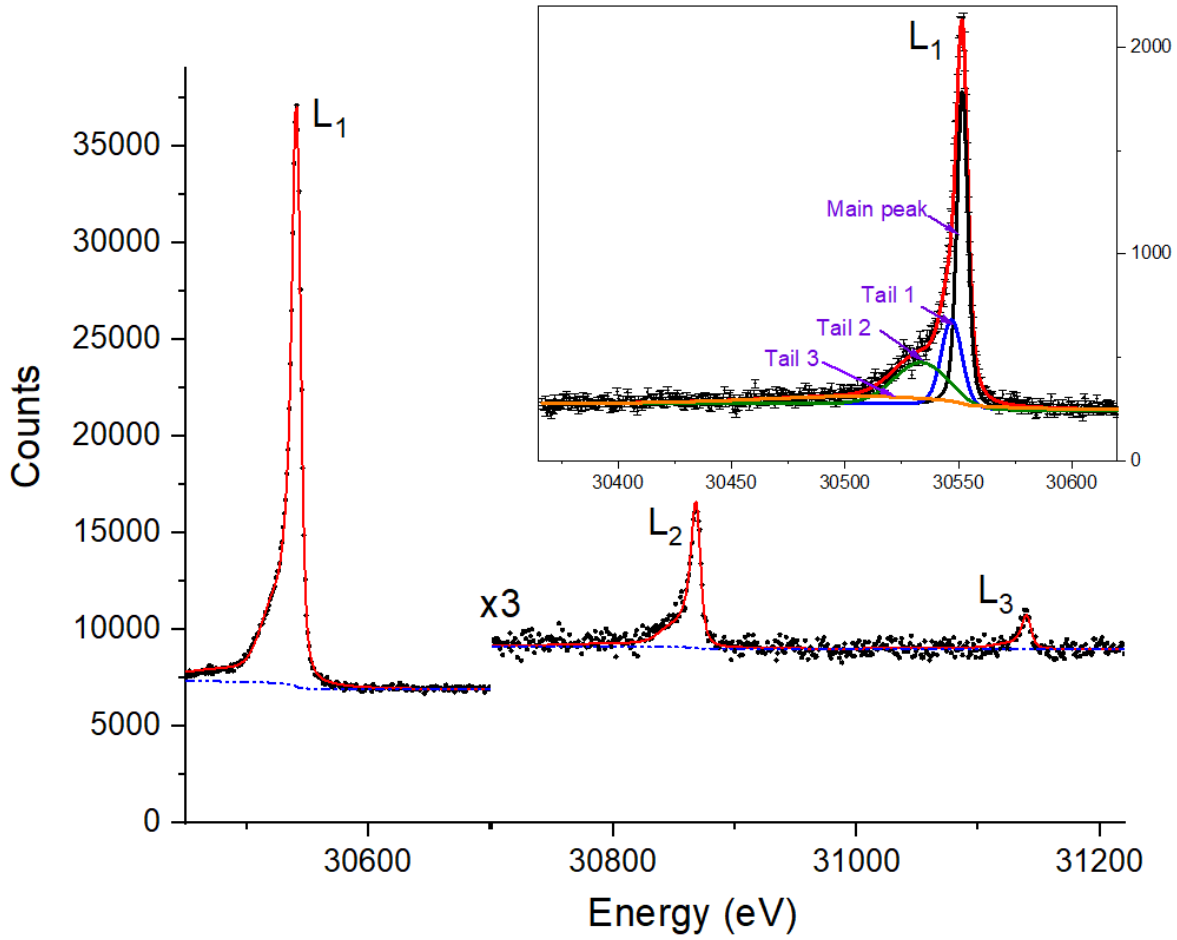

Figure 4.2: The L_1, L_2 and L_3 conversion line spectrum, which is taken at 6.6 eV instrumental resolution. The L_1 measured (upper panel) at high resolution is also shown indicating the components fitted to the line shape. Natural widths of the L_1, L_2 and L_3 lines are 2.2 eV, 2.84 eV and 2.62 eV, respectively, as adopted from the literature [129].

The measured energies for the L_1, L_2 and L_3 lines are 30543 (10) eV, 30871(10) eV and 31140 (10) eV, respectively. In comparison to the predicted BrIcc energies of 30553 eV, 30881 eV and 31151 eV respectively, the discrepancy is within 10 eV. This result is reasonable since the measured voltage of the spectrometer in low resolution mode could be out by up to 8 V (which corresponds to 8 eV of electron energy) as discussed in chapter 3, section 3.6.2. The measured peak separation of the conversion lines is, however, within 1 eV of that calculated. The L subshell intensity ratios as determined from the fit are L_1: L_2 : L_3 = 1: 0.083 (3): 0.019 (5). Similar measurements were conducted by Brabec et al. [116] and Casey et al. [48] with different spectrometers. They measured the L subshells intensity ratios to be 1: 0.095 (2): 0.023(5) and 1: 0.11(2): 0.041(2), respectively. Thus, the measured relative intensities of the L_2 and L_3 lines in the present work seem to be lower than those reported before [48, 116].

Present measurements have a much better resolution than the measurements performed by Brabec et al. and Casey et al. as illustrated in Figure 4.3. Hence, the shake contributions in their measured spectra would have been buried by this effect. Moreover, the sources used in their experiments were relatively thick (order of μm), which results in a more pronounced tail at the low-energy side, due to the energy loss of electrons as they travel through the material. Thus, the present measurements provide better quality data to qualify the tail of the line shape and hence the magnitude of shake effects.

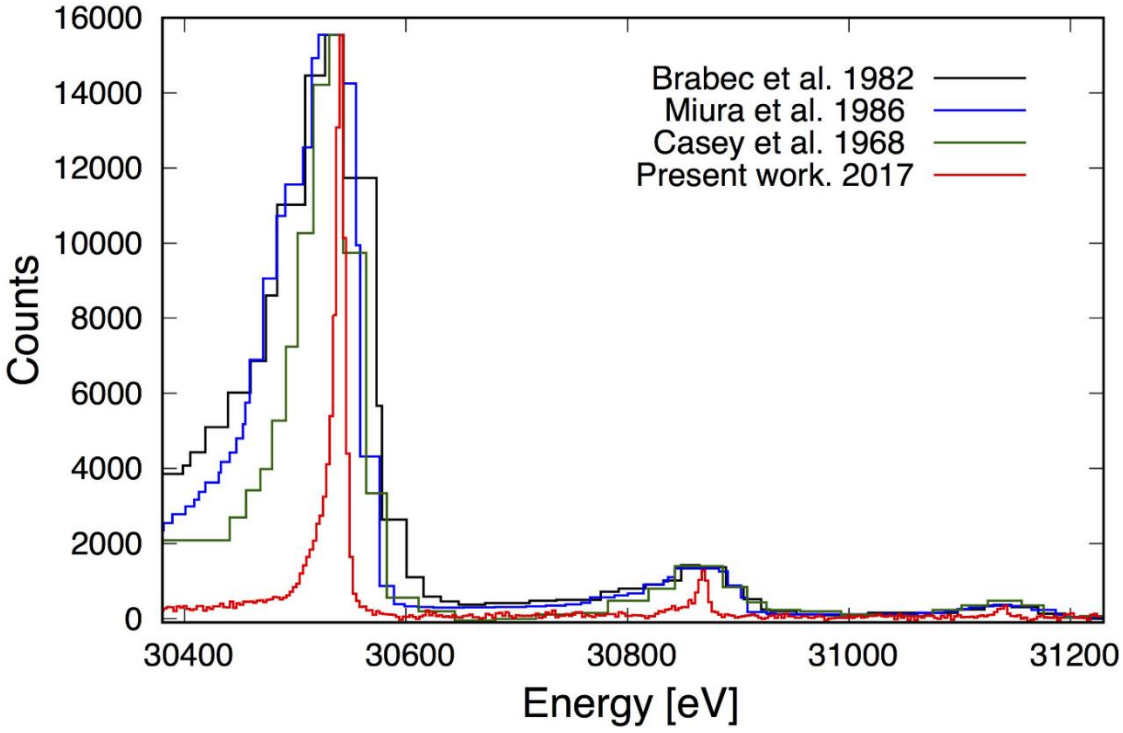

Figure 4.3: The L-conversion measured in the present work and measurements by Brabec et al. [116] (black curve), Miura et al. [135] (blue curve), Casey et al. [48] (dark green curve). All literature data were digitised and scaled to match the L_1 peak height of the present data. The energy resolution of the present measurement is significantly better than the previous measurements.

4.4 L, M and N conversion lines spectrum

As the M_1 conversion line is almost 4 keV apart from the L_1conversion line, a 3 keV energy region in between the peaks was skipped in the measurement to reduce data acquisition time as shown in Figure 4.4. The M, N and O conversion lines spectrum was acquired in a separate measurement. However, only the M_1, M_2, M_3 and N_1 lines were strong enough to be observed, as shown in Figure 4.5 and Figure 4.6. This was due to the signals of the all other lines being too weak relative to the background. The natural widths of these conversion lines were adopted from [129].

The measured intensity ratio L_1: M_1 = 1: 0.21 (1) is in very good agreement with the predicated BrIcc value of 1: 0.20. This ratio does not depend on the nuclear parameters (see Table 4.3). Hence it confirms our assumption that the efficiency of the spectrometer is energy-independent. The measured energies of the M_1, M_2 and M_3 lines were 34473 (10) eV, 34609(10) eV and 34660(10) eV, respectively, while the predicted BrIcc values for these are 34486 eV, 34622

eV and 34673 eV, respectively. Again, a good agreement is found between the measured and predicted energies.

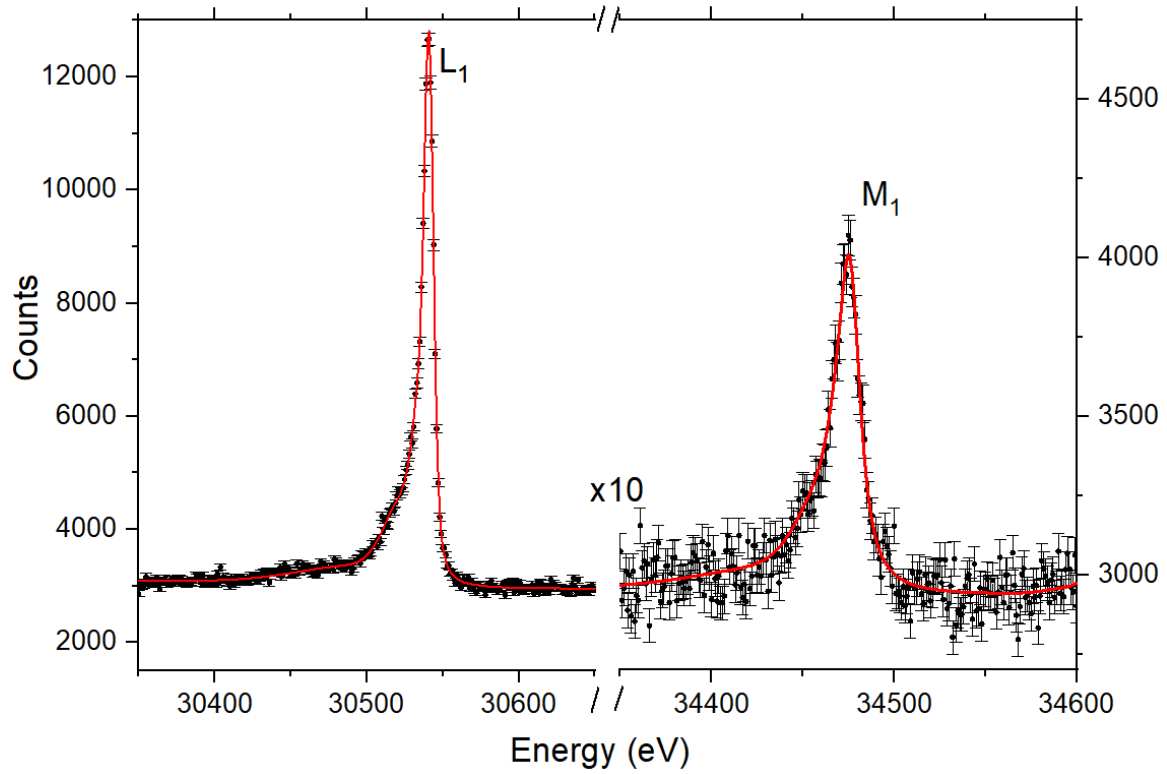

Figure 4.4: The L_1 and M_1 conversion line spectrum. A 3 keV energy region was skipped to reduce the measurement time. Natural widths of the L_1 and M_1 lines are 2.2 eV and 10.2 eV, respectively [129] and indeed the observed M_1 peak is much broader than the L_1 peak.

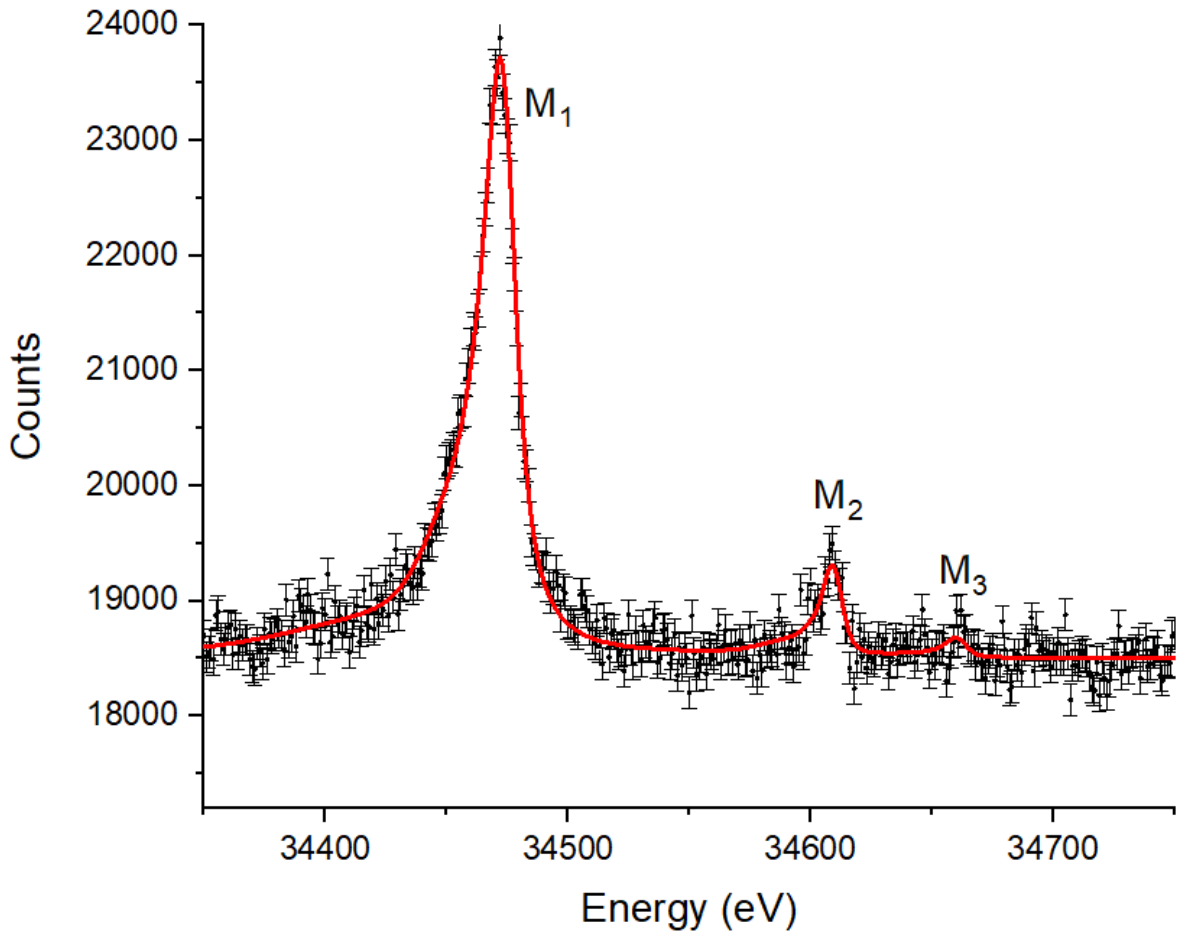

Figure 4.5: The M_1, M_2 and M_3 conversion line spectrum. Natural widths of the M_1, M_2 and M_3 are 10.2 eV, 3.2 eV and 3.9 eV, respectively [129].

The measured intensity ratios were M_1:M_2:M_3= 1:0.099(6):0.029(7). Ratios of 1: 0.100(5): 0.030(5) were reported by Brabec et al. [116]. Both measurements are consistent with each other, but it should be noted that the signal of the M_2 and M_3 lines were weak, so there is a large uncertainty in them. Finally, the M_1 conversion line was measured together with the N_1 conversion line as shown in Figure 4.6. The measured intensity ratio of M_1 and N_1 was found to be 1:0.20 (3), while 1:0.21(1) was reported by Brabec et al. [116]. Both measured ratios are consistent with the predicated BrIcc value of 1:0.20. It is apparent from Figure 4.5 that the M_3 conversion line was largely buried under the background due to low statistics in this measurement.

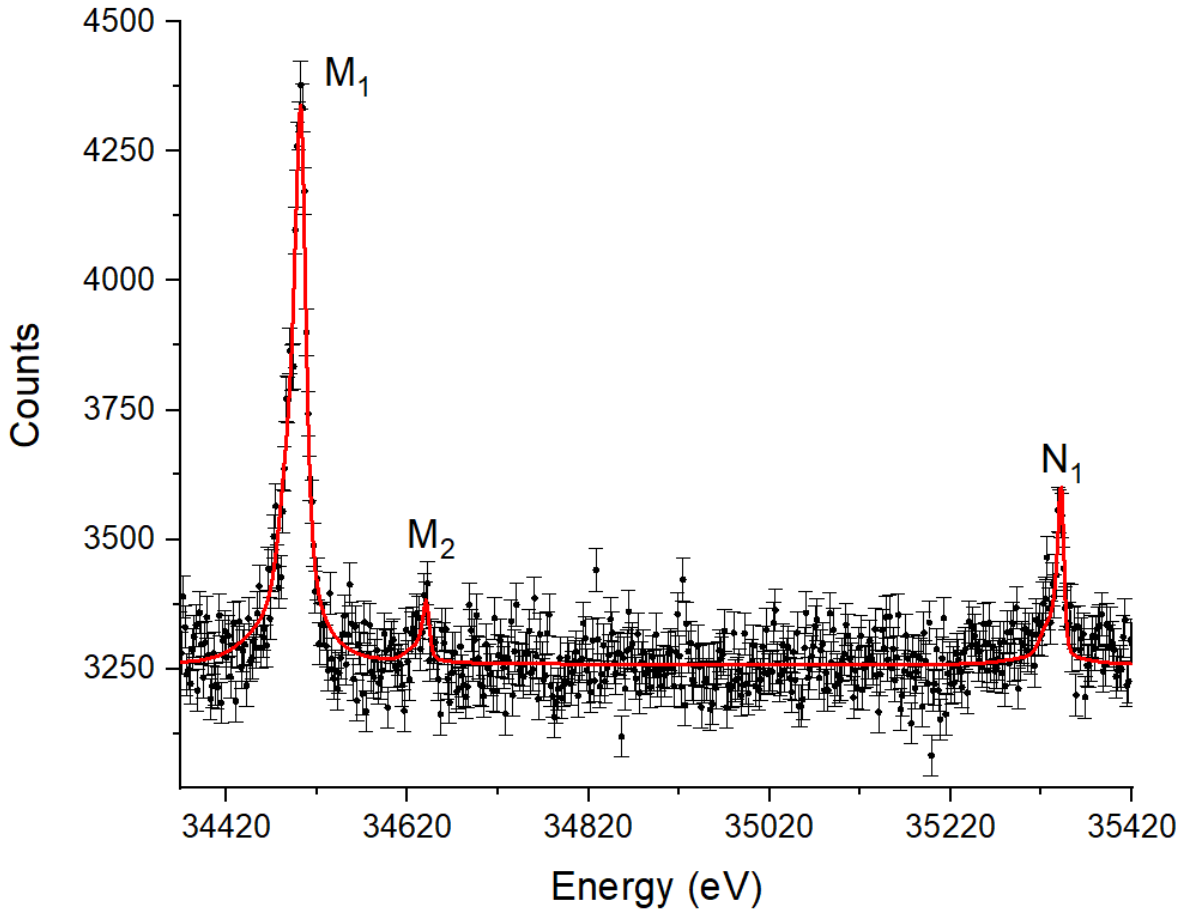

Figure 4.6: The M_1, M_2 and N_1 conversion line spectrum. Natural widths of the M_1, M_2 and N_1 lines are 10.2 eV, 3.2 eV and 2.4 eV, respectively [129].

4.5 Nuclear parameters analysis

The least squares fitting method was used to extract the nuclear parameters, λ and Δ from the intensity ratio of the different conversion lines using the program Minuit [136]. The extracted nuclear parameters, as determined from our measurements of the intensity of the various conversion lines, are:

$$\lambda = 2.0 \pm 2.0 \tag{4.1}$$

$$\Delta = 0.0000^{+0.0001}_{-0.0000}$$

Note that Δ is related to the mixing ratio δ by equation 2.23. The experimental results suggest a zero mixing ratio δ, which implies that the multipolarity of the 35 keV transition in ^{125}Te is purely $M1$. For consistency, the mixing ratio of $\delta = 0.0$, as obtained from this analysis, was adopted in the later Auger spectra analysis. An example of how the nuclear parameters could have an effect on the conversion line intensity ratio is shown in Figure 4.7. On the other hand, the obtained penetration parameter, λ = 2.0(20), agrees broadly with the Brabec et al. [116] value of λ = 2.4(14). However, due to the current limitations of the BrIccEmis program, the penetration effect was not included in the calculations for $\delta = 0.0$ Auger spectra. Therefore, the analysis presented in the next chapter adopts a mixing ratio of $\delta = 0.0$ and no penetration effect is included. Note that the nuclear parameters (λ and δ) may change a little. However, small values of nuclear parameters (e.g. λ = 0.029 and δ = 0.015) consistent with our measurement would not change the major calculation of this work significantly.

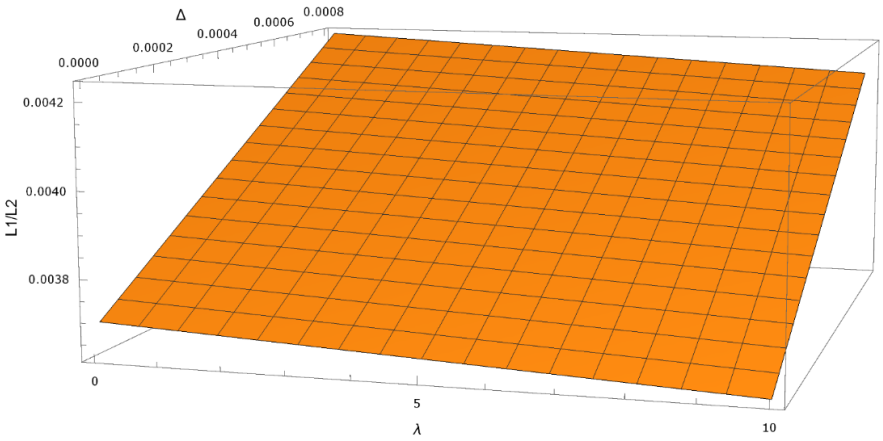

Figure 4.7: Illustration of how the parameters λ and Δ influence the intensity ratio of the conversion lines. As one can see from the figure when the Δ increases the L_1/L_2 ratio increases. In contrast, when the λ increases the L_1/L_2 ratio decreases.

Acknowledgment

I would like to thank Mr Bryan Tee for providing me the values of λ and δ.

4.6 Summary

Important conclusions drawn from the conversion electron spectra measurements include: a) All measured line shapes are asymmetric and about half of the intensity is not in the main component but in the tail at the low energy side of the peak. It was also found that, after the effect of different lifetimes is taken into account, it is possible to describe all conversion lines with the same line shape. b) The second important finding was that the mixing ratio δ was determined from the intensity ratios. This mixing ratio of δ was found to be ≈ 0.00. This implies that the multipolarity of the 35 keV transition in ^{125}Te is purely $M1$, from this one can calculate that the fraction of the decay of the metastable state of ^{125}Te that goes by gamma-ray emission should be close to 0.074 [137]. As a result, the number of the conversion electrons that appear per nuclear decay are known ($P_{CE} = 0.93$), and hence this number can be used to derive the number of Auger electrons per nuclear decay by studying the CE to Auger intensity ratio.

A summary of the BrIcc and the previous measurement results are presented along with our measurements in Table 4.2 and Table 4.3. For comparison purpose, the calculated conversion intensity ratios from BrIcc accommodate two different mixing ratios and lambdas ($\delta = 0.00$ and $\lambda = 2$) and ($\delta = 0.03$ and $\lambda = 0$). It is obvious from the Table 4.3, that the present measurements suggest nuclear parameters of ($\delta = 0.00$ and $\lambda = 2$), in contrast to the measurements by Brabec et al., which suggest nuclear parameters of ($\delta = 0.03$ and $\lambda = 2.4$).

Table 4.2: Experimental results of the measured energies as obtained from the conversion line measurements. These results are compared with the BrIcc.

Atomic shell	Energy (eV)	
	Experiment	Ref. [108]
L_1	30543 (10)	30553
L_2	30871(10)	30881
L_3	31140(10)	31151
M_1	34473 (10)	34486
M_2	34609(10)	34622
M_3	34660(10)	34673
N_1	35323(10)	35324

Table 4.3: Results of the measured intensity ratios as obtained from the conversion line measurements. These results are compared with the literature and BrIcc.

Atomic shell	Experiment			BrIcc	
	Present work	Brabec et at. [116]	Casey et al. [48]	$\delta = 0.00$ $\lambda = 2$	$\delta = 0.03$ $\lambda = 0$
$L_1 : L_2$	$1 : 0.083(3)$	$1 : 0.095(2)$	$1 : 0.11(2)$	$1 : 0.081$	$1 : 0.093$
$L_1 : L_3$	$1 : 0.018(4)$	$1 : 0.023(5)$	$1 : 0.041(2)$	$1 : 0.020$	$1 : 0.039$
$L_1 : M_1$	$1 : 0.21(1)$	–	–	$1 : 0.20$	$1 : 0.20$
$M_1 : M_2$	$1 : 0.099(6)$	$1 : 0.100(3)$	–	$1 : 0.087$	$1 : 0.098$
$M_1 : M_3$	$1 : 0.029(7)$	$1 : 0.030(5)$	–	$1 : 0.022$	1:0.040
$M_1 : N_1$	$1 : 0.20(1)$	$1 : 0.21(1)$	–	$1 : 0.20$	$1 : 0.20$

Chapter 5

High-energy Auger measurement results and discussion

If the Auger electrons are emitted from an atom with an initial vacancy in the K-shell, then these electrons are called K-Auger electrons. In this experiment the KLL-Auger spectrum was measured together with the L_1-conversion line since the L_1-conversion line is intense and close to the K-Auger line in energy (see Figure 2.12). In this chapter the challenge created by the background during the iodine measurement and the measured KLL-Auger spectra from the decay of excited ^{125}Te using the EMS spectrometer is presented. The same fitting procedures were employed for KLL-Auger lines as in the previous chapter (conversion lines). Moreover, energies and relative intensities of these spectral lines are compared with those calculated by BrIccEmis and those found in the literature.

5.1 Background challenge

One of the problems encountered during the ^{125}I measurement was that the background count rate increased over time. In our case, there are two types of background that can affect the measurement: a) Iodine slowly effusing from the sample through the analyser toward the detector, and hence contributing counts which are independent of the voltages on the analyser. This background contribution increases during the measurement and, as a consequence, it is not really possible to measure the weak signals later on in the measurement series. Figure 5.1 shows how the background increases after a certain period of time. b) Decay electrons that have lost energy upon entry into the gold appear under the Auger peak as a background count. This type of background is more pronounced in the LMM-Auger spectra which will be discussed in the next chapter. Figure 5.2 shows schematically how electrons emitted by iodine interact with the gold.

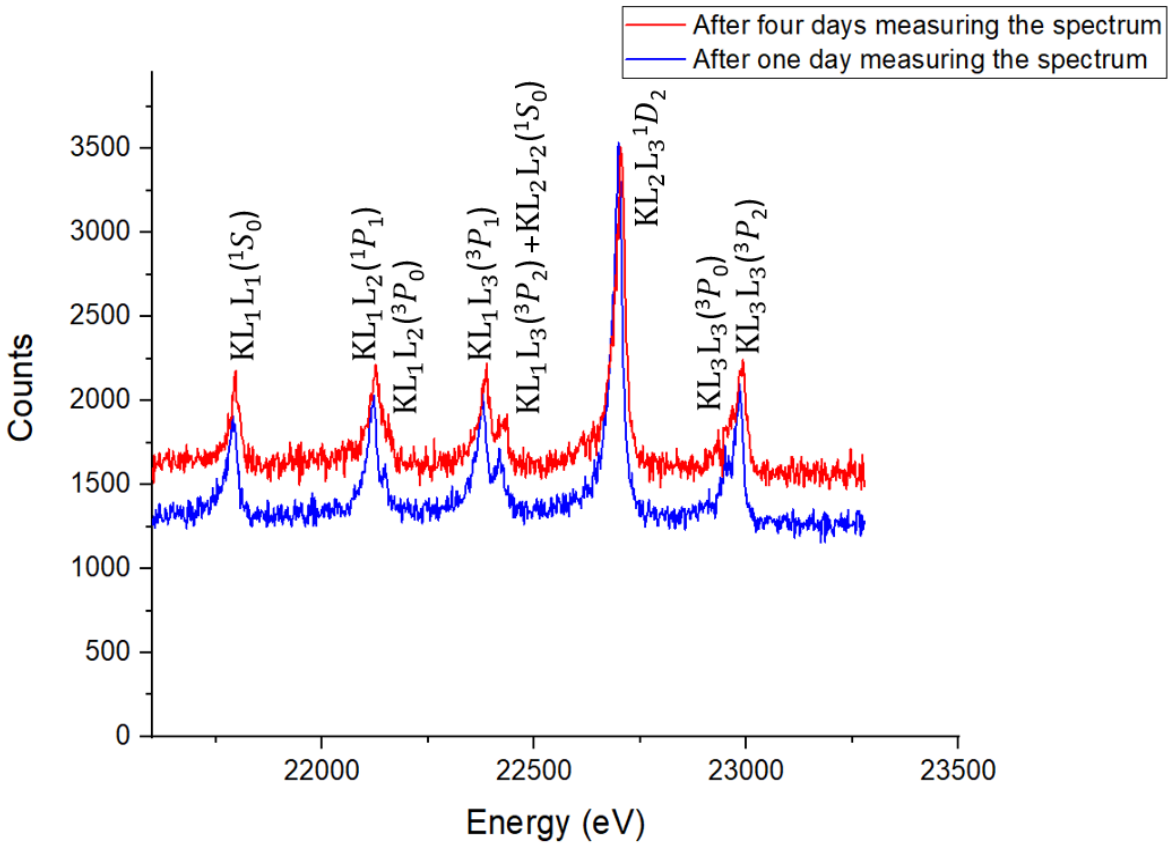

Figure 5.1: The measured KLL-Auger spectrum. The red spectrum shows how the background increases after 4 days. The red spectrum was scaled to match the KL_2L_3 height of the blue spectrum. By fitting the spectrum with the origin software then Figure 5.3 is obtained.

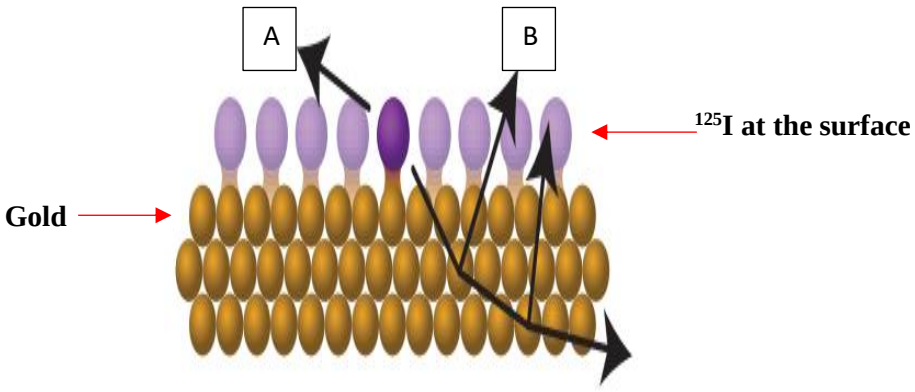

Figure 5.2: Auger electrons emit from ^{125}I in two different ways. A: emission directly from the surface without any interaction with gold. B: Auger electrons interact with the gold substrate, lose energy and are measured after being deflected by Au towards the analyser. The image was extracted from [53].

5.2 The *KLL* Auger spectrum

Much research has been conducted on the *KLL*-Auger group due to their intensity and isolation from other *K*-Auger groups, and their energies and intensity ratios are relatively well established [49-52]. However, the *KLL*-Auger line to conversion line intensity ratio has rarely been studied for any radionuclide. This ratio allows us to determine how many Auger electrons are emitted per nuclear decay, which is very important in medical applications.

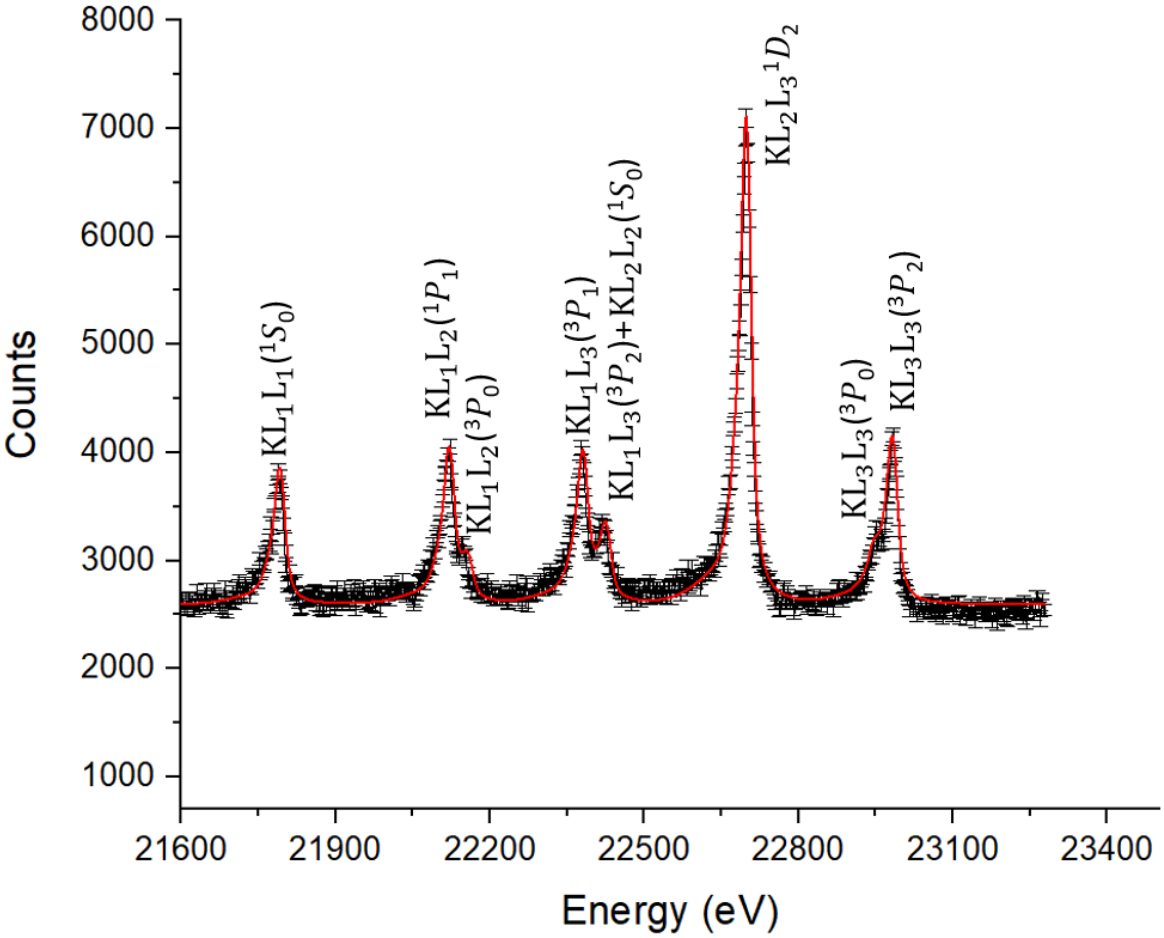

Figure 5.3: The measured *KLL*-Auger spectrum which is obtained at an energy resolution of 6.6 eV including the fit (red) with eight components as suggested by the semiempirical theory of Larkins [57].

The relevant spectrum is shown in Figure 5.3. The KLL-Auger spectrum consists of several peaks spread over more than 1 keV. The natural widths of each KLL-Auger line can be estimated as the sums of the level widths involved during the transitions. They were calculated by Krause et al. [133] and are used in the present work. As the K and L level widths are approximately 10 eV and 3 eV respectively, the KLL-Auger line widths are of the order of 16 eV.

Atomic structure effects due to the differences in electronic structure after electron capture and conversion electron emission also contribute to the broadening of the Auger lines. Details of the atomic structure effect were discussed in section 2.4.5. The energy difference between these two Auger decays is estimated to be 10 eV [138]. In order to account for the shift in energy due to the atomic structure effect a new parameter m_s was included during the fitting process. This enables each Auger peak to be split into two components with the same width. The intensities of both components are assumed to be the same. This is because the K vacancies initiated from EC and IC process contribute almost equally (see Table 2.3). With m_s unrestricted, the best fit for the shift is $m_s = 8 \pm 2$ eV, which is surprisingly close to what was found by Kovalik et al. [138] for the case of $^{131}\mathrm{X_e}$.

There are at least two ways of describing the KLL-Auger spectrum:
(i) One can characterize each final state in terms of the atomic orbitals they originate from and the total angular momentum and total spin quantum number of the final state. In principle, this leads to nine possible final states in the intermediate coupling scheme, that is: $KL_1L_1(^1S_0)$, $KL_1L_2(^1P_1)$, $KL_1L_2(^3P_0)$, $KL_1L_3(^3P_1)$, $KL_1L_3(^3P_2)$, $KL_2L_2(^1S_0)$, $KL_2L_3(^1D_2)$, $KL_3L_3(^3P_0)$ and $KL_3L_3(^3P_2)$ as discussed in section 2.4.6. However, the energies of $KL_1L_3(^3P_2)$ and $KL_2L_2(^1S_0)$ lines are too close ($\approx$ 5 eV apart) relative to their widths to be able to distinguish them. This is predicted from the calculations by Larkins [57] using the semi-empirical approach. Indeed, only eight peaks were resolved in the measured KLL Auger spectrum.

(ii) One can neglect the fine splitting and characterize the final state in terms of L_x only. Then there are six possible final states (L_1L_1, L_1L_2, L_1L_3, L_2L_2, L_2L_3, L_3L_3) but for ^{125}Te the KL_1L_3 and KL_2L_2 energies are almost identical and these two contributions will not be resolved; the spectrum then consists of five peaks. This approach is adopted in BrIccEmis [112] and remains

manageable when one calculates several steps down in the relaxation cascade, where more vacancies are present.

There were clearly eight different components observed in the KLL-Auger spectrum. The same tail parameters were implemented for all KLL-Auger lines, as were adopted for the L-conversion lines, in order to restrict the number of variables in the fit. Table 5.1 provides a comparison of observed KLL-Auger intensities (relative to the $KL_2L_3(^1D_2)$ line) for ^{125}I EC with those calculated using BrIccEmis [112] and by Chen et al. [106]. Also, the experimental transition energies are compared with BrIccEmis [112] and the tabulation of Larkins [57] are presented in Table 5.1.

Table 5.1: Energies and relative intensities of the KLL-Auger transitions from ^{125}I electron capture decay.

Transition	Energy (eV)			Relative Intensities		
	Exp.	BrIccEmis	Ref. [57]	Exp.	BrIccEmis	Ref. [106]
$KL_1L_1(^1S_0)$	21800(5)	21868	21810	0.262(5)	0.263	0.263
$KL_1L_2(^1P_1)$	22128(5)	} 22210	22131	0.296(10)	} 0.397	0.305
$KL_1L_2(^3P_0)$	22151(10)		22165	0.086(6)		0.093
$KL_1L_3(^3P_1)$	22390(5)	} 22490	22388	0.309(7)	} 0.457	0.289
$KL_1L_3(^3P_2)$+ $KL_2L_2(^1S_0)$	22423(5)		22437	0.153(6)		0.168
$KL_2L_3(^1D_2)$	22702(3)	22792	22708	1	1	1
$KL_3L_3(^3P_0)$	22948(10)	} 23068	22955	0.071(6)	} 0.436	0.077
$KL_3L_3(^3P_2)$	22995(10)		22989	0.364(7)		0.360

As discussed in section 2.5, BrIccEmis is not able to calculate the intensity of each multiplet, as its calculations are based on the jj-coupling scheme. However, since the combined intensity of the multiplets will remain the same, they can be used to compare with the sum of both components of the experimental data. As can be seen from Table 5.1 the measured energies and intensities are consistent with the predicted values from Larkins [57] and Chen et al. [106]. Nonetheless, the energies calculated from BrIccEmis were overestimated by about 90 eV due to the absence of the Breit electron interaction and the quantum electrodynamics corrections (see section 2.5).

5.3 Discussion of the high energy conversion and Auger electrons intensity ratio

Figure 5.4 shows the comparison of the calculated KLL-Auger spectra and L_1CE line from BrIccEmis with experimental data. Note that L_1CE and KLL-Auger spectra were measured in a single measurement. The comparisons clearly show the discrepancy between the theoretical and experimental values of Auger to conversion intensity ratio. The combined L_1CE-KLL Auger measurement indicates that in the experiment the relative Auger intensity is about 20% higher than that calculated. In this section the discrepancy found in the K-Auger groups only is discussed.

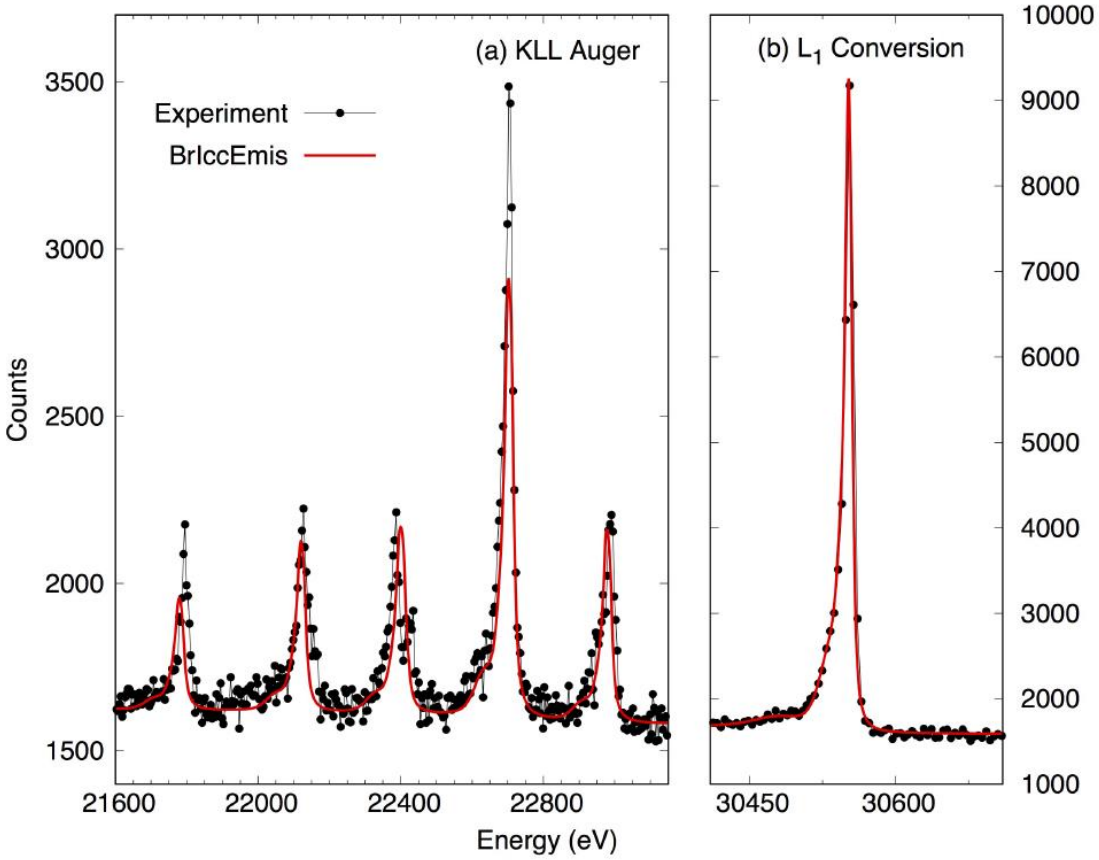

Figure 5.4: The KLL-Auger and L_1-conversion line spectrum (black curve) compared with BrIccEmis calculations (red curve). All calculated peaks intensities were scaled to the L_1 line. The energy of the calculated Auger spectrum was shifted down by 86 eV to match the experimental data. The increase in the background was calculated using the Shirley approach for both spectra.

The intensity ratio of the most intense Auger line, $KL_2L_3(^1D_2)$, to the L_1-conversion line was found to be $R_{KL_2L_3} = 1: 0.67(2)$, whereas the predicted ratio from BrIccEmis is $1: 0.53$. Thus, the difference is about $26(4)\%$. This rather unexpected result indicates that the predicted absolute intensity of either the Auger or conversion lines, or both, was estimated wrongly by $\approx 20\%$. The cause will be explained next.

5.3.1 *K* Auger and fluorescence yields

A core hole can either decay by X-ray emission (fluorescence) or by Auger decay. The fluorescence yield, ω_K is defined as the fraction of core holes that relaxes by X-ray emission. For the ^{125}Te K-shell, the best estimate of ω_K is ≈ 87.5 % [139, 140]. The EADL database used by BrIccEmis [110] also uses such a value. Some experimental values for ^{125}Te are considerably smaller $(82.3 \pm 7.3)\%$, but all are with considerable error bars (Singh et al. [141]). The K-shell Auger yield is proportional to $(1 - \omega_K)$. The corresponding Auger yield for the K-shell, based on theory, would be 12.5%, whereas the results of Singh et al. [141] correspond to an Auger yield of 17.7%, i.e. the measured fluorescence value from Singh would predict almost 50% larger Auger yield, a difference much larger than is required to describe the observed discrepancy in the conversion to Auger intensity ratio in our data. There is thus no experimental evidence that excludes the possibility that $\omega_K \approx 85\%$, a value that would describe our data quite well. For high Z elements, where ω_K approaches 1, the determination of the K-Auger yield is therefore an accurate way of determining the value of ω_K.

Besides the aforementioned fluorescence-yield measurements based on results from stable tellurium isotopes, there are measurements based on coincidences between γ and X-rays for the case of the decay of ^{125}I [142], which gave a value of the fluorescence rate of $(85.9 \pm 2.2)\%$. It is worth noting that the measurement described here, based exclusively on the measurement of electron intensities, agrees with the measurement of Karttunen et al. [142], which relies solely on X- and γ-ray intensities. Table 5.2 and Figure 5.5 show the comparison between our measured ω_K^{exp} with these semi-emperical values, and the reported values. It is apparent from Table 5.2 that our measured ω_K^{exp} value is consistent with other measurements, but with a statistical error of only 2%. It should also be noted that, all other experiments [141-145] employed methods which involved X-ray measurements, whereas in the present work, to the author's best knowledge, it is the first experiment that employs the Auger to conversion electron intensity ratio to determine the K fluorescence yield for tellurium.

Table 5.2: K fluorescence yield (ω_K) compilation for tellurium from the literatures.

ω_K	Reference	Method
0.859(22)	Karttunen et al. (1969)[142]	Measurement of (K X-ray)-(K CE) coincidences
0.873(17)	Tolea et al. (1974)[143]	Measurement of (K X-ray)-(γ-ray) coincidences
0.823(73)	Singh et al. (1990)[141]	Fluorescent excitation of solid targets
0.879(54)	Ozdemir et al. (2002)[144]	K X-ray and γ-ray spectroscopy
0.840(32)	Yashoda et al. (2005)[145]	Fluorescent excitation of solid targets
0.850(15)	Present work	Auger to CE intensity ratio
0.865(30)	Grotheer et al. (1969)[91]	Semi-empirical fit
0.868(5)	Kahoul et al. (2010)[88]	Semi-empirical fit
0.878(20)	EADL (Perkins, 1991)[110]	Theoretical calculations

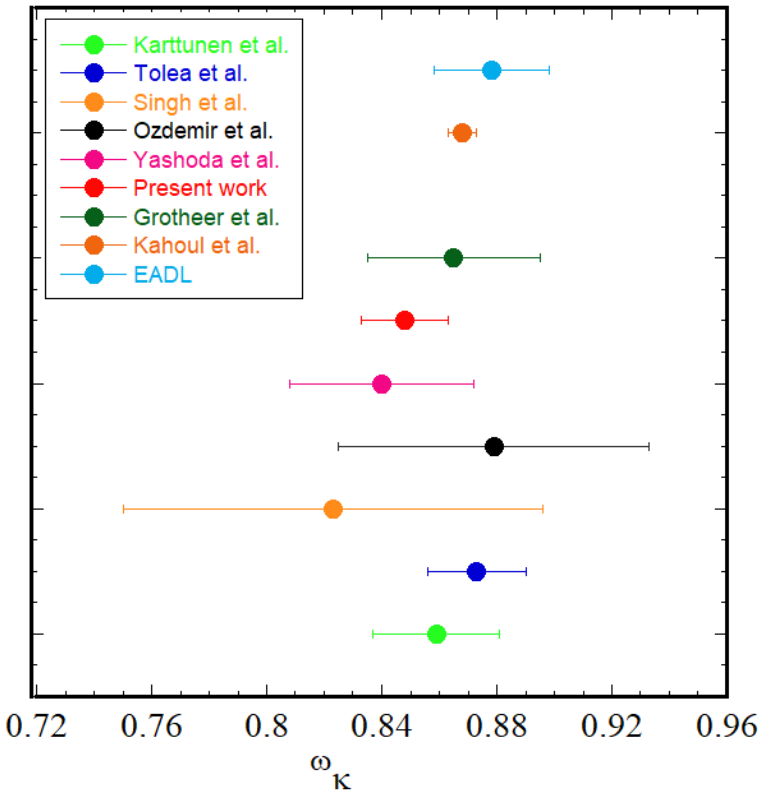

Figure 5.5: Comparison of K fluorescence yields in the atomic number $Z = 52$ (Tellurium) obtained using different methods. The methods are tabulated in Table 5.2.

5.3.2 Influence of the nuclear parameters

In chapter 4, from the conversion line measurements, the penetration parameter was evaluated to be $\lambda = 2.0 \pm 2.0$ and the mixing ratio was found to be $\Delta = 0.00$.

So, since the uncertainty in λ is large, there is no absolute evidence to show the presence of the penetration effect in the 35 keV transition of ^{125}Te.

Despite this, if the penetration effect had been taken into account, it might change the conversion coefficients, and thus the absolute intensity of the conversion line. As a result, this could subsequently influence the determined Auger yields. Table 5.3 shows the calculated a_K, when the penetration effect is assumed. The values of some associated parameters are presented in the table as well. The calculated K Auger yield, when penetration effect is taken into account, is $a_K = 0.149$. Thus, under penetration effect, a_K decreases by about 2%. The L_1-conversion electron intensity decreases by 3%. The corresponding ω_K then has a much smaller change ($\approx$ 0.4%). It can thus be concluded that the influence of the nuclear parameter on the derived fluorescence yield is minor.

Table 5.3: The calculated gamma intensity, L_1-conversion electron intensity and K-Auger yield as obtained for different penetration parameters λ.

Parameters	$\lambda = 0$	Auger yield $[a_K(\lambda = 0)]$	$\lambda = 2$	Auger yield $[a_K(\lambda = 2)]$
I_γ	0.0684	0.152	0.0687	0.149
α_{L_1}	1.413		1.374	

5.4 Summary

In conclusion, The KLL-Auger spectra were measured together with L_1-CE line. Energies of the KLL-Auger lines were found to be in reasonably agreement with the literature and BrIccEmis calculations. However, the intensity ratio of the KLL-Auger line to the L_1-CE line was found to be underestimated in BrIccEmis by 20%. This discrepancy can not be attributed to the influence of the penetration parameter. This discrepancy between the measurement and BriccEmis, which adopts the transition rate from the EADL database, has to be attributed to the slight overestimation of the fluorscence rate in the database BrIccEmis uses.

Chapter 6

Low-energy Auger measurement results and discussion

In this chapter, the low-energy electron spectra (MNN, LMM and LMN), which are in the energy range from 100 eV to 4 keV, were measured using the super-CMA. The K-conversion electrons have an energy of 3.679 keV, which is within the energy region of the LMM and LMN Auger transitions. This therefore provides another opportunity to establish the ratio of conversion electrons to Auger intensities experimentally. In addition, the EMS spectrometer was used to measure the spectra from 2.9 keV to 3.8 keV in order to measure the intensity ratio with a better energy resolution.

6.1 LMM and LMNAuger spectra

The spectra produced by the super-CMA were analysed with two different approaches. The initial approach was to fit the spectra using the Origin software [124] and then compare the intensities and energies of the various Auger lines with Casey and Albridge [48], since in their work there is no information given in terms of the relative intensity of K-CE to the Auger peaks. The second approach was to compare the intensities and energies of the K-CE and the Auger peaks from the calculated BrIccEmis spectra to the measured spectra.

The energy and relative intensity of the labelled peaks (as shown in Figure 6.1) are compared with the BrIccEmis and literature as presented in Table 6.1. As shown in the second part of Table 6.1, peaks 6,7and 8 are taken together because they are partly overlapping.

6.1.1 Fitting approach

The fitting approach will be first focus. The fitting procedure similar to that of the L-conversion line, where the Gaussian width represents the resolution of the spectrometer, and the Lorentzian width represents the lifetime broadening of the associated transition level(s). It was implemented to fit the L-Auger and K-conversion spectra. Both the $1/E^{0.8}$ efficiency dependence, where E is the electron energy, and the correction of the lifetime broadening for the K-conversion line were taken into account. Auger lines and the conversion lines were assumed to have the same tail parameters during the fit, but different from the L-conversion line parameters. The natural width of the K-conversion line was adopted from Campbell et

al.[129]. The Lorentzian widths of the Auger lines were allowed to be free parameters, as in reality many Auger peaks consist of a series of contributions at slightly different energies. Figure 6.1 presents the fitted L-Auger and K-CE spectrum. Note the energy resolution of the measured spectrum shown in Figure 6.1 is about 9 eV. This was determined from the elastic peak experiment as discussed in chapter 3, section 3.3.1.

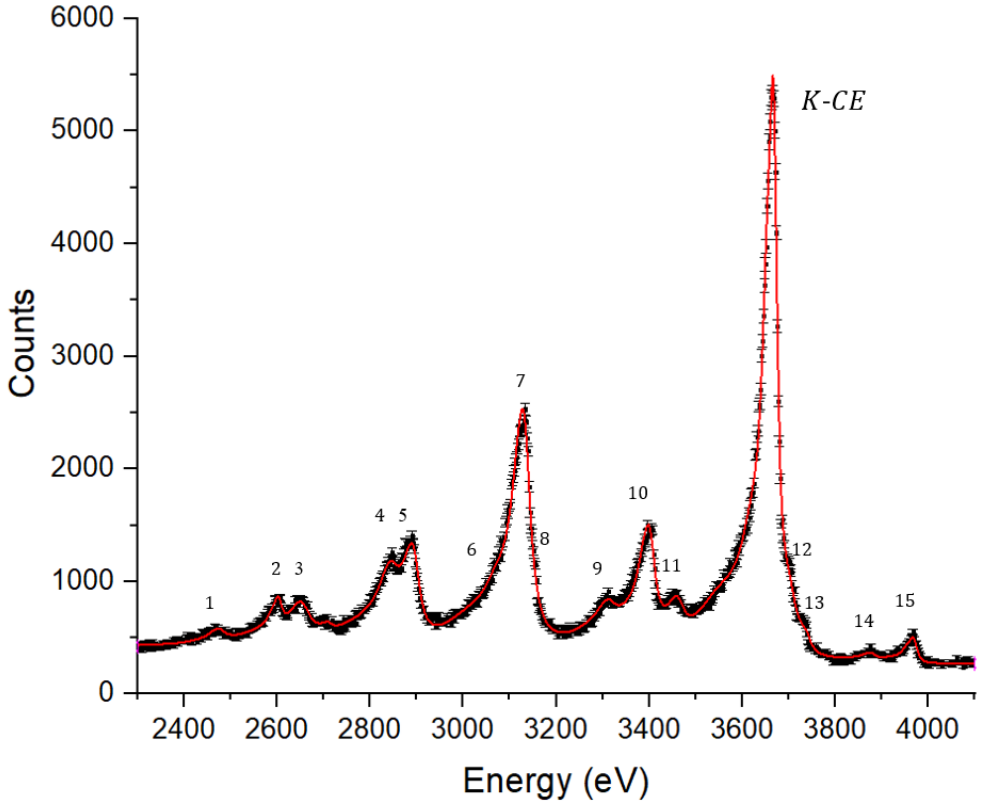

Figure 6.1: The measured spectrum of K-conversion and LMM and LMN Auger electrons using super-CMA spectrometer. The spectrum is fitted (red line) with 15 peaks. There is significant overlap between the LMM and LMN Auger spectra. Thus it is difficult to assess the exact line shape. As a result, the LMM and LMN Auger spectra were analysed together. The peaks are numbered for identification purposes. The increment in the background was subtracted using the Shirley background approach.

An attempt was made to fit the L-Auger and K-conversion spectra with the same tail parameters as the L-conversion line (as discussed in chapter 4, section 4.2). In addition, the associated background was calculated using Shirley background approach [134]. However, such an approach failed, as shown in Figure 6.2. This failure may have been a result of the super-CMA spectrometer response being different (non-Gaussian) from the EMS spectrometer (more details of the super-CMA limitation will be presented in section 6.2.4). It could also be due to different interactions of the lower-energy electrons with their environment.

The strongest line is the $K\text{-}CE$ line. There is some overlap between this line and neighbouring Auger lines. This close proximity (from 2.5 keV to 4 keV) means that corrections due to the energy dependence of the analyser efficiency are small. It was observed that the $K\text{-}CE$ line is broader than the other conversion lines measured with the EMS, shown in Figure 4.2. This is partly due to the larger lifetime broadening of the K hole ($\approx$ 9.9 eV versus 2.2 eV, 2.84 eV and 2.62 eV for the L_1, L_2 and L_3 respectively [129]).

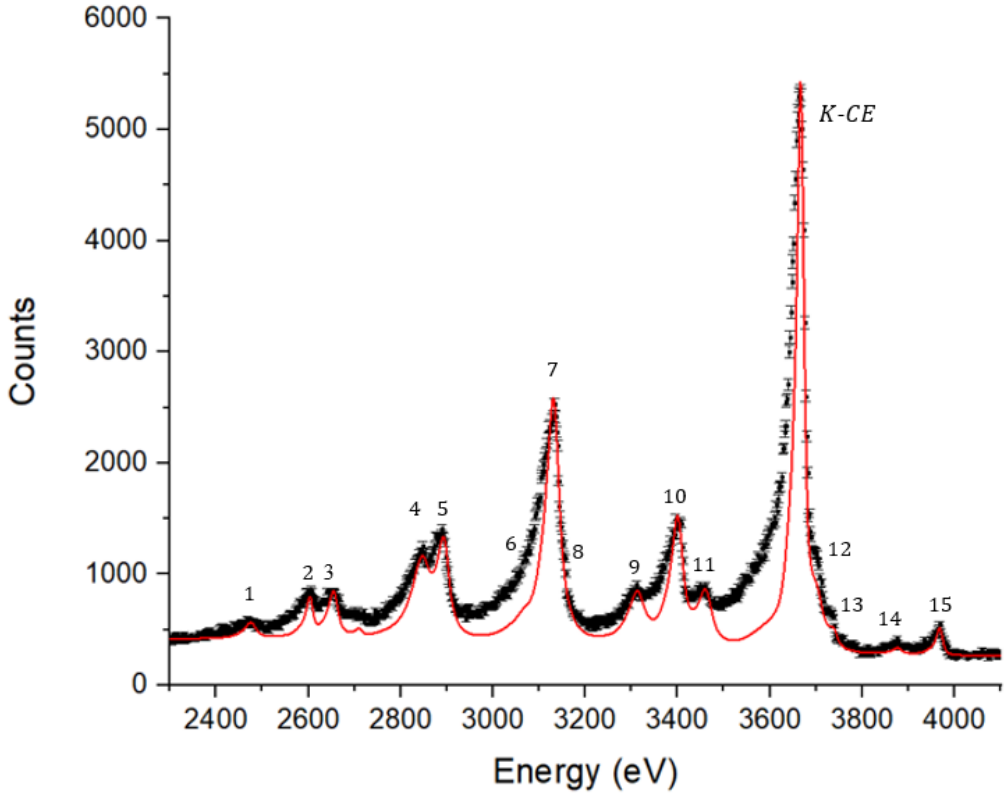

Figure 6.2: The K-conversion and LMM and LMN Auger spectrum fit with same tail parameters as the L-conversion line (taking into account their different lifetime broadening). The increment in the background was subtracted using the Shirley background approach. Note this spectrum is identical to the measured spectrum in Figure 6.1.

The L-Auger peaks together with the K-CE line were compared with the results of Casey and Albridge [48] measured using a magnetic spectrometer, as shown in Figure 6.3. It was found that on the low energy side (< 2800 eV) the present result shows much better defined peaks than the Casey and Albridge results. In addition, the present measurement has a better resolution. Hence the areas of the Auger and conversion lines can be determined more accurately.

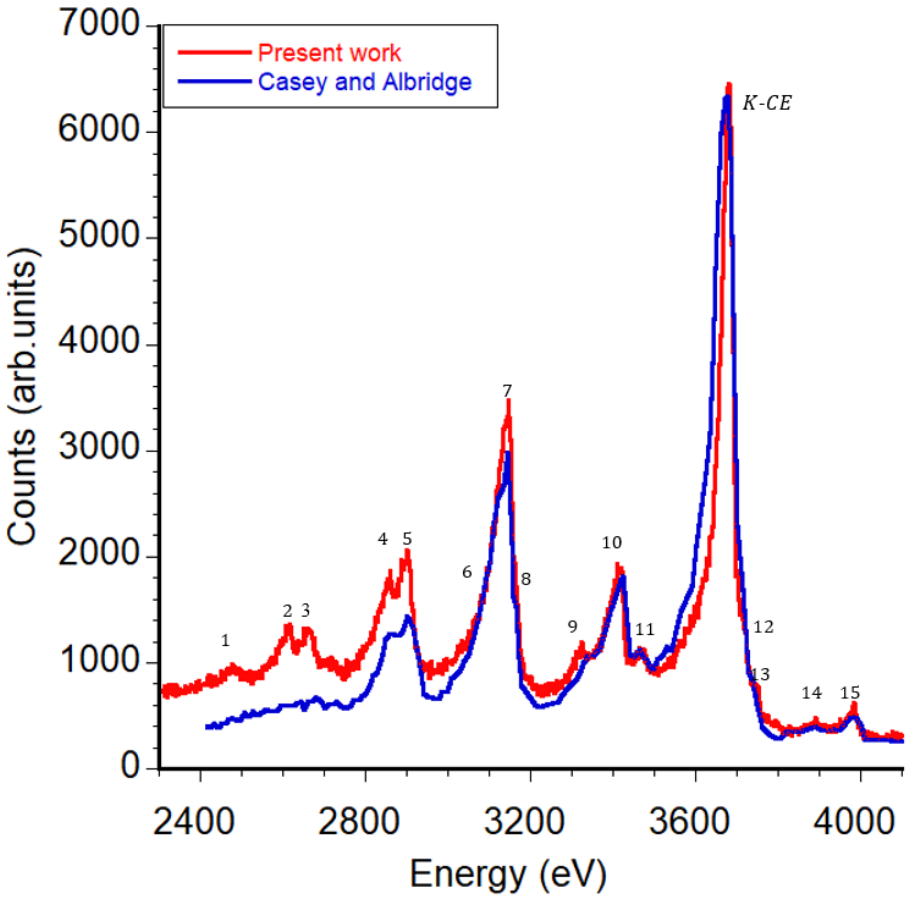

Figure 6.3: Comparison of the L-Auger spectrum of tellurium measured using the super-CMA with the Casey and Albridge spectrum [48]. The super-CMA spectrum is identical to the measured spectrum in Figure 6.1 (from $\approx$ 2 keV to 4 keV). The energy resolution of the present measurement is significantly better than the Casey and Albridge spectrum. Their data were digitised for comparison with the present measurement. Note that the data from the present measurement was scaled to match the height of the conversion line (labelled as K-CE) of the Casey and Albridge data.

In order to determine the appropriate dose to cells, an accurate knowledge of Auger yields is required. The spectrum was fitted and the ratio of the sum of all L-Auger intensities to K-conversion line intensity was determined. This approach showed that the intensity ratio of the L-Auger lines to K-conversion line ($\frac{\mathrm{I_{LMM}}}{\mathrm{I}_{K-CE}}$), as shown in Figure 6.1, was $\frac{\mathrm{I_{LMM}}}{\mathrm{I}_{K-CE}} = 1.99 \pm 0.11$. A value close to 2 is expected as there are two different cascades, which originate from either electron capture or internal conversion, each of which will almost always have at least one LMM or LMN transition. Note the experimental data had been multiplied by $1/E^{0.8}$ to take out the variation due to analyser transmission.

The K-conversion line and peaks 12,13 overlap. If the peak decomposition is not correctly accounted for, then an incorrect intensity ratio will obtained. This can be investigated by reconstructing the spectrum based on theory (BrIccEmis).

6.1.2 Comparison of fitting and BrIccEmis

The measured spectrum is now compared with the theoretical model BrIccEmis (second approach). BrIccEmis is based on the known intensity of the K-conversion electron, estimates of the decay rates for Auger and X-ray emission [112] (details of how BrIccEmis works were discussed in chapter 2, section 2.5). Indeed, a similar structure as that measured is obtained, see Figure 6.4. Thus, the relative intensity of the conversion line to the Auger peaks from BrIccEmis will now be compared with the measured spectrum.

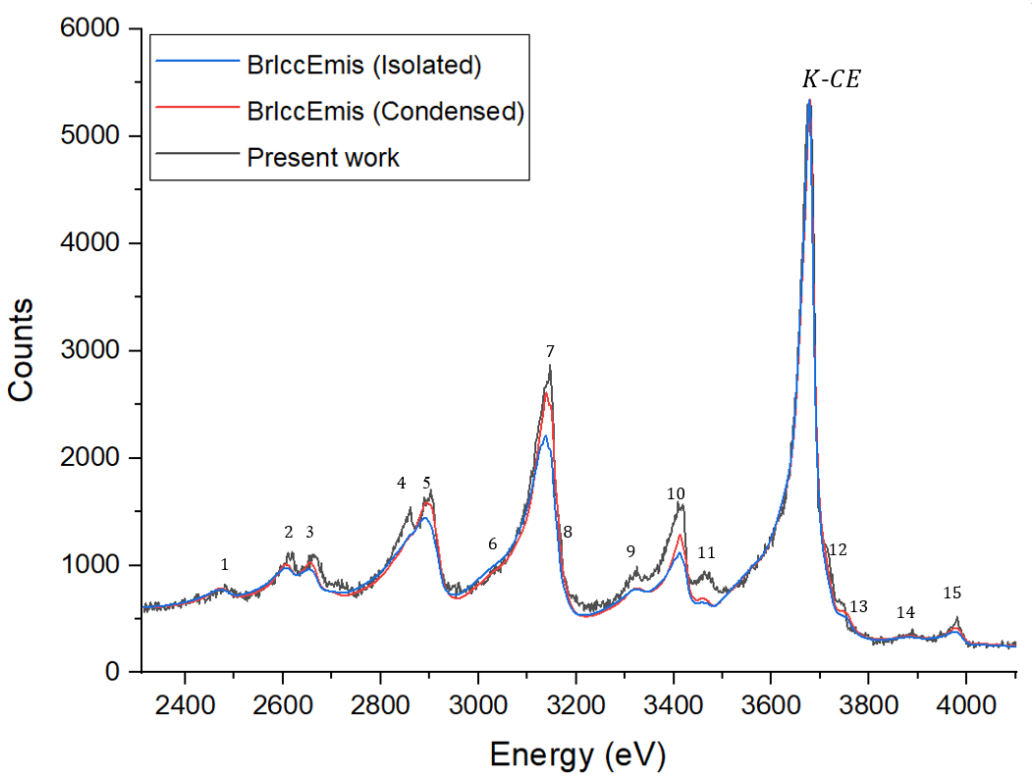

Figure 6.4: The measured spectrum (black line) of the conversion line and L-Auger lines. Two calculation spectra are compared with the measurement; one is the condensed-phase approximation (red line), which adopts the fast neutralisation and another one is isolated atom approximation (blue line), which adopts slow neutralisation. The experiment and theory were scaled using the height of the $K\text{-}CE$ line as a reference. Shirley background has been applied to the BrIccEmis calculation to account for the step increment in the measured background.

Figure 6.4 presents the L-Auger and $K\text{-}CE$ spectra produced by BrIccEmis together with our experimental data. From the fitting (Figure 6.1), fifteen peaks were identified and by comparing the energies of these 15 peaks with those based on the calculated energies, the intensity of each of the many transitions calculated in BrIccEmis was assigned to each of these 15 peaks.

The same approach (sum of all L-Auger intensities to K-conversion line intensity) was applied to the results of BrIccEmis simulation (condensed) and it was found that the intensity ratio $\frac{I_{LMM}}{I_{K-CE}} = 1.94$, which means that the theoretical L-Auger intensities to K-conversion line intensity is less than the one obtained by the fitting procedure by only ≈ 2-3%. However, looking at Figure 6.4, there is clearly an underestimation of the theoretical Auger intensities (at least 10 % less), especially in the energy range from 3300 eV to 3500 eV.

Table 6.1: Energy and relative intensities of the LMM and LMN from the EC decay of the ^{125}I comparison table. Note the number in square brackets (column 7) refers to the peak assignment in the Casey and Albridge paper [48].

NO.	Transition	Energy (eV)			Relative Intensity		
		Exp.	Ref.[48]	BrIccEmis	Exp.	Ref.[48]	BrIccEmis
1	$L_3M_1M_3$	2477	–	2475	0.04(2)	–	0.03
2	$L_3M_2M_3$	2604	2583	2607	0.08(2)	[1] 0.13(2)	0.05
3	$L_3M_3M_3$ $L_2M_1M_2$ $L_3M_1M_4$ $L_3M_1M_5$	2656	2679	2659 2696 2708 2719	0.19(3)	[2+3] 0.11(2)	0.080
	$L_2M_1M_3$			2750			
4	$L_2M_2M_2$ $L_3M_2M_4$ $L_3M_2M_5$	2848	2835	2824 2848 2854	0.24(3)	[4] 0.24(3)	0.16
5	$L_1M_1M_1$ $L_2M_2M_3$ $L_3M_3M_4$ $L_3M_3M_5$ $L_2M_3M_3$	2895	2882	2886 2886 2881 2910 2933	0.35(3)	[5] 0.33(3)	0.22
6	$L_2M_1M_4$ $L_2M_1M_5$ $L_1M_1M_2$	3067	2988	2982 2993 3031	1	[6+7+8] 1	1
7	$L_1M_1M_3$ $L_2M_2M_4$ $L_2M_2M_5$ $L_3M_4M_4$	3133	3121	3084 3123 3128 3133			
8	$L_1M_2M_2$ $L_3M_4M_5$ $L_3M_1N_1$ $L_3M_5M_5$ $L_2M_3M_4$	3162	3141	3158 3143 3134 3154 3171			
	$L_2M_3M_5$ $L_1M_2M_3$ $L_3M_1N_3$ $L_1M_3M_3$			3185 3215 3193 3267			
9	$L_3M_1N_{4,5}$ $L_3M_2N_1$ $L_1M_1M_4$ $L_1M_1M_5$	3315	3303	3276 3270 3316 3327	0.12(2)	[9] 0.032(20)	0.032

Continuation of Table 6.1: Energy and relative intensities of the LMM and LMN from the EC decay of the ^{125}I comparison table.

No.	Transition	Energy (eV)			Relative Intensity		
		Exp.	Ref.[48]	BrIccEmis	Exp.	Ref.[48]	BrIccEmis
10	$L_3M_3N_1$ $L_3M_2N_{2,3}$ $L_2M_4M_4$ $L_3M_3N_{2,3}$ $L_2M_4M_5$ $L_3M_2N_{4,5}$ $L_2M_1N_1$ $L_2M_5M_5$ $L_1M_2M_4$	3402	3398	3330 3334 3407 3380 3417 3412 3408 3429 3457	0.42(2)	[10] 0.23(2)	0.18
11	$L_1M_2M_5$ $L_3M_3N_{4,5}$ $L_2M_1N_{2,3}$ $L_1M_3M_4$ $L_1M_3M_5$ $L_2M_1N_{4,5}$ $L_2M_2N_1$	3463	2438	3462 3465 3505 3457 3505 3519 3544	0.17(2)	[11] 0.07(10)	0.045
12	$L_2M_3N_{2,3}$ $L_2M_2N_{4,5}$ $L_3M_4N_{4,5}$ $L_3M_5N_{4,5}$ $L_1M_4M_4$ $L_1M_4M_5$ $L_2M_3N_{4,5}$	3703	3716	3646 3686 3704 3714 3741 3751 3738	0.22(4)	[13 + 14] 0.12(3)	0.27
13	$L_1M_5M_5$ $L_1M_1N_1$	3739	3754	3763 3742	0.046(3)	[15+16] 0.056(10)	0.044
	$L_1M_1N_{2,3}$			3800			
14	$L_2M_4N_1$ $L_2M_5N_1$ $L_1M_2N_1$ $L_1M_1N_{4,5}$	3878	3863	3836 3846 3878 3883	0.018(11)	[17] 0.034(10)	0.020
	$L_2M_4N_{2,3}$ $L_2M_5N_{2,3}$			3890 3896			
15	$L_1M_3N_1$ $L_1M_2N_{2,3}$ $L_2M_4N_{4,5}$ $L_2M_5N_{4,5}$ $L_1M_3N_{2,3}$	3969	3959	3931 3938 3979 3988 3985	0.06(12)	[18] 0.06(10)	0.04
K-CE		3668	3657	3676	1.88(10)	–	1.33

According to the BrIccEmis simulation there is an extra Auger peak beneath the $K\text{-}CE$ (see Figure 6.5). By accommodating the intensity of this "extra Auger peak" and fitting the measured spectrum again, a different L-Auger to K-conversion intensity ratio $\frac{\mathrm{I_{LMM}}}{\mathrm{I}_{K-CE}} \approx 2.16 \pm 0.11$ rather than 1.99 ± 0.10 is obtained. This procedure showed that the L-Auger intensity (relative to $K\text{-}CE$) was underestimated by 10% in BrIccEmis, which is consistent with Figure 6.4.

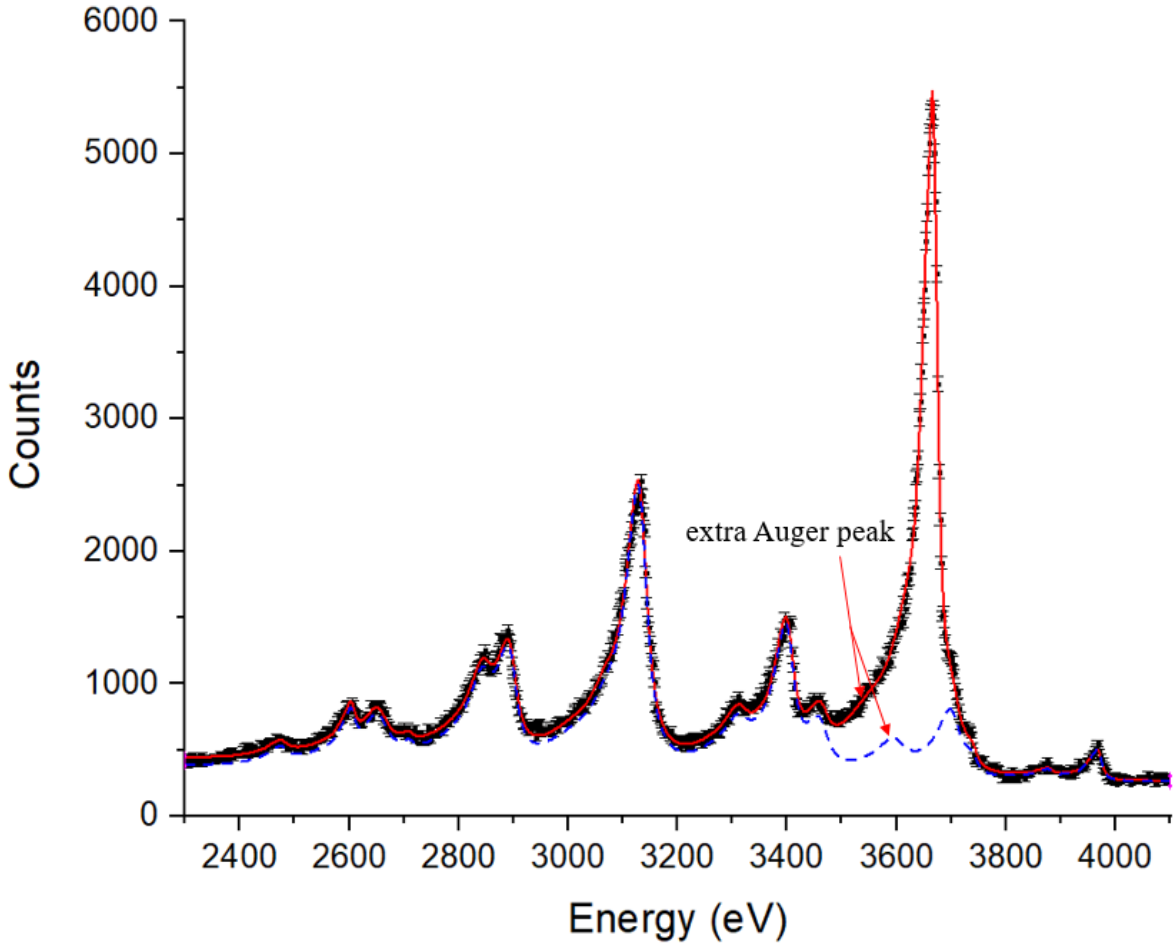

Figure 6.5: Second try of the fitting after taking an extra Auger component into account. The red line shows the fit of the L-Auger spectrum with 16 peaks.

Electron-beam induced Auger spectra from tellurium films were measured for comparison purposes (reader refer to [146] for more details), as shown in Figure 6.6. It was found that indeed there is an Auger intensity beneath the K-conversion line. The intensity of this Auger peak is in line with the "extra Auger peak" intensity assumed in Figure 6.5.

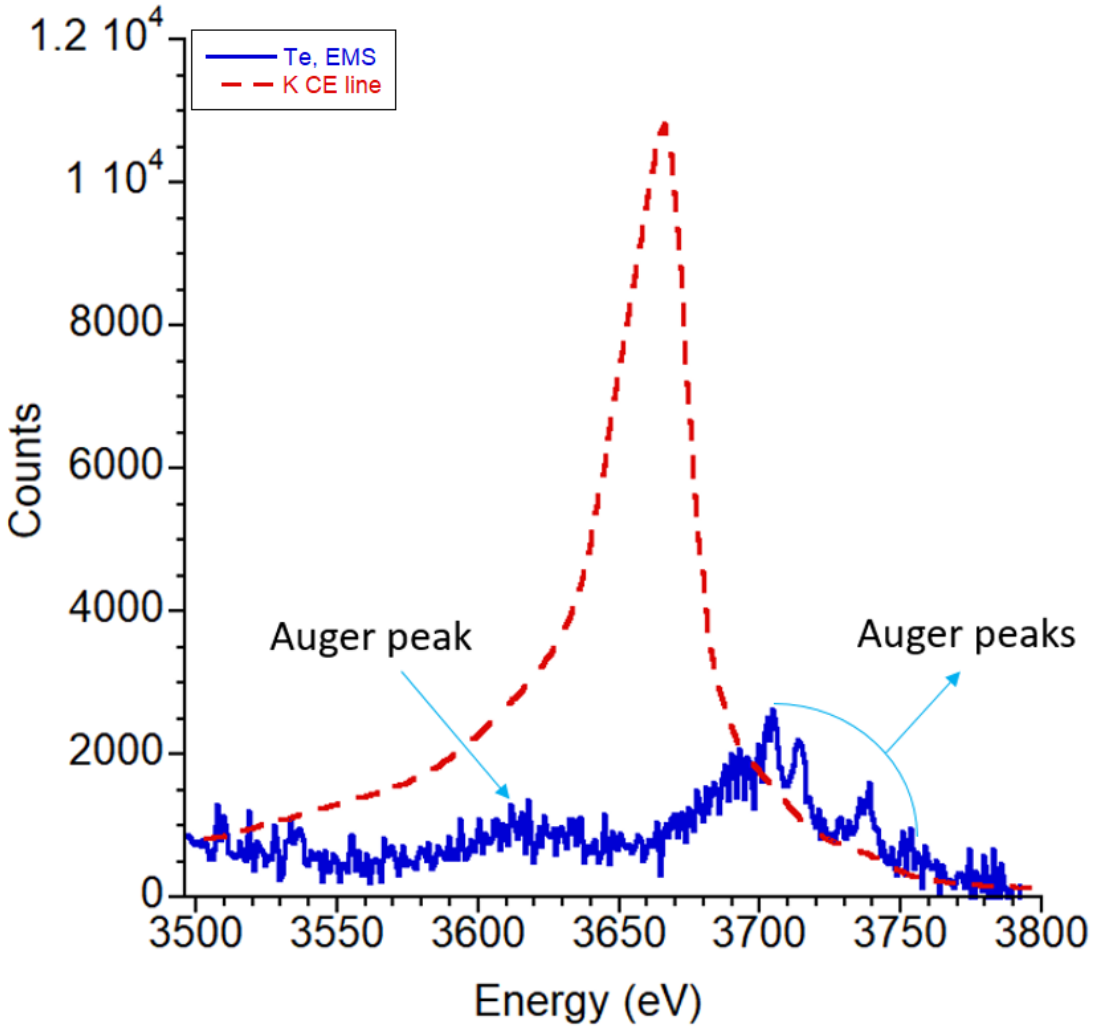

Figure 6.6: Electron beam induced tellurium spectrum measured using EMS spectrometer.

Based on these results one can conclude that there are about 2.16 ± 0.10 LMM and LMN Auger electrons are emitted per nuclear decay, whereas BrIccEmis simulates 1.94.

6.2 Discussion of the discrepancies

The comparisons showed clear evidence of discrepancies between theoretical and experimental intensity of Auger to conversion electron ratios. Therefore, four factors that could contribute to the discrepancy in the energy range from 2 keV to 4 keV are discussed. Note the LMM-Auger is generally the second step in the relaxation cascade, and hence its calculated intensity depends on the processes involved in the first step, e.g. on how the vacancies are distributed over the L_1, L_2 and L_3 shells after the first relaxation step.

6.2.1 Penetration effect

As was pointed out in section 5.3.2, the influence of the penetration effect on the KLL transition was found to be very small. It was also found that for the LMM-K spectrum case, the influence of the penetration effect on the Auger to conversion line ratio is not pronounced either. This is due to the low ($< 3\%$) change in K-conversion absolute intensity (α_K) under this effect, which can be seen in Table 6.3.

Table 6.3: The calculated gamma intensity, K-conversion electron intensity and L-Auger yield as obtained for different penetration parameters λ.

Parameters	$\lambda = 0$	Auger yield $[a_K(\lambda = 0)]$	$\lambda = 2$	Auger yield $[a_K(\lambda = 2)]$
I_γ	0.0684	19.46	0.0701	19.45
α_K	11.69		11.38	

6.2.2 L fluorescence yield

The discrepancy seen in the energy range from 2 keV to 4 keV cannot be attributed to uncertainty in fluorescence yield of the L-shell. The L fluorescence yield is low for Te (9%, [139]), thus the LMM-Auger intensity is not very sensitive to the fluorescence yield. The LMM-Auger to K-CE intensity ratio thus can not be attributed to uncertainty in this quantity.

6.2.3 Spectrometer efficiency

It was observed that the theoretical spectrum with a $1/E^{0.8}$ correction factor is in reasonable agreement with measured spectrum (below 600 eV will be discussed in detail in section 6.4). Thus, the transmission function of the super-CMA was assumed to follow the $1/E^{0.8}$ curve. As you can see from Figure 6.7, the intensity of the Auger peak at 3995 eV, which is at higher energy than $K\text{-}CE$ and hence should decreased due to the $1/E^{0.8}$ efficiency, is not lower than predicted by BrIccEmis. It was expected that if the discrepancy found between the measurement and the BrIccEmis (in the energy range from 2 keV to 4 keV) is due to the energy dependence of the spectrometer transmission then the measurement should be below or at most the same height as the BrIccEmis at 3995 eV, which is above the $K\text{-}CE$ energy. This is not the case. Thus, another important factor which could very reasonably explain this discrepancy is the atomic structure effect (see section 2.4.5 for more details on the atomic structure effect).

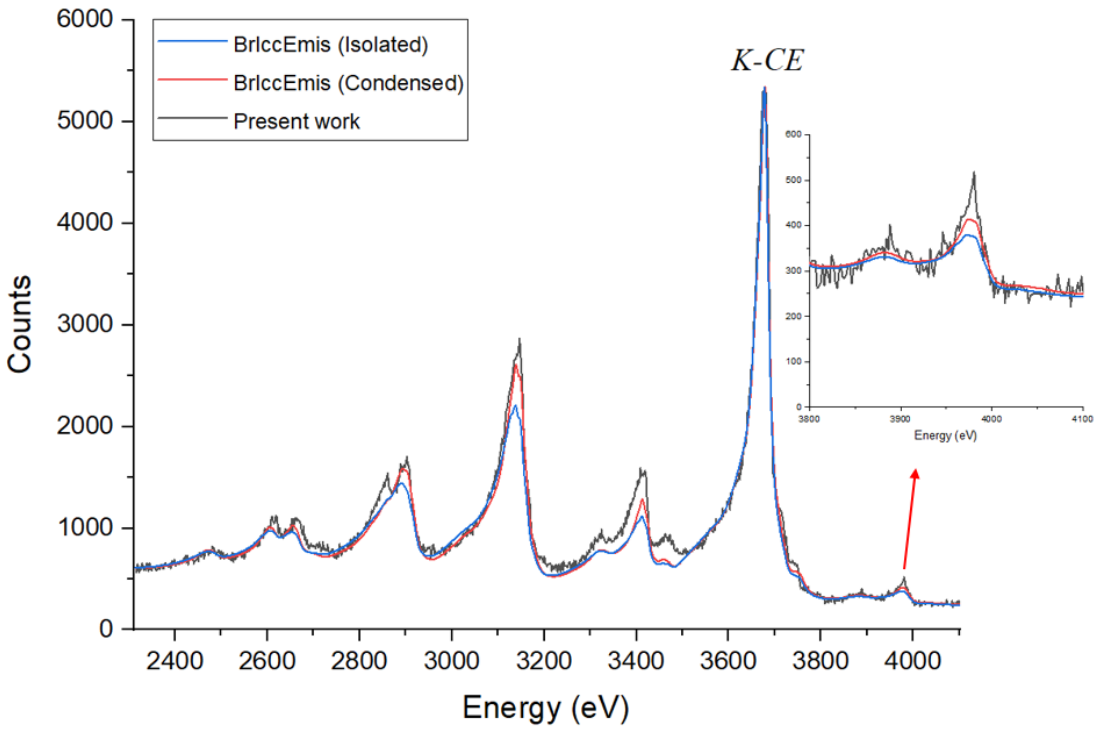

Figure 6.7: A comparison of the BrIccEmis calculation with the experiment scaled so the $K\text{-}CE$ lines has the same intensity. The BrIccEmis was scaled by $1/E^{0.8}$ to correct for the energy dependence of the transmission. The measured Auger intensity at energy larger than the $K\text{-}CE$ line as well as the Auger intensity at lower energies, is less than the simulated one. The discrepancy at high and low energy cannot be fixed by changing $1/E^{0.8}$ of the energy dependence of the transmission function.

6.2.4 Limitation of Super-CMA at high energies

Before discussing the atomic structure effect, it is necessary to first discuss the limitation of the super-CMA performance at high energies. The energy resolution of the super-CMA can be changed by altering the pass energy (PE) as discussed in section 3.3. It is generally assumed that setting a low PE should improve the energy resolution at the expense of a reduction in count rate. In the iodine measurement with the super-CMA, a 100 eV pass energy was selected, corresponding to an energy resolution of ≈ 9 eV. Such an energy resolution results in a degradation of the measured spectra. However, it was observed that for high energies the spectrometer does not operate well at lower PEs. This was attributed to the adverse effects associated with the increase in the deceleration ratio of the grids. The reader is referred to these papers [147, 148] for more details. Figure 6.8 shows the spectrometer operation with low PEs (35 eV PE and 50 eV PE) compared with 100 eV PE. From Figure 6.8, it appears there is a structure just next to the K-conversion line (labelled as $K\text{-}CE$). This structure is a consequence of focusing effects due to the grids, which becomes strong for large retardation i.e. when high kinetic energy electrons are measured at lower PE [147, 148]. As a result, the resolution is always insufficient to investigate the atomic structure effect using the super-CMA spectrometer. Quite likely this effect is already present at 100 eV PE causing the discrepancy seen in Figure 6.7.

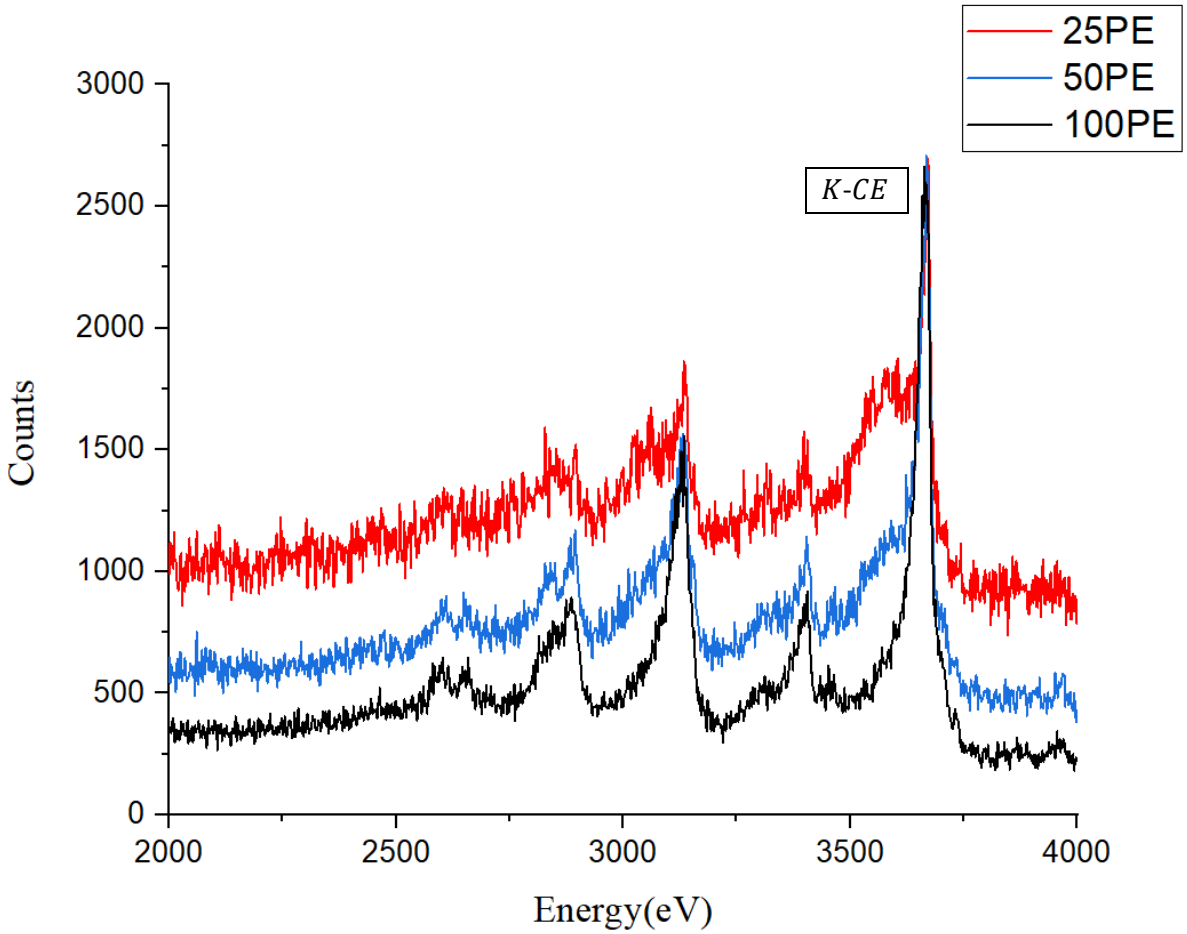

Figure 6.8: The LMN and LMM Auger spectra with different PEs. Red and blue spectra are scaled to match the K-conversion line height of the black spectrum. It is clear from the figure that the spectrum shape is affected significantly (see the structure next to the $K\text{-}CE$) by measuring the spectrum with low pass energies.

6.3 Atomic structure effect studied at high energy resolution using EMS spectrometer

In order to investigate the atomic structure effect in the LMN and LMM Auger spectrum, high energy resolution is required. Hence, the spectrum was measured using the EMS spectrometer. Figure 6.9 shows L-Auger and K-CE lines produced using both spectrometers (EMS and super-CMA). As is clear from the Figure that the spectrum measured using the EMS spectrometer has more structure and is also sharper than the one measured using the super-CMA spectrometer. However, the K-CE is not as sharp as the L-conversion line which was also measured using the EMS spectrometer (see chapter 4, section 4.2). This is at least in part due to the difference in the lifetime broadening ($\approx$ 9.9 eV versus 2.2 eV for the K and L_1 respectively), as mentioned in section 6.1.1. Note that due to the EMS spectrometer's limitation in the scan range in the high-energy resolution mode, the spectrum was only measured from 2.87 keV to 3.8 keV. The spectrum produced by the EMS spectrometer is then compared to the spectrum calculated by BrIccEmis as shown in Figure 6.10.

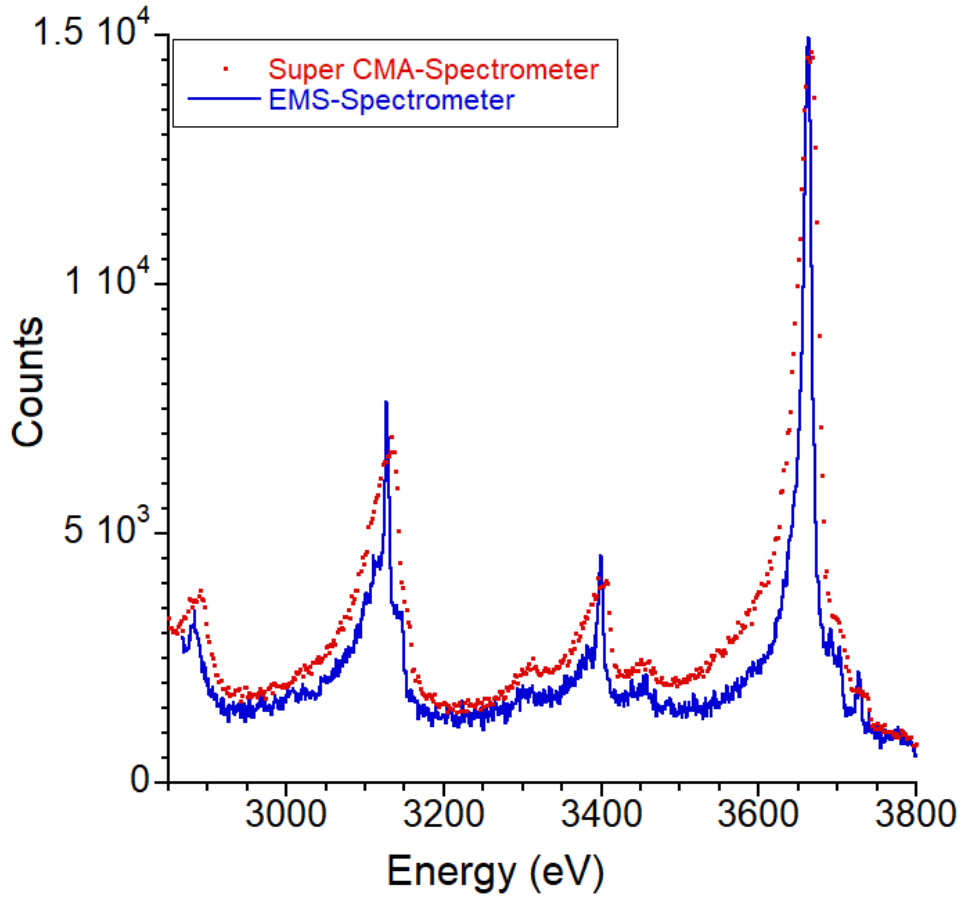

Figure 6.9: L-Auger and K-CE measured with both spectrometers (EMS versus super-CMA).

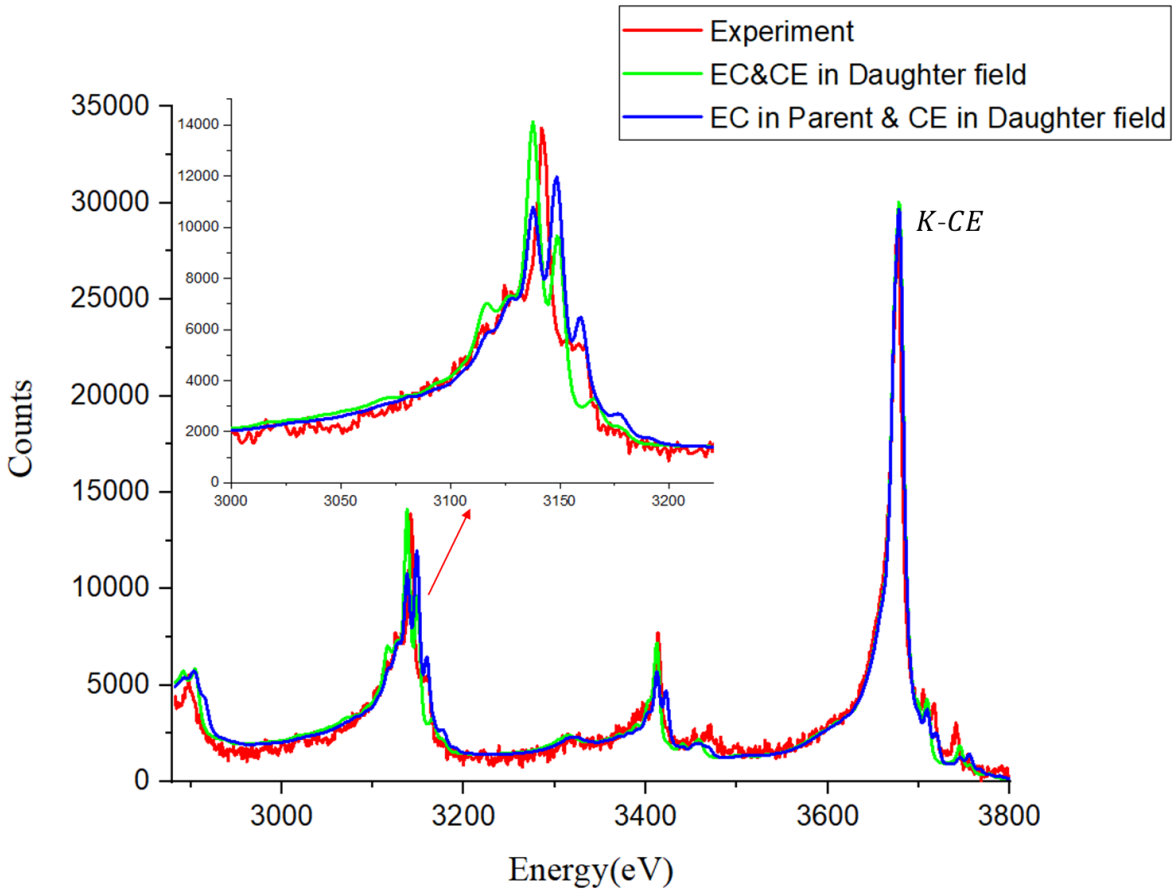

Figure 6.10: comparison of the low energy spectrum measured using EMS spectrometer and BrIccEmis. Theoretical spectra were scaled to match the maximum intensity of the main K-conversion line (labelled as $K\text{-}CE$).

Although the fact that the LMM and LMN Auger lines have less lifetime broadening than KLL, it was difficult to estimate the splitting of the peaks using the super-CMA spectrometer with its energy resolution (≈ 9 eV). As can be seen from the Figure 6.10 the discrepancy in intensities found using super-CMA (see Figure 6.4 or Figure 6.7) is not obvious anymore. This is because the atomic structure effect is neglected in the theoretical spectrum, and hence the spectrum fits much better with the measurement. Without the atomic structure effect, the theoretical Auger spectrum calculated using BrIccEmis (the blue line) after internal conversion and conversion electron emission will overlay each other and hence produce the green line, which is more consistent with what is obtained by the EMS spectrometer (red line). The green spectrum is a better representation of the experiment than the blue one.

Recall that the atomic structure effect in the KLL-Auger spectrum was accounted for during the fitting process (see section 5.2). This atomic structure effect required each measured Auger peak to be fitted with two, slightly shifted, contributions. The atomic structure effect in KLL is more pronounced than for the LLM-Auger spectra, and hence the KLL-Auger lines cannot be fitted well without taking the atomic structure effect into account. Figure 6.10 reveals that without accounting for the atomic structure effect, the theoretical spectrum fit is much better. This is probably due to the difference in lifetime of KLL and LMM Augers. The KLL lifetime is about 6.5×10^{-17} second while the LMM lifetime is about 2.1×10^{-16} second, i.e. KLL decays faster than LMM.

Immediately after an electron capture event, the atomic electron configuration remains in the iodine electron configuration. There is then an atomic relaxation process during which the electrons will be rearranged into the Te electron configuration, however this requires some time. An Auger electron could be emitted before, during, or after the atomic relaxation process, thus resulting in energy shifts in the Auger spectrum due to the changing binding energies of each shell. If the Auger emission occurs before the atomic configuration relaxation, its energy will be described as if in the iodine electron configuration, contributing to one peak, whereas if it occurs after reconfiguration into Te, or if it occurs as a result of internal conversion once the Te atom is formed, then another, different energy peak will be created, and appear in the spectrum as a widening of the peak such as is the case for the KLL-Auger spectrum shown in Figure 5.3.

In the case of the LMM-Auger electron emission after an electron capture process the absence of the atomic structure effect indicates that the L and M shell atomic electrons have enough time to reconfigure into the Te configuration prior to Auger emission. Therefore, the Auger electron emissions for both iodine electron capture and Te internal conversion appear at the same energy.

6.4 *MNN* low-energy Auger spectra

In the case of MNN Auger electrons (< 600 eV as shown in Figure 6.11), the level of the agreement between the measured and the theoretical spectra is not as good as in the LMM and LMN case. $1/E, 1/E^{0.6}$ and $1/E^{0.8}$ correction efficiency factors have been applied to the BrIccEmis calculation to model the influence of different spectrometer efficiencies. It is clear from Figure 6.11 that the comparison is strongly influenced by the energy dependence of the analyser efficiency. It is obvious that the theoretical spectrum with a $1/E^{0.8}$ effeciency factor, which is the factor obtained from the SIMION simulation approach (see section 3.3.1 for all approaches were used to determine the spectrometer efficiency), most closely resembles the experimental results.

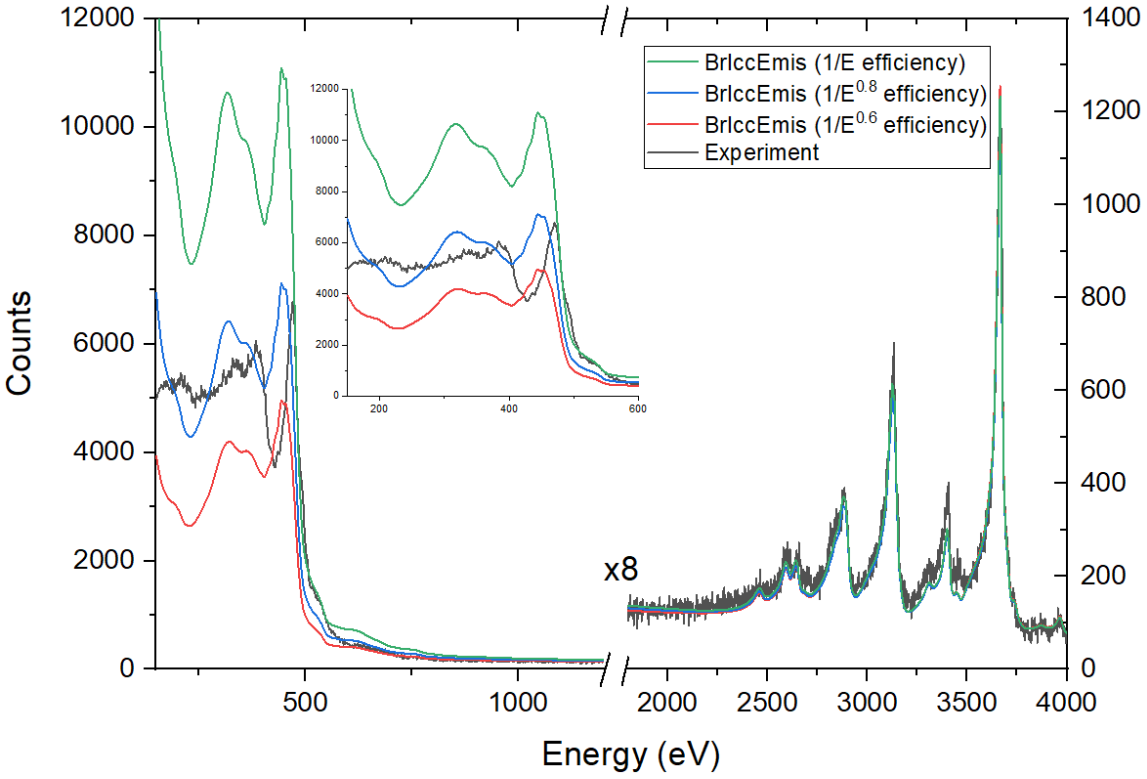

Figure 6.11: The low-energy Auger spectrum (100 eV- 4000 eV) compared with BrIccEmis (condensed-phase approximation) calculation from the decay of ^{125}I. The BrIccEmis calculation spectrum is scaled to match the intensity of the K-conversion electron (labelled as $K\text{-}CE$). $1/E, 1/E^{0.6}$ and $1/E^{0.8}$ correction factors to the efficiency and Shirley background have been applied to the BrIccEmis calculation to account for the spectrometer efficiency and the step increment in the measured background.

The two calculated spectra (condensed and isolated, as explained in section 2.5) with a $1/E^{0.8}$ correction factor are compared with the measured one as shown in Figure 6.12. It is obvious from the Figure 6.12 that the condensed-phase approximation is in better agreement with the measurement than the isolated-atom approximation as it predicts a peak near 450 eV, as observed in the experiment. This indicates that during the vacancy cascade of tellurium there are some electrons transferred from the gold substrate to the tellurium atom and the time scale of the transfer is comparable to the time scale of the vacancy cascade.

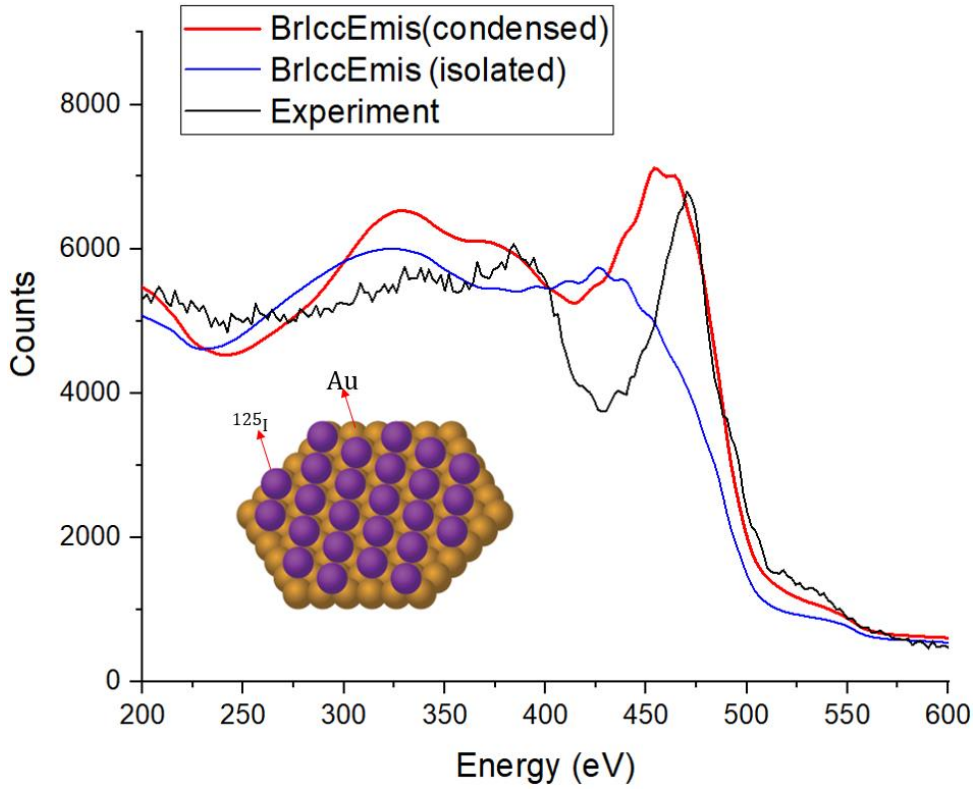

Figure 6.12: Comparison of very low-energy Auger spectrum (MNN) with the theoretical calculated from BrIccEmis. Also shown is the image (extracted from [53]) of a Au (111) surface covered by a third of a monolayer of ^{125}I.

6.5 Very low energies

At very low energies (< 200 eV), there are not only low energy Auger electrons ($M_{4,5}NN$ and NVV), but also secondary electrons. In this section, this very low energy region is investigated. However, there is an experimental problem. When one measures spectra using different pass energies, one obtains different shapes. However, there is a consistent shape (see Figure 6.13) at higher energies (above 200 eV). This means that the shape of the spectra in this energy range (200 eV to 600 eV) is not affected by the pass energy. In contrast, as can be seen from the same Figure, the shape of the spectra changes very rapidly with pass energy (as discussed in section 3.3.1) for electron energies from 200 eV down to $\approx$ 20 eV, which means that the spectrometer only works as expected if the energy of the measured electron is considerably larger than the PE. Thus, at lower energy the transmission deviates strongly from $1/E^{0.8}$. For the Auger electron emission with the initial vacancy in the N shell, BrIccEmis predicts a steep increase in counts above 100 eV (see Figure 6.13). As can be seen from the Figure there is a good agreement between BrIccEmis and the experiment for the low pass energy measurements. This indicates that Auger electron spectra can be measured down to the energy of 50 eV, provided that a low PE is used.

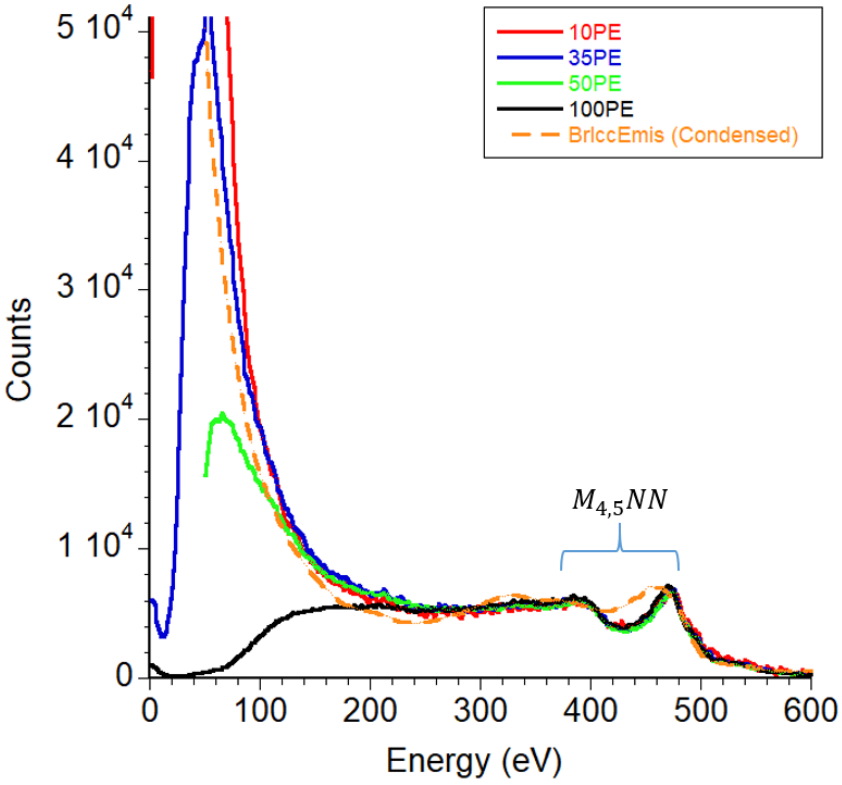

Figure 6.13: The influence of the pass energy on the spectrum below 200 eV. All measured spectra were scaled to match the maximum BrIccEmis intensity of the pronounced peak at ≈ 480 eV, which is the same height as the BrIccEmis results corrected for $1/E^{0.8}$ efficiency as shown in Figure 6.11.

6.6 Summary

The LMM-Auger lines were measured together with the K-conversion line using the super-CMA and EMS spectrometers. A 10% discrepancy was found between the measured Auger to conversion intensity ratio and the ratio predicted by BrIccEmis. Several factors have been considered to account for this discrepancy. However, the main factors that contribute to this discrepancy were found to be the energy resolution of spectrometer and the atomic structure effect. For MNN-Auger spectra it was found that the measured spectra are in a better agreement with condensed-phase approximation than the isolated-phase approximation.

For energies below 200 eV, when comparing the shape of the spectra measured at a different pass energy one finds that the shape is the same down to 2 times the largest pass energy used. For the low pass energy measurements there is good agreement with BrIccEmis down to 50 eV.

Chapter 7

Conclusion

Cancer is the world's second leading cause of death and was responsible for an estimated 9.6 million deaths in 2018. Globally, about 1 in six deaths are caused by cancer [1]. In the current study, the natural phenomenon called Auger electron emission is investigated and this process may be beneficial in the treatment of cancer. Auger electrons with kinetic energy less than one hundred eV exhibit a high average linear energy transfer of between 10 and 25 keV μm^{-1}. As a consequence, they have short ranges (several nm) in biological matter, and this makes Auger electrons attractive for cancer therapy.

7.1 Number of Auger electrons emitted per nuclear decay

For medical applications it is important to know how many Auger electrons are produced per nuclear decay. This was investigated for ^{125}I. The approach was to measure the Auger electron intensity to conversion electron intensity ratios as the intensity of conversion electrons per nuclear decay is well known. Table 7.1 shows the experimentally observed number of Auger electron produced per nuclear decay for the LMM and KLL Auger lines compared with BrIccEmis and some other calculations from the literature. Note in the case of BrIccEmis the EADL ω_K value of 87.9% was used as well as a modified ω_K value of 85.4% which is required to fit the experimental KLL-Auger intensity (details were discussed in section 5.3.1).

From Table 7.1 since ω_K was measured to be 85.4 rather than the EADL ω_K value of 87.9% this means the effect of Auger decay within microns of the emitter is increased by $\approx$ 20%. At distances smaller than the range of LMM Auger electrons $\approx$ 100 nm the effects remain largely unchanged.

Table 7.1: Comparison of the present measurement, BrIccEmis and the literature of the KLL and LMM Auger electrons produced per nuclear decay. Note every peak was taken into account during the fitting, so level of confident in these values is high.

Number of Auger electrons produced per nuclear decay					
Transition	Present measurement	BrIccEmis	BrIccEmis mod. ω_K	Stepanek [149]	Pomplum [150]
KLL	0.167 ± 0.308	0.130	0.155	0.126	0.134
LMM	–	1.22	1.24	1.22	1.25
LMM+LMN	2.16 ± 0.11	1.94	1.96	–	–

7.2 Summary of results

Two types of electron spectrometers were used in this experiment to measure the L,M,N CE lines and KLL, LMM Auger spectra from the decay of ^{125}I. The assumed line shape is essential for analysis of the ratio of the areas of the Auger and conversion lines. The approach that was used herein was generally to minimize the number of fitting parameters. The Gaussian width represents the resolution of the spectrometer, and the Lorentzian width was calculated from the literature level lifetimes. The same tail parameters were adopted to all measured peaks of the L-Auger and K-CE spectrum, but different from K-Auger and L-CE parameters. This approach assumes both Auger lines and conversion lines have the same shake probability; there is no detailed published description for shake probability in tellurium. Furthermore, a small increase in the background for all observed peaks was implemented using the Shirley background approach [134].

The KLL-Auger spectra were measured together with L_1-CE line. Eight lines were determined and identified for the KLL-Auger spectrum. Energies and intensity ratios of the KLL-Auger lines were determined and found to be in reasonably agreement with the literature and BrIccEmis calculations. However, the intensity ratio of the KLL-Auger line to the L_1-CE line was found to be underestimated in BrIccEmis by 20%. This discrepancy between the measurement and BriccEmis, which adopts the transition rate from EADL database, has to be attributed to the slight overestimation of the fluorscence rate in the database BrIccEmis uses.

The LMM-Auger group was measured together with the K-conversion line. Fifteen Auger lines were resolved in the spectrum. Energies and intensity ratios of the LMM Auger lines were investigated and found to be in reasonably good agreement with the literature and BrIccEmis. However, a 10% discrepancy was found (using the super-CMA sepectrometer) from the Auger to conversion line ratio when compared with BrIccEmis. In contrast, the L-Auger and K-CE spectra (from 2.87 keV to 3.87 keV) were measured using the high-energy spectrometer (EMS), and then compared with BrIccEmis spectra. It was concluded that the discrepancy found using super-CMA cannot be attributed to the penetration effect or uncertainty in the L yields. Instead, this discrepancy could possibly be attributed to peak distributions in the super-CMA spectrometer.

For the MNN-Auger spectra (in the energy range from $\approx$ 200 eV to $\approx$ 600 eV), the calculated spectra from BrIccEmis (condensed) was found to be in a better agreement with measured spectra than the BrIccEmis (isolated) calculation. Thus no multiple charged ions (as assumed in the isolated atom model) are formed in the final state, which would cause a shift in the MNN-Auger line to lower energies.

For the very low energy range (from $\approx$ 20 eV to $\approx$ 200 eV) it was realized that the spectrometer efficiency plays a crucial role especially when the high pass energies are used. For low pass energies a reasonable agreement with the BrIccEmis calculation was obtained.

Finally, the results of this study reveal that a comparison of the CE and Auger electron intensity after nuclear decay provides a crucial test of the theory and thus a clear way to improve databases, such as the EADL by Perkins et al.[110], that are widely used in simulating the effects of ionizing radiation in medical physics.

Bibliography

[1] World Health Organization. (2018). *Cancer*. Available: http://www.who.int/mediacentre/factsheets/fs297/en/

[2] US Department of Human Health Services. (2016). *US cancer death info.* Available: https://gis.cdc.gov/Cancer/USCS/DataViz.html.

[3] G. Delaney, S. Jacob, C. Featherstone, and M. Barton, "The role of radiotherapy in cancer treatment: estimating optimal utilization from a review of evidence-based clinical guidelines," *Cancer: Interdisciplinary International Journal of the American Cancer Society,* vol. 104, no. 6, pp. 1129-1137, 2005.

[4] Cancer Reasearch UK. (2016). *Cancer incidence statistics*. Available: http://www.cancerresearchuk.org/health-professional/cancer-statistics/worldwide-cancer/incidence#heading-One

[5] Australian Governmnet. (2019). *All cancers in Australia.* Available: https://canceraustralia.gov.au/affected-cancer/what-cancer/cancer-australia-statistics

[6] J. Vignard, G. Mirey, and B. Salles, "Ionizing-radiation induced DNA double-strand breaks: a direct and indirect lighting up," *Radiotherapy and Oncology,* vol. 108, no. 3, pp. 362-369, 2013.

[7] P. Nygren, "What is cancer chemotherapy?," *Acta Oncologica,* vol. 40, no. 2-3, pp. 166-174, 2001.

[8] Cancer Council. (2015). *Treatment side effects*. Available: https://www.cancercouncil.com.au/15307/b1000/living-well-after-cancer-45/living-well-after-cancer-treatment-side-effects/

[9] S. Forberg, E. Odeblad, R. Söremark, and S. Ullberg, "Autoradiography with isotopes emitting internal conversion electrons and Auger electrons," *Acta Radiologica: Therapy, Physics, Biology,* vol. 2, no. 4, pp. 241-262, 1964.

[10] B. Q. Lee, T. Kibédi, A. E. Stuchbery, and K. A. Robertson, "Atomic radiations in the decay of medical radioisotopes: a physics perspective," *Computational and Mathematical Methods in Medicine,* vol. 2012, 2012.

[11] F. F. Knapp and A. Dash, "Auger electron-Based Radionuclide Therapy " in *Radiopharmaceuticals for Therapy,* New Delhi: Springer, 2016, p. 58.

[12] B. Boudaïffa, P. Cloutier, D. Hunting, M. A. Huels, and L. Sanche, "Resonant formation of DNA strand breaks by low-energy (3 to 20 eV) electrons," *Science,* vol. 287, no. 5458, pp. 1658-1660, 2000.

[13] A. I. Kassis, "The amazing world of Auger electrons," *International Journal of Radiation Biology,* vol. 80, no. 11-12, pp. 789-803, 2004.

[14] F. Buchegger, F. Perillo-Adamer, Y. M. Dupertuis, and A. B. Delaloye, "Auger radiation targeted into DNA: a therapy perspective," *European Journal of Nuclear Medicine and Molecular Imaging,* vol. 33, no. 11, pp. 1352-1363, 2006.

[15] A. A. S. Tavares and J. M. R. Tavares, "^{99m}Tc Auger electrons for targeted tumour therapy: A review," *International Journal of Radiation Biology,* vol. 86, no. 4, pp. 261-270, 2010.

[16] C. Regaud and A. Lacassagne, "La radiosensibilite cellulaire envisage dans ses manifestations generalis," *Radiophysiologie et radiotherapie, Paris. Archieves de L'Institut du Radium de L'Universite de Paris and La Foundation Curie,* pp. 95-116, 1927.

[17] C. R. Arumainayagam, H.-L. Lee, R. B. Nelson, D. R. Haines, and R. P. Gunawardane, "Low-energy electron-induced reactions in condensed matter," *Surface Science Reports,* vol. 65, no. 1, pp. 1-44, 2010.

[18] E. Alizadeh, A. G. Sanz, G. García, and L. Sanche, "Radiation damage to DNA: The indirect effect of low-energy electrons," *The Journal of Physical Chemistry Letters,* vol. 4, no. 5, pp. 820-825, 2013.

[19] R. A. Laskey and A. D. Mills, "Enhanced autoradiographic detection of ^{32}P and ^{125}I using intensifying screens and hypersensitized film," *FEBS letters,* vol. 82, no. 2, pp. 314-316, 1977.

[20] A. Pronschinske, P. Pedevilla, B. Coughlin, C. J. Murphy, F. R. Lucci, M. A. Payne, A. J. Gellman, A. Michaelides, and E. C. H. Sykes, "Atomic-scale picture of the composition, decay, and oxidation of two-dimensional radioactive films," *ACS Nano,* vol. 10, no. 2, pp. 2152-2158, 2016.

[21] T. Fischer, K. Schomäcker, and H. Schicha, "Diethylstilbestrol (DES) labeled with Auger emitters: Potential radiopharmaceutical for therapy of estrogen receptor-positive tumors and their metastases?," *International Journal of Radiation Biology,* vol. 84, no. 12, pp. 1112-1122, 2008.

[22] C. Chan, Z. Cai, R. Su, and R. M. Reilly, "^{111} In-or ^{99m} Tc-labeled recombinant VEGF bioconjugates: in vitro evaluation of their cytotoxicity on porcine aortic endothelial

cells overexpressing Flt-1 receptors," *Nuclear Medicine and Biology,* vol. 37, no. 2, pp. 105-115, 2010.

[23] D. L. Costantini, K. McLarty, H. Lee, S. J. Done, K. A. Vallis, and R. M. Reilly, "Antitumor effects and normal-tissue toxicity of 111In-nuclear localization sequence-trastuzumab in athymic mice bearing HER-positive human breast cancer xenografts," *Journal of Nuclear Medicine,* vol. 51, no. 7, pp. 1084-1091, 2010.

[24] E. Koumarianou, T. A. Slastnikova, M. Pruszynski, A. A. Rosenkranz, G. Vaidyanathan, A. S. Sobolev, and M. R. Zalutsky, "Radiolabeling and in vitro evaluation of ^{67} Ga-NOTA-modular nanotransporter–A potential Auger electron emitting EGFR-targeted radiotherapeutic," *Nuclear Medicine and Biology,* vol. 41, no. 6, pp. 441-449, 2014.

[25] A. P. Kiess, I. Minn, Y. Chen, R. Hobbs, G. Sgouros, R. C. Mease, M. Pullambhatla, C. J. Shen, C. A. Foss, and M. G. Pomper, "Auger radiopharmaceutical therapy targeting prostate-specific membrane antigen," *Journal of Nuclear Medicine,* vol. 56, no. 9, pp. 1401-1407, 2015.

[26] Nuclear Physics for Medicine. (2014). *Nuclear Physics European Collaboration Committee*. Available: http://www.nupecc.org/pub/npmed2014.pdf

[27] S. Adelstein, "Merrill C. Sosman Lecture. The Auger process: a therapeutic promise?," *AJR. American Journal of Roentgenology,* vol. 160, no. 4, pp. 707-713, 1993.

[28] C. Hillyar, "Auger electron radionuclide therapy utilising F3 peptide to target the nucleolus," PhD thesis, University of Oxford, England, 2015.

[29] National Nanotechnology Initiative. (2000). *Size of the Nanoscale*. Available: https://www.nano.gov/nanotech-101/what/nano-size

[30] J.-P. Pouget, I. Navarro-Teulon, M. Bardiès, N. Chouin, G. Cartron, A. Pèlegrin, and D. Azria, "Clinical radioimmunotherapy—the role of radiobiology," *Nature Reviews Clinical Oncology,* vol. 8, no. 12, p. 720, 2011.

[31] A. I. Kassis, "Therapeutic radionuclides: biophysical and radiobiologic principles," in *Seminars in nuclear medicine*, 2008, vol. 38, no. 5, pp. 358-366: Elsevier.

[32] T. M. Behr, M. Béhé, M. Löhr, G. Sgouros, C. Angerstein, E. Wehrmann, K. Nebendahl, and W. Becker, "Therapeutic advantages of Auger electron- over β-emitting radiometals or radioiodine when conjugated to internalizing antibodies," *European Journal of Nuclear Medicine,* journal article vol. 27, no. 7, pp. 753-765, June 01 2000.

[33] A. Capello, E. P. Krenning, W. A. Breeman, B. F. Bernard, and M. de Jong, "Peptide receptor radionuclide therapy in vitro using [^{111}In-DTPA^{0}] octreotide," *Journal of Nuclear Medicine,* vol. 44, no. 1, pp. 98-104, 2003.

[34] E. T. Janson, J.-E. Westlin, U. Ohrvall, K. Oberg, and A. Lukinius, "Nuclear localization of ^{111} In after intravenous injection of [^{111} In-DTPA-D-Phe ^{1}]-octreotide in patients with neuroendocrine tumors," *The Journal of Nuclear Medicine,* vol. 41, no. 9, p. 1514, 2000.

[35] R. M. Reilly, R. Kiarash, R. G. Cameron, and N. Porlier, "^{111} In-labeled EGF is selectively radiotoxic to human breast cancer cells overexpressing EGFR," *The Journal of Nuclear Medicine,* vol. 41, no. 3, p. 429, 2000.

[36] R. W. Howell, "Auger processes in the 21st century," *International Journal of Radiation Biology,* vol. 84, no. 12, pp. 959-975, 2008.

[37] A. I. Kassis, "Cancer therapy with Auger electrons: are we almost there?," *Journal of Nuclear Medicine,* vol. 44, no. 9, pp. 1479-1481, 2003.

[38] P. Unak, "Targeted tumor radiotherapy," *Brazilian Archives of Biology and Technology,* vol. 45, no. SPE, pp. 97-110, 2002.

[39] C. T. R. Wilson, "On an expansion apparatus for making visible the tracks of ionising particles in gases and some results obtained by its use," *Proceedings of the Royal Society of London. Series A, Containing Papers of a Mathematical and Physical Character,* vol. 87, no. 595, pp. 277-292, 1912.

[40] P. Auger, "Sur les rayons β secondaires produits dans un gaz par des rayons X," *CR Acad. Sci.(F),* vol. 177, p. 169, 1923.

[41] D. Coster and R. d. L. Kronig, "New type of auger effect and its influence on the x-ray spectrum," *Physica,* vol. 2, no. 1-12, pp. 13-24, 1935.

[42] J. Lander, "Auger peaks in the energy spectra of secondary electrons from various materials," *Physical Review,* vol. 91, no. 6, p. 1382, 1953.

[43] G. Harrower, "Auger electron emission in the energy spectra of secondary electrons from Mo and W," *Physical Review,* vol. 102, no. 2, p. 340, 1956.

[44] L. Tharp and E. Scheibner, "Energy spectra of inelastically scattered electrons and LEED studies of tungsten," *Journal of Applied Physics,* vol. 38, no. 8, pp. 3320-3330, 1967.

[45] L. Harris, "Analysis of materials by electron-excited Auger electrons," *Journal of Applied Physics,* vol. 39, no. 3, pp. 1419-1427, 1968.

[46] P. Palmberg, G. Bohn, and J. C. Tracy, "High sensitivity Auger electron spectrometer," *Applied Physics Letters*, vol. 15, no. 8, pp. 254-255, 1969.

[47] N. MacDonald, "Auger electron spectroscopy in scanning electron microscopy: Potential measurements," *Applied Physics Letters*, vol. 16, no. 2, pp. 76-80, 1970.

[48] W. Casey and R. Albridge, "The L-and K-Auger spectra of tellurium," *Zeitschrift für Physik A Hadrons and Nuclei*, vol. 219, no. 3, pp. 216-226, 1969.

[49] C. Briançon, B. Legrand, R. Walen, T. Vylov, A. Minkova, and A. Inoyatov, "A new combined electrostatic electron spectrometer," *Nuclear Instruments and Methods in Physics Research*, vol. 221, no. 3, pp. 547-557, 1984.

[50] A. Kovalík, E. Yakushev, D. Filosofov, V. Gorozhankin, P. Petev, and M. Mahmoud, "Precise measurement of the KLL and KLX Auger spectra of cadmium from the EC-decay of ^{111}In," *Journal of Electron Spectroscopy and Related Phenomena*, vol. 105, no. 2, pp. 219-229, 1999.

[51] A. Kovalík, A. Lubashevsky, A. Inoyatov, D. Filosofov, N. Korolev, V. Gorozhankin, T. Vylov, and I. Štekl, "A detailed experimental investigation of the low energy electron spectrum generated in the EC-decay of $_{31}{}^{67}$Ge," *Journal of Electron Spectroscopy and Related Phenomena*, vol. 134, no. 1, pp. 67-79, 2004.

[52] A. K. Inoyatov, L. Perevoshchikov, A. Kovalík, D. Filosofov, Y. V. Yushkevich, M. Ryšavý, B. Lee, T. Kibédi, A. Stuchbery, and V. Zhdanov, "Search for environmental effects on the KLL Auger spectrum of rubidium generated in radioactive decay," *Physica Scripta*, vol. 90, no. 2, p. 025402, 2015.

[53] A. Pronschinske, P. Pedevilla, C. J. Murphy, E. A. Lewis, F. R. Lucci, G. Brown, G. Pappas, A. Michaelides, and E. C. H. Sykes, "Enhancement of low-energy electron emission in 2D radioactive films," *Nature Materials*, vol. 14, no. 9, pp. 904-907, 2015.

[54] D. Reger, S. Goode, and D.Ball, *Chemistry: Principles and Practice*. United States of America: Cengage Learning, 2010, pp. 264-265.

[55] A.Beiser, *Concepts of Modern Physics*. New York: McGraw-Hill, 2003, pp. 249-255.

[56] Andrea Hazard. (2016). *enhanced Bohr model with subshells*. Available: https://commons.wikimedia.org/wiki/File:52_tellurium_(Te)_enhanced_Bohr_model.png

[57] F. Larkins, "Semiempirical Auger-electron energies for elements $10 \leq Z \leq 100$," *Atomic Data and Nuclear Data Tables*, vol. 20, no. 4, pp. 311-387, 1977.

[58] J.R.Cooper, K.Randle, and R.S.Sokhi, *Radioactive Releases in the Environment: Impact and Assessment*. England: Wiley and Sons, 2003, pp. 33-34.

[59] D.K.Jha, *Radioactivity And Radioactive Decay*. New Delhi: Discovery Publishing House, 2004, pp. 2-3.

[60] J.S.Lilley, *Nuclear Physics: Principles and Applications*. England: Wiley and Sons, 2001, pp. 18-19.

[61] Radioactivity.eu.com. (2001). *Radioactive decay*. Available: http://www.radioactivity.eu.com/site/pages/Radioactive_Decay.htm

[62] J. Katakura, "Nuclear data sheets for A= 125," *Nuclear Data Sheets*, vol. 112, no. 3, pp. 495-705, 2011.

[63] M. F. L'Annunziata, *Handbook of Radioactivity Analysis*. Oxford UK: Elsevier Inc, 2012, pp. 57-70.

[64] M. Bé, V. Chisté, C. Dulieu, E. Browne, V. Chechev, N. Kuzmenko, R. Helmer, A. Nichols, E. Schönfeld, and R. Dersch, "Table of radionuclides (Vol. 1-A= 1 to 150)," *Bureau International des Poids et Mesures, France: Sèvres*, 2004.

[65] B. Q. Lee, "A Numerical Model of Atomic Relaxation and its Applications," PhD thesis, The Australian National University, Australia, 2017.

[66] M. Bé, V. Chisté, C. Dulieu, E. Browne, C. Baglin, V. Chechev, N. Kuzmenco, R. Helmer, F. Kondev, and D. MacMahon, "Table of Radionuclides (vol. 3–A= 3 to 244)," *Monographie BIPM*, vol. 5, 2006.

[67] K. S. Krane, *Introductory Nuclear Physics*. New York: Wiley and Sons, 1988, pp. 341- 348.

[68] T. Kibedi, T. W. Burrows, M. Trzhaskovskaya, and C. Nestor Jr, "A new tool to interpolate conversion coefficients and E0 electronic factors," in *AIP Conference Proceedings*, 2005, vol. 769, no. 1, pp. 268-271: AIP.

[69] T. Kibédi. (2011). *BrIcc - program to evaluate conversion coefficients User's manual for version 2.3.* . Available: http://bricc.anu.edu.au/BrIccV2.3Manual.pdf

[70] M. Rose, G. Goertzel, B. Spinrad, J. Harr, and P. Strong, "The Internal Conversion Coefficients. I: The K-Shell," *Physical Review*, vol. 83, no. 1, p. 79, 1951.

[71] T. Green and M. Rose, "Nuclear structure effects in internal conversion," *Physical Review*, vol. 110, no. 1, p. 105, 1958.

[72] H. C. Pauli and U. Raff, "A computer program for internal conversion coefficients and particle parameters," *Computer Physics Communications*, vol. 9, no. 6, pp. 392-407, 1975.

[73] R. B. Firestone, C. M. Baglin, and S. Y. F. Chu, *Table of Isotopes: 1999 Update* (no. v. 4). Wiley, 1999.

[74] R. S. Hager and E. C. Seltzer, "Internal conversion tables part I: K-, L-, M-shell conversion coefficients for Z= 30 to Z= 103," *Nuclear Data Sheets. Section A,* vol. 4, no. 1-2, pp. 1-11, 1968.

[75] J.W. Rohlf, *Modern Physics from a to Z0*. United States of America: Wiley, 1994, pp. 150 - 152.

[76] Python Software Foundation. (2010). *Python Language Reference, version 2.7.* Available: http://www.python.org

[77] K. S. Krane, *Introductory Nuclear Physics*. New York: Wiley and Sons, 1988, pp. 161-167.

[78] O. Šipr, J. Vackár, and J. Minár, "Finite lifetime broadening of calculated X-ray absorption spectra: possible artefacts close to the edge," *Journal of Synchrotron Radiation,* vol. 25, no. 2, pp. 523-528, 2018.

[79] N.Tsoulfanidis and S. Landsberger, *Measurement & Detection of Radiation* New York: CRC Press Taylor & Francis Group, 2015, pp. 33-39.

[80] F. R. Knapp and A. Dash, "Auger Electron-Based Radionuclide Therapy," in *Radiopharmaceuticals for Therapy*: Springer, 2016, pp. 57-67.

[81] D. P. Woodruff T.A. Delchar, *Modern Techniques of Surface Science*. Cambridge UK: Cambridge University Press, 1994, pp. 170-174.

[82] R. Jenkins, R. Manne, R. Robin, and C. Senemaud, "IUPAC—nomenclature system for X-ray spectroscopy," *X-Ray Spectrometry,* vol. 20, no. 3, pp. 149-155, 1991.

[83] R. W. Howell, "Radiation spectra for Auger-electron emitting radionuclides: Report No. 2 of AAPM Nuclear Medicine Task Group No. 6," *Medical Physics,* vol. 19, no. 6, pp. 1371-1383, 1992.

[84] M. Krause, "Rearrangement of inner shell ionized atoms," *Le Journal de Physique Colloques,* vol. 32, no. C4, pp. C4-67-C64-75, 1971.

[85] T. A. Carlson and M. O. Krause, "Electron Shake-Off Resulting from K-Shell Ionization in Neon Measured as a Function of Photoelectron Velocity," *Physical Review,* vol. 140, no. 4A, p. A1057, 1965.

[86] I. Manno, *Introduction to the Monte-Carlo method*. Akadémiai Kiadó, 1999.

[87] W. Bambynek, B. Crasemann, R. Fink, H.-U. Freund, H. Mark, C. Swift, R. Price, and P. V. Rao, "X-ray fluorescence yields, Auger, and Coster-Kronig transition probabilities," *Reviews of Modern Physics,* vol. 44, no. 4, p. 716, 1972.

[88] A. Kahoul, A. Abassi, B. Deghfel, and M. Nekkab, "K-shell fluorescence yields for elements with 6≤ Z≤ 99," *Radiation Physics and Chemistry,* vol. 80, no. 3, pp. 369-377, 2011.

[89] A. Némethy, L. Kövér, I. Cserny, D. Varga, and P. Barna, "The KLL and KLM Auger spectra of 3d transition metals, Z= 23–26," *Journal of Electron Spectroscopy and Related Phenomena,* vol. 82, no. 1-2, pp. 31-40, 1996.

[90] W. Mehlhorn and R. Albridge, "Diekll-Auger-Spektren von Eisen und Vanadium," *Zeitschrift für Physik,* vol. 175, no. 5, pp. 506-519, 1963.

[91] H.-H. Grotheer, J. W. Hammer, and K.-W. Hoffmann, "Experimentelle Untersuchungen am Elektroneneinfang des 85 Strontium und 88 Yttrium," *Zeitschrift für Physik A Hadrons and nuclei,* vol. 225, no. 4, pp. 293-302, 1969.

[92] T. A. Carlson and C. Nestor Jr, "Calculation of electron shake-off probabilities as the result of X-ray photoionization of the rare gases," *Physical Review A,* vol. 8, no. 6, p. 2887, 1973.

[93] T. A. Carlson, C. Nestor Jr, T. C. Tucker, and F. Malik, "Calculation of electron shake-off for elements from Z= 2 to 92 with the use of self-consistent-field wave functions," *Physical Review,* vol. 169, no. 1, p. 27, 1968.

[94] M. O. Krause and T. A. Carlson, "Vacancy cascade in the reorganization of Krypton ionized in an inner shell," *Physical Review,* vol. 158, no. 1, p. 18, 1967.

[95] T. A. Carlson, "Double electron ejection resulting from photo-ionization in the outermost shell of He, Ne, and Ar, and its relationship to electron correlation," *Physical Review,* vol. 156, no. 1, p. 142, 1967.

[96] A. Kochur, A. Dudenko, and D. Petrini, "Shake process probabilities for outer-shell electrons in atoms with Z⩽ 71," *Journal of Physics B: Atomic, Molecular and Optical Physics,* vol. 35, no. 2, p. 395, 2002.

[97] T. Mukoyama and K. Taniguchi, "Atomic excitation as the result of inner-shell vacancy production," *Physical Review A,* vol. 36, no. 2, p. 693, 1987.

[98] J. Lowe, C. Chantler, and I. Grant, "Ab initio determination of satellite intensities in transition-metal photoemission spectroscopy using a multiconfiguration framework," *Physical Review A,* vol. 83, no. 6, p. 060501, 2011.

[99] J. Lowe, C. Chantler, and I. Grant, "A new approach to relativistic multi-configuration quantum mechanics in titanium," *Physics Letters A,* vol. 374, no. 47, pp. 4756-4760, 2010.

[100] D. F. Anagnostopoulos, R. Sharon, D. Gotta, and M. Deutsch, "K α and K β x-ray emission spectra of metallic scandium," *Physical Review A,* vol. 60, no. 3, p. 2018, 1999.

[101] Y. Ito, T. Tochio, H. Oohashi, and A. Vlaicu, "Contribution of the [1s3d] shake process to $K\alpha_{1,2}$ spectra in 3d elements," *Radiation Physics and Chemistry,* vol. 75, no. 11, pp. 1534-1537, 2006.

[102] G. Hölzer, M. Fritsch, M. Deutsch, J. Härtwig, and E. Förster, "K $\alpha_{1,2}$ and K $\beta_{1,3}$ x-ray emission lines of the 3 d transition metals," *Physical Review A,* vol. 56, no. 6, p. 4554, 1997.

[103] T. A. Carlson, "The nature of secondary electrons created as the result of electron shake-off and vacancy cascades," *Radiation Research,* vol. 64, no. 1, pp. 53-69, 1975.

[104] V. Bulgakov, A. Kaznovetskij, V. Kirishchuk, S. Kovalenko, V. Kupryashkin, A. Lashko, N. Stril'chuk, A. Feoktistov, and I. Shapovalova, "Study on effect of Auger electrons energy dependence of Ir and Lu KLL-group on atom excitation method," *Izvestiya Akademii Nauk SSSR, Seriya Fizicheskaya,* vol. 55, no. 11, pp. 2147-2153, 1991.

[105] A. Kovalik, "Effects of level-crossing interaction and nuclear transformation processes on the L_3-*MM* Auger spectrum of $_{64}{}^{155}$Gd," *Journal of Electron Spectroscopy and Related Phenomena,* vol. 70, no. 1, pp. 51-60, 1994.

[106] M. H. Chen, B. Crasemann, and H. Mark, "Relativistic K− L L Auger spectra in the intermediate-coupling scheme with configuration interaction," *Physical Review A,* vol. 21, no. 2, p. 442, 1980.

[107] G. Howat, "The effects of orbital relaxation and interchannel interaction on magnesium K Auger transition rates," *Journal of Physics B: Atomic and Molecular Physics,* vol. 11, no. 9, p. 1589, 1978.

[108] T. Kibedi, T. Burrows, M. Trzhaskovskaya, P. M. Davidson, and C. Nestor Jr, "Evaluation of theoretical conversion coefficients using BrIcc," *Nuclear Instruments and Methods in Physics Research Section A: Accelerators, Spectrometers, Detectors and Associated Equipment,* vol. 589, no. 2, pp. 202-229, 2008.

[109] E. Schönfeld, "Calculation of fractional electron capture probabilities," *Applied Radiation and Isotopes,* vol. 49, no. 9, pp. 1353-1357, 1998.

[110] S. Perkins, D. Cullen, M. Chen, J. Rathkopf, J. Scofield, and J. Hubbell, "Tables and graphs of atomic subshell and relaxation data derived from the LLNL Evaluated

Atomic Data Library (EADL), Z= 1--100," Lawrence Livermore National Lab., CA (United States)1991.

[111] I. Band, M. Trzhaskovskaya, C. Nestor Jr, P. Tikkanen, and S. Raman, "Dirac–Fock internal conversion coefficients," *Atomic Data and Nuclear Data Tables*, vol. 81, no. 1-2, pp. 1-334, 2002.

[112] B. Q. Lee, H. Nikjoo, J. Ekman, P. Jönsson, A. E. Stuchbery, and T. Kibédi, "A stochastic cascade model for Auger-electron emitting radionuclides," *International Journal of Radiation Biology*, vol. 92, no. 11, pp. 641-653, 2016.

[113] N. Falzone, B. Q. Lee, J. M. Fernández-Varea, C. Kartsonaki, A. E. Stuchbery, T. Kibédi, and K. A. Vallis, "Absorbed dose evaluation of Auger electron-emitting radionuclides: impact of input decay spectra on dose point kernels and S-values," *Physics in Medicine & Biology*, vol. 62, no. 6, p. 2239, 2017.

[114] T. Kibedi, M. Trzhaskovskaya, M. Gupta, and A. Stuchbery, "Conversion coefficients for superheavy elements," *Atomic Data and Nuclear Data Tables*, vol. 98, no. 2, pp. 313-355, 2012.

[115] D. Zatsepin, I. Zhidkov, and A. Zatsepin, *Lecture: The Shapes of XPS Spectra – How to Process the Background Correctly?* 2014.

[116] V. Brabec, M. Ryšavý, O. Dragoun, M. Fišer, A. Kovalik, C. Ujhelyi, and D. Berényi, "Nuclear structure and chemical effects in internal conversion of the 35 keV M1+E2 transition in ^{125} Te," *Zeitschrift für Physik A Atoms and Nuclei*, vol. 306, no. 4, pp. 347-351, 1982.

[117] W. Bambynek, "Production of Inner-Shell Vacancies by Orbital Electron Capture of the Nucleus and by Internal Conversion of Gamma Rays," in *Low-Level Measurements of Man-Made Radionuclides in the Environment*: World Scientific, 1991, pp. 138-155.

[118] L. Huang, P. Zeppenfeld, S. Horch, and G. Comsa, "Determination of iodine adlayer structures on Au (111) by scanning tunneling microscopy," *The Journal of Chemical Physics*, vol. 107, no. 2, pp. 585-591, 1997.

[119] Staib instruments. (2004). *Super-CMA*. Available: http://www.staibinstruments.com/super-cma-highlights/

[120] G. Gergely, M. Menyhard, A. Sulyok, J. Toth, D. Varga, and K. Tokesi, "Determination of the transmission and correction of electron spectrometers, based on backscattering and elastic reflection of electrons," *Applied Surface Science*, vol. 144, pp. 101-105, 1999.

[121] SIMION. (2003). *The field and particle trajectory simulator, SIMION version 8.1*. Available: http://simion.com/info/simion80.html

[122] QUASES. (2016). *QUASES-IMFP-TPP2M Ver.3.0*. Available: http://www.quases.com/products/quases-imfp-tpp2m/

[123] A. Jablonski, F. Salvat, and C. Powell, "NIST electron elastic-scattering cross-section database," *NIST Standard Reference Database,* vol. 64, 2010.

[124] Origin. (2018). *Origin Pro 2018b*. Available: http://www.originlab.com

[125] Sjuts. (2002). *Introduction / Principles of Operation*. Available: http://www.sjuts.com/Introduction_Principles.html

[126] M. Went and M. Vos, "Electron-induced KLL Auger electron spectroscopy of Fe, Cu and Ge," *Journal of Electron Spectroscopy and Related Phenomena,* vol. 148, no. 2, pp. 107-114, 2005.

[127] M. Vos, G. Cornish, and E. Weigold, "High-energy (e, 2 e) spectrometer for the study of the spectral momentum density of materials," *Review of Scientific Instruments,* vol. 71, no. 10, pp. 3831-3840, 2000.

[128] M. Vos, M. Went, and E. Weigold, "Electron spectroscopy using two-dimensional electron detection and a camera in a single electron counting mode," *Review of Scientific Instruments,* vol. 80, no. 6, p. 063302, 2009.

[129] J. Campbell and T. Papp, "Widths of the atomic K–N7 levels," *Atomic Data and Nuclear Data Tables,* vol. 77, no. 1, pp. 1-56, 2001.

[130] C. Kunz, B. Cowie, W. Drube, T.-L. Lee, S. Thiess, C. Wild, and J. Zegenhagen, "Relative electron inelastic mean free paths for diamond and graphite at 8 keV and intrinsic contributions to the energy-loss," *Journal of Electron Spectroscopy and Related Phenomena,* vol. 173, no. 1, pp. 29-39, 2009.

[131] F. Yubero and S. Tougaard, "Quantification of plasmon excitations in core-level photoemission," *Physical Review B,* vol. 71, no. 4, p. 045414, 2005.

[132] Y. Chen, "Surface effects on angular distributions in X-ray-photoelectron spectroscopy," *Surface Science,* vol. 519, no. 1-2, pp. 115-124, 2002.

[133] M. O. Krause and J. Oliver, "Natural widths of atomic K and L levels, K α X-ray lines and several KLL Auger lines," *Journal of Physical and Chemical Reference Data,* vol. 8, no. 2, pp. 329-338, 1979.

[134] D. A. Shirley, "High-resolution X-ray photoemission spectrum of the valence bands of gold," *Physical Review B,* vol. 5, no. 12, p. 4709, 1972.

[135] T. Miura, Y. Hatsukawa, M. Yanaga, K. Endo, H. Nakahara, M. Fujioka, E. Tanaka, and A. Hashizume, "Relation of contact densities with Mössbauer isomer shifts for 35.46 keV M1 transition of ^{125} Te," *Hyperfine Interactions,* vol. 30, no. 4, pp. 371-386, 1986.

[136] F. James, "MINUIT function minimization and error analysis: reference manual version 94.1," 1994.

[137] M. Bé, B. Duchemin, K. Debertin, E. Schönfeld, F. Lagoutine, N. Coursol, and J. Legrand, "Table of Radionuclides–Introduction," *CEA/LNHB,* vol. 91191, 2011.

[138] A. Kovalík, V. Gorozhankin, A. Novgorodov, M. Mahmoud, N. Coursol, E. Yakushev, and V. Tsupko-Sitnikov, "The electron spectrum from the atomic deexcitation of $_{54}{}^{131}$Xe," *Journal of Electron Spectroscopy and Related Phenomena,* vol. 95, no. 2-3, pp. 231-254, 1998.

[139] J. Hubbell, P. Trehan, N. Singh, B. Chand, D. Mehta, M. Garg, R. Garg, S. Singh, and S. Puri, "A review, bibliography, and tabulation of K, L, and higher atomic shell X-Ray fluorescence yields," *Journal of Physical and Chemical Reference Data,* vol. 23, no. 2, pp. 339-364, 1994.

[140] M. O. Krause, "Atomic radiative and radiationless yields for K and L shells," *Journal of Physical and Chemical Reference Data,* vol. 8, no. 2, pp. 307-327, 1979.

[141] S. Singh, R. Rani, D. Mehta, N. Singh, P. Mangal, and P. Trehan, "K X-ray fluorescence cross-section measurements of some elements in the energy range 8–47 keV," *X-Ray Spectrometry,* vol. 19, no. 3, pp. 155-158, 1990.

[142] E. Karttunen, H. Freund, and R. Fink, "The K-fluorescence yield of Te and the total and K-shell conversion coefficients of the 35.48 keV transition in ^{125}I decay," *Nuclear Physics A,* vol. 131, no. 2, pp. 343-352, 1969.

[143] F. Tolea, K. Baker, W. Schmidt-Ott, and R. Fink, "The electron capture decay of ^{125} I and ^{145} Pm," *Zeitschrift für Physik,* vol. 268, no. 3, pp. 289-292, 1974.

[144] Y. Özdemir, R. Durak, and E. Öz, "K-shell X-ray production cross-sections and fluorescence yields in some medium-Z elements," *Radiation Physics and Chemistry,* vol. 65, no. 3, pp. 199-204, 2002.

[145] T. Yashoda, S. Krishnaveni, and R. Gowda, "Measurement of K-shell fluorescence yields for the elements in the range $22 \leqslant Z \leqslant 52$ excited by 14.4 and 122 keV photons," *Nuclear Instruments and Methods in Physics Research Section B: Beam Interactions with Materials and Atoms,* vol. 240, no. 3, pp. 607-611, 2005.

[146] M. Alotiby, I. Greguric, T. Kibedi, B. Tee, and M. Vos, "Quantitative electron spectroscopy of ^{125}I over an extended energy range," *Journal of Electron Spectroscopy and Related Phenomena,* vol. 232, pp. 73-82, 2019.

[147] F. Harris, P. Bassett, and M. Prutton, "Some properties of retarding-field spectrometers using postmonochromators," *Journal of Physics E: Scientific Instruments,* vol. 8, no. 1, p. 11, 1975.

[148] P. Staib and U. Dinklage, "Recent developments on an improved retarding-field analyser," *Journal of Physics E: Scientific Instruments,* vol. 10, no. 9, p. 914, 1977.

[149] J. Stepanek, "Methods to determine the fluorescence and Auger spectra due to decay of radionuclides or due to a single atomic-subshell ionization and comparisons with experiments," *Medical Physics,* vol. 27, no. 7, pp. 1544-1554, 2000.

[150] E. Pomplun, J. Booz, and D. Charlton, "A Monte Carlo simulation of Auger cascades," *Radiation Research,* vol. 111, no. 3, pp. 533-552, 1987.